Development of Novel Metal Oxide/Graphene Nanocomposites for Electrochemical- Energy Storage and Sensing Applications

A thesis submitted by

Hussen Maseed

(Reg. No. 12ENPT01)

in the partial fulfilment of the requirement for the award of the degree of

Doctor of Philosophy

in

Nano Science and Technology

Under the supervision of

Dr.-Ing. V. V. S. S. Srikanth



School of Engineering Sciences and Technology
University of Hyderabad
Central University (P.O.)
Hyderabad 500046
India

October 2019

Declaration

I, Hussen Maseed, declare that this thesis work entitled "Development of Novel Metal

Oxide/Graphene Nanocomposites for Electrochemical- Energy Storage and Sensing

Applications", submitted in partial fulfillment of the requirement for the award of Doctor of

Philosophy (in Nano Science and Technology) in the School of Engineering Sciences and

Technology, University of Hyderabad is completely my own work except for those referenced.

This work was done under the supervision of Dr.-Ing. V. V. S. S. Srikanth. This report is a

record of the bonafide research work carried out by me and the results incorporated in it have not

been reproduced/copied from any source. This work has not been submitted to any other

University or Institution for the award of any other degree or equivalent.

Hussen Maseed

Reg. No.: 12ENPT01

School of Engineering Sciences and Technology

University of Hyderabad



CERTIFICATE

This is to certify that the thesis entitled <u>Development of Novel Metal Oxide/Graphene Nanocomposites for Electrochemical- Energy Storage and Sensing Applications</u> Submitted by <u>Hussen Maseed</u> bearing registration number <u>12ENPT01 (Int. M.Tech./Ph.D. (Nano Science and Technology)</u> in partial fulfilment of the requirements for award of Doctor of Philosophy (Nano Science and Technology) in the <u>School of Engineering Sciences and Technology</u> is a bonafide work carried out by him under my supervision and guidance.

This thesis is free from plagiarism and has not been submitted previously in part or in full to this or any other University or Institution for award of any degree or diploma.

Parts of this thesis have been:

A. published in the following publications:

- 1. The Journal of Physical Chemistry C 121, 3778 (2017) (ISSN number: 1932-7455) Chapter 4
- 2. New Journal of Chemistry 42, 12817 (2018) (ISSN number: 1144-0546) Chapter 4

and

B. presented in the following conferences:

- 1. NANOS-2015 (International)
- 2. CEMAT-2016 (International)
- 3. IUMRS-ICYRAM-2016 (International)
- 4. ICONSEA-2018 (International)

Further, the student has passed the following courses towards fulfilment of coursework requirement for Ph.D.

Course Code	Name	Credits	Pass/Fail
AC801	Research Methodology	4	Pass

and was exempted from doing coursework (recommended by Doctoral Committee) on the basis of the following courses passed during her M.Tech. program (in Int. M.Tech./Ph.D. program) and the M.Tech. degree was awarded:

Course Code	Name	Credits	Pass/Fail
NT401	Thermodynamics and Phase Equilibria	4	Pass
NT402	Characterization of Materials	4	Pass
NT403	Advanced Engineering Mathematics	4	Pass
NT404	Seminar	2	Pass
NT405	Concepts of Nano Science and Technology	4	Pass
NT406	Synthesis and Application of Nanomaterials	4	Pass
NT407	Materials Processing and Characterization Laboratory	4	Pass
NT408	Polymer science and Technology	2	Pass
NT451	Nano Bio Technology	4	Pass
NT452	Mechanical Behaviour of Nanomaterials		Pass
NT453	Modeling and Simulation	4	Pass
NT454	MEMS and NEMS – Nanofabrication Technologies	4	Pass
NT455	Surface Engineering	4	Pass
NT456	Advanced characterization Techniques	2	Pass
NT457	Laboratory	4	Pass
NT458	Seminar	2	Pass
NT550	Dissertation	18	Pass

Supervisor Dean of School

Acknowledgements

I would like to express deep gratitude and sincere thanks to my research supervisor Dr.-Ing. V. V. S. S. Srikanth who provided me the opportunity to do Ph.D. under his supervision. I am very thankful to him for his invaluable guidance, encouragement, support and suggestions throughout my Ph.D. studies. I would like to thank my doctoral review committee members, Dr. Koteswararao V Rajulapati, School of Engineering Sciences and Technology (SEST), University of Hyderabad (UoH) and Dr. Rajanikanth, School of Physics (SOP), UoH for their valuable suggestions and comments which have helped in improving the quality of my thesis work. I am thankful to Prof. M. Ghanashyam Krishna, Dean and all faculty members of SEST for their support.

My special thanks to Dr. M. V. Reddy, National University of Singapore and Profs. B. V. R. Chowdary and Madhavi Srinivasn, Nanyang Technological University for providing battery testing facilities. I am grateful to my guru Prof. O. Md. Hussain, Sri Venkateswara University, Tirupati for providing electrochemical testing facility. Also, I thank my guru Mr. N. Venkateswara Rao (M.Sc. Mathematics), T.J.P.S. College, A.N.U, Guntur for his encouragement in my graduation that inspired me to pursue higher education.

I am very thankful to Drs. P. Shaikshavali and Naresh Kumar Rotte, for helping me at various stages of my Ph.D. work. I thank my lab mates Dr. K. V. Sreenivasulu, Mr. N. Charanadhar, Mrs. Regala Aneela, and Mrs. J. Sravani and research scholars Dr. Md. Quasim, Mr. Pagidi Srinivas, Mr. Pandu Sunil Kumar, Mr. S. Janaki Ram, Mr. Kolla Vijay Sekhar, Mrs. Debashrita Bharatiya, Ms. Khusnuma Asghar, Ms. Monica Pandey for their help, and constant encouragement. I am also thankful to the technical assistants Mr. K. Bala Kishan, Mr. G. Prasanth, Mr. S. Pankaj Kumar, and Ms. Ch. Sunitha for helping me with characterization techniques. I also thank the non-teaching staff of SEST for their help

I am grateful to university grant commission (UGC), India for providing financial support through Moulana Azad National Fellowship (MANF) scheme.

I am very thankful to my best friends Mr. Md. Dastagir Mirja (N.T.P.C.) and Mr. B. Srinath Guptha for their support. Finally, I am very thankful to my family members, father Sri. M. Meera Mohiddin, mother Smt. Mahabubi, Brothers Mr. M. Abdul Razaak and Mr. M. Jani Basha for their constant encouragement and who would always believe my abilities to be successful in academics and in career.

Hussen Maseed

This thesis is dedicated to

my beloved Family, Teachers and Friends

Table of Contents

Abstract	i
Chapter 1 Introduction	3
1.1 Energy Storage Systems	3
1.1.1 General Background	3
1.1.2 Li-ion Batteries	4
1.1.3 Supercapacitors	6
1.2 Electrochemical Bio-sensors	10
1.2.1 General Background	10
1.2.2 Requirements for Bio-sensing	11
1.2.3 Important Bio-molecules	11
1.3 Problem Definition and Objectives	13
1.4 Overview of the Thesis	14
References	14
Chapter 2 Literature Review	19
2.1 Metal Oxide-FLG Composites as Anodes in LIBs	19
2.2 Metal Oxide-FLG Composites as Electrodes in Supercapacitors	20
2.3 Metal Oxide-FLG Composites for Electrochemical Detection of Dop	oamine24
References	27
Chapter 3 Experimental Details	36
3.1 Synthesis of Materials	36
3.1.1 Graphene Oxide	36
3.1.2 Reduced Graphene Oxide	36
3.1.3 Fe ₃ O ₄ /FLG Composite	37
3.1.4 Fe ₂ Mo ₃ O ₈ /FLG Composite	37
3.1.5 MnO/FLG Composite	38
3.2 Materials Characterization	38
3.2.1 Electron Microscopy	38
3.2.2 X-ray Diffraction	38
3.2.3 Raman Scattering	39
3.2.4 X-ray Photoelectron Spectroscopy	39

3.2.5 Thermogravimetric Analysis	39
3.2.6 BET Surface Area Measurement	39
3.3 Li-ion Cell Testing	40
3.4 Supercapacitor Testing	40
3.5 Fe ₃ O ₄ /FLG-Glassy Carbon Electrode	41
Chapter 4 Results and Discussion	42
4.1 Anode Materials in Li Ion Batteries	42
4.1.1 Highly Crystalline Few Layered Graphene	42
4.1.2 Fe ₃ O ₄ /FLG Composite	52
4.1.3 Fe ₂ Mo ₃ O ₈ /FLG Composite	55
4.2 MnO/FLG Composite as Electrode Material in Supercapacitor	63
4.3 Fe ₃ O ₄ /FLG Composite for Electrochemical Detection of Dopamine	70
References	79
Chapter 5 Conclusions and Future Scope	84
5.1 Conclusions	84
5.2 Future Scope	86

Abstract

This thesis involves preparation and testing of various graphenaceous materials as anode materials in Li-ion batteries (LIBs), electrode material in supercapacitor and as electrochemical sensing material. In this context, of late, metal oxide (MO)-few layered graphene (FLG) composites have gained prominence mainly due to their ability to overcome the draw-backs of both metal oxides and FLG when used as the main materials in the above mentioned applications. The objectives of this thesis work are as follows (1) preparation of reduced graphene oxide (rGO) from GO by using microwave energy, (2) preparation and characterization of Fe₃O₄-FLG, Fe₂MO₃O₈-FLG, and MnO-FLG composites by using graphenothermal reduction (GTR) method, (3) to test microwave reduced GO, Fe₃O₄-FLG, and Fe₂MO₃O₈-FLG as anode materials in LIBs, (4) to test MnO-FLG composite as electrode material in aqueous supercapacitora and (5) to test Fe₃O₄-FLG composite as an electrochemical sensing material for the detection of dopamine (DA) in the presence of uric acid (UA) and ascorbic acid (AA). Even though there are several methods to prepare MO-FLG composites, graphenothermal reduction (GTR) has become the most popular method. In this work to prepare various MO-FLG composites, GTR method (which involves the use of dry powder mixture of graphene oxide (GO) and metal precursors in appropriate proportions as the starting materials) is used. GO is expected to exfoliate to FLG while MO forms simultaneously due to the reducing nature of carbons in GO. The main advantage of GTR approach is that the GO in the reaction mixture acts as a reducing agent as well as the source of FLG. Since the method is a solid state method, it facilitates easy synthesis of bulk amounts of MO_x-FLG. GTR method does not involve the use of any harmful or toxic chemicals. In this work rGO (named as highly crystalline few layered graphene (hcFLG)) was prepared by reducing GO in a household microwave oven. hcFLG when tested as an anode material in LIB delivered reversible capacities as high as 400 and 330 mAh g⁻¹ at 0.1 and 1.0 C current rates, respectively. hcFLG exhibited excellent rate capability by showing reversible capacity of 215 mAh g⁻¹ even at very high current rate of 10.0 C. Long-term cycling of hcFLG showed a great increase in reversibly capacity from 330 to 555 mAh g⁻¹ at 1175th cycle of 1.0 C rate and from 200 to 365 mAh g⁻¹ at 1160th cycle of 2.0 C rate. Fe₃O₄-FLG composite exhibited a reversible capacity of 860 mAh/g owing to good contacts between FLG and Fe₃O₄ phases. As-prepared Fe₂Mo₃O₈-FLG composite had hexagonal platelets of Fe₂Mo₃O₈ and sheet-like FLG. Diffraction analysis showed that Fe₂Mo₃O₈ phase is well crystallized into the hcp system. As-synthesized Fe₂Mo₃O₈-FLG showed a reversible capacity as high as 945 mAh g⁻¹ at 50 mA g⁻¹ current rate.

MnO-FLG composite was constituted by both micro and nano sized MnO particle networks that are uniformly anchored on FLG sheets which facilitate easy and efficient transfer of electrons and ions in the fabricated supercapacitor electrode in the presence of 1M LiSO₄. Due to the synergic effect between the FLG sheets and MnO, the composite electrode exhibited high specific capacitance of 778.5 F g⁻¹ at a current density of 0.5 mA g⁻¹ and good long term cycling stability. Binder-free Fe₃O₄-FLG/glassy carbon electrode showed excellent electrocatalytic action and excellent selectivity towards DA detection in the presence of UA and AA. The Fe₃O₄-FLG/glassy carbon electrode detected DA with a low limit of detection (LOD) of 3.429 nM and Limit of Quantification (LOQ) of 11.43 nM.

Chapter 1 Introduction

1.1 Energy Storage Systems

1.1.1 General Background

In our day-to-day life the consumption of non-renewable fossil fuels is increasing much faster than expected and as a consequence the associated environmental pollution is also growing at a faster rate [1-3]. Hence it is essential to balance the renewable and non-renewable energy resources such that future has sustainable energy sources [4-6]. To resolve the serious crisis of fossil fuels' depletion and associated environmental illnesses, advancement of energy storage and conversion devices with low carbon foot-print is urgently needed. Among the various energy storage devices, electrochemical storage devices are popular mainly owing to their efficiency and ease in fabrication. Ragone plot depicting power- and energy- densities of electrochemical energy storage devices is shown in Fig. 1.1. The energy density is the energy that can be stored in a system and power density represents how fast the stored energy could be converted to electricity [7,8]. From Fig. 1.1 it can be clearly observed that the energy density is usually low when power density is high. The electrochemical storage devices store the energy through different mechanisms and therefore they cannot charge/discharge quickly without overheating and possibly being damaged [9].

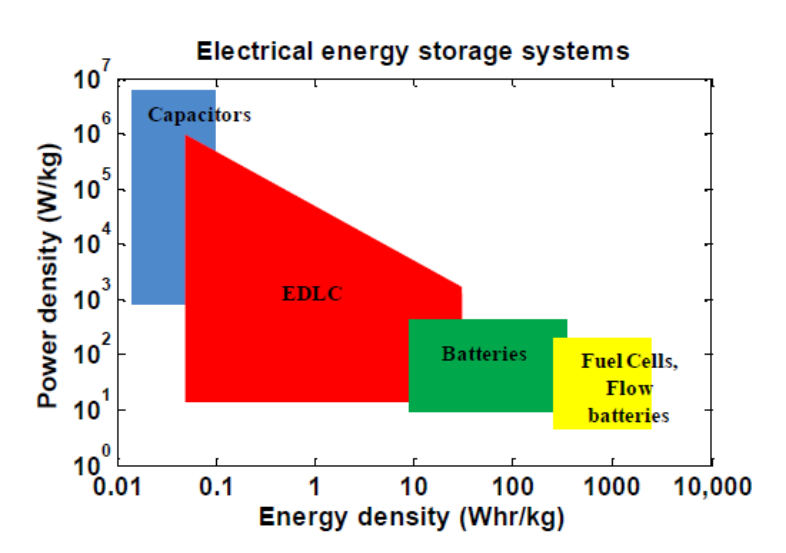


Figure 1.1. Ragone plot for electrochemical energy storage systems. EDLC is electric double layer capacitance.

Supercapacitors work lies between traditional capacitors and batteries. However, the capabilities of conventional capacitors and supercapacitors do not match the energy densities of batteries and fuel cells. Supercapacitor are gaining much attention from researchers as they

Introduction

provide high energy and power densities by order of magnitudes than the dielectric capacitors and long cycling stability as compared with batteries. Also, supercapacitors have the ability to store more electrical energy as compared to conventional capacitors and to deliver much faster in comparison with batteries because of the high specific surface area of the electrode materials [10]. Commercial supercapacitors can deliver energy densities as high as ~5 Whkg⁻¹, which is higher than those delivered by conventional solid-state electrolytic capacitors but far lower than those delivered by batteries and fuel cells, which can deliver as high as ~200 and ~350 Wh kg⁻¹, respectively [11]. An electrolytic capacitor stores energy by forming electric double layer between its electrodes and electrolyte [12]. In general, batteries and fuel cells have the ability to store more energy while supercapacitors have the ability to charge and discharge faster.

1.1.2 Li-ion Batteries

Li-ion batteries (LIBs) are the most promising rechargeable batteries which are used in a variety of applications. Li-type batteries were introduced in the early 1960s and with time these batteries have undergone several transformations. In the beginning, Li was used as the anode material, but it had safety issues due to growth of Li dendrites towards the cathode. With cycling these dendrites used to grow in size towards the cathode and at some point of time in operation they used to pierce the separator membrane and come in contact with the cathode triggering short circuit [13]. Currently, Li batteries are the dominant energy storage sources in laptops, mobile phones, computers, etc. [14]. However, the availability of Li sources in nature is a major drawback to meet the ever increasing demand for portable to transportation technology [15]. Even then, LIBs are in great demand to power electric vehicles [16,17]. The comparison among commercial rechargeable batteries (Pb-acid, Ni-Cd, Ni-metal hydride (Ni-MeH) battery, Li-ion and Li-ion-polymer, etc., batteries) in terms of the gravimetric and volumetric densities are shown in Fig. 1.2 [18]. It should be noted that among the different existing battery technologies, Li-ion rechargeable batteries have superior energy density and design flexibility. Other battery technologies such as Pb-acid and Ni-Cd batteries are toxic in nature owing to the presence of Pb and Cd in them. Li-ion batteries have become the most promising technologically due to their high- power, capacity, and charging rate, longer life span, safer operation, and lesser cost [19] and have become an integral part of everyone's dayto-day life through their presence in various portable devices and gadgets [20].

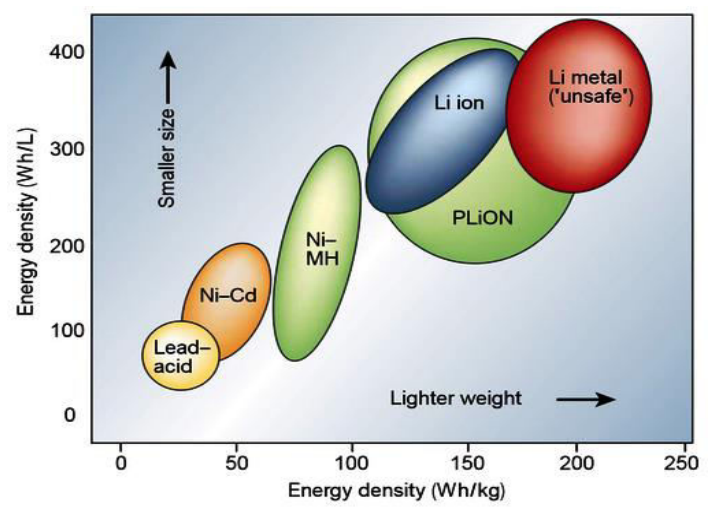


Figure 1.2. Comparison of different batteries as a function of volumetric and specific energy densities [18].

A battery is constituted by a number of electrochemical cells connected in a series (to increase voltage) or parallel (to increase current) or combined configurations to get required voltage and capacity. In batteries chemical form of energy is converted into electric power. Each battery unit primarily consists of anode and cathode in an electrolyte solution containing disassociated salts. The anode is indicated as negative lithiated carbon and cathode which contain Li-metal oxide as a positive electrode. The electrodes are separated by separator from each other, generally a micro porous membrane of polymer used which allows the Li ions exchange between the two electrodes but not the electrons. The electrolyte is a liquid solution which can act as a conducting medium and plays a key role in transporting ions from one electrode to another electrode. High purity lithium (Li) type organic solvent (LiPF₆ or LiBF₄ in mixed organic solvents of ethylene carbonate (EC), dimethyl carbonate (DMC) and diethyl carbonate (DEC) are used as electrolytes. The charge/discharge process when a Li-ion battery is connected to an external circuit is schematically represented in the Fig. 1.3. When it is charging the anode is oxidized and the cathode is reduced. During charging, the Li⁺ ions move from negative side to positive side (also known as an insertion) to build up charge while it is discharging, Li+ ions return to the cathode (exertion). This process is called as the Li intercalation process or "shuttle chair" mechanism [21,22]. The present day basic Li-ion battery designs are the still same as those which were introduced commercially two decades ago by Sony. However, various types of anode and cathode materials, electrolytes and separators are developed and tested. Nonetheless, LiCoO2 as cathode and graphite as anode are popular because they have great stability in atmosphere, their handling is simple and they have no difficulties at industrially scale [18].

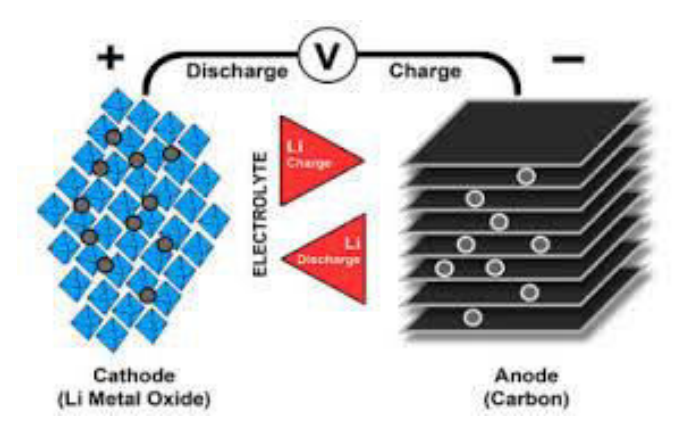


Figure 1.3. Schematic of Li-ion battery mechanism.

1.1.3 Supercapacitors

Supercapacitors or ultra-capacitors are basically energy storage devices that charge and discharge energy due to charge separation at electrode/electrolyte interface. The electrolyte can be aqueous as well as organic. The supercapacitors consist of two electrodes separated by the porous film called a separator and permeated by an electrolyte. The electrolytes have a huge amount of ions based on the type of solvents such as aqueous or organic electrolytes. The performance rate of a supercapacitor is essentially determined by its active electrode material [23]. Supercapacitors can provide a huge amount of energy in a very short span of time for the production of centralized power delivery systems. They have outstanding cyclic stability and ultra-high power density performance when compared to conventional batteries. Therefore supercapacitors are very crucial to meet future energy storage requirements [24]. However, supercapacitors exhibit a low energy density which has been the bottle neck in expanding their use in various applications. Of late, many new nanostructured materials (for energy storage and conversion) that can deliver high energy and power densities, in order to solve the serious problems of fossil fuel depletion and environmental pollution [25] are being developed. In recent times, in the field of electrochemical capacitors, new energy storing and converting nanostructured materials are being developed. Supercapacitors bridge the energy/power performance gap between the traditional capacitors (with high power densities) and rechargeable batteries (with high energy densities) [26]. Supercapacitor are primarily divided (Fig. 1.4) into electric double layer capacitors (EDLC), two, pseudo-capacitance capacitors and three, asymmetric or hybrid capacitors based on the respective underlying charge storage mechanism such as distributions of ions coming from the electrolyte to the electrode surface. They can be classified based on the active materials. One is these capacitors is briefly discussed in the following paragraphs.

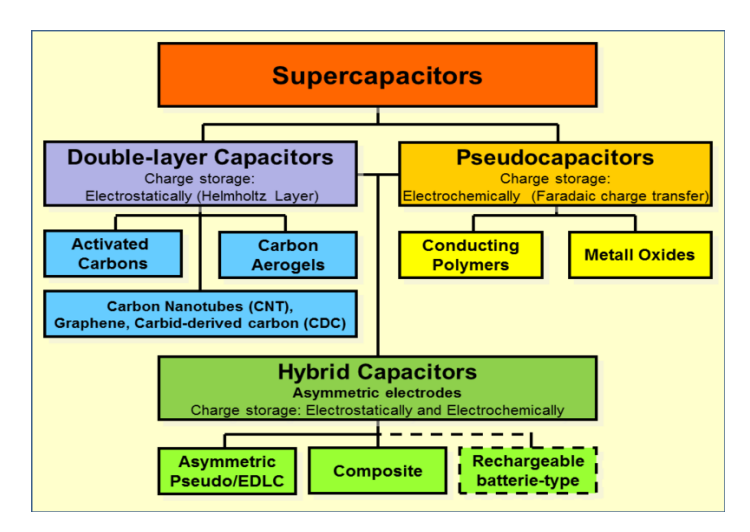


Figure 1.4. Taxonomy of supercapacitors.

Electrostatic capacitors are composed of using two parallel plates separated by a dielectric medium as shown in Fig. 1.5. Here A is the area of each plate, d is the distance of separation between the plates, E is the electric field across the plates and Q is the charge on each plate. The dielectric medium can be air, mica, and ceramic. The energy density E (i.e., energy stored per unit volume) of the capacitor is given by $E = (1/2) \text{ CV}^2$, where C and V are capacitance and potential, respectively.

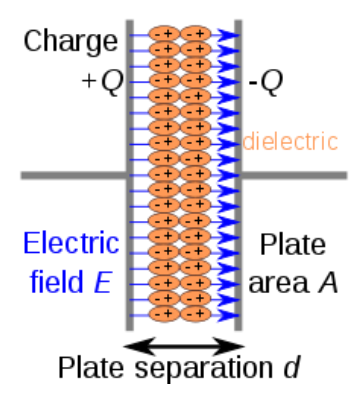


Figure 1.5. Schematic illustration of a charged electrostatic capacitor.

In the case of EDLC type capacitors, the stored electrical energy is nothing but the accumulation of charges by forming the two charged layers (double layers) [27]. EDLC mechanism (Fig. 1.6) was firstly demonstrated by Von Helmholtz, while he examined the opposite charges distribution at the electrode/electrolyte interface of a colloidal suspension of particles with separation of an atomic distance. This Helmholtz model is similar to conventional capacitors [28]. EDLC is capable of delivering very high power and long cycle life due to the fast and long-lasting activities between the active electrode and the electrolyte. EDLC's performance can be altered by changing the type of electrolyte used.

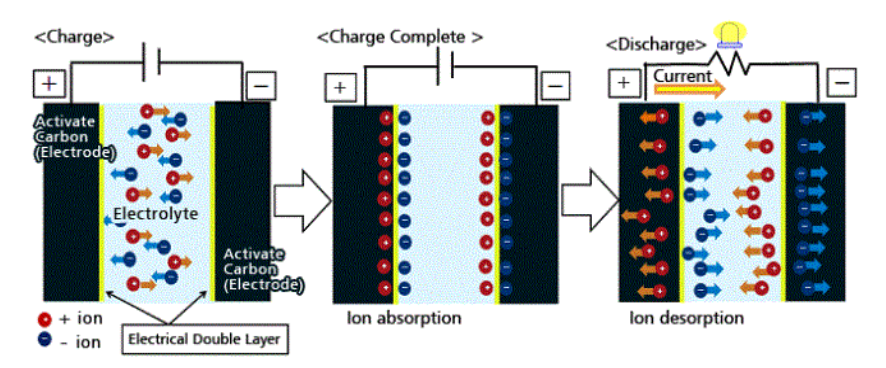


Figure 1.6. Mechanism of EDLC recharge/discharge process (www.murata.com).

The EDLC capacitor constitute 2 electrodes with an ion permeable separator in electrolyte solution. The separator helps to transport the ions. In such type of devices each electrode/electrolyte can be considered a capacitor and if two capacitors are arranged in series can be considered as a complete cell. For symmetrical capacitors with similar electrodes, the cell capacitance is measured by using the formula $1/C_{Cell} = 1/C_1 + 1/C_2$ where C_1 and C_2 are the capacitances of the first and second electrode, respectively. Carbon based materials and carbon allotropes such as activated carbon graphene etc., are common EDLC electrode materials owing to their easy processability, non-toxic nature, large specific surface area, appropriate electrical conductivity, controllable pore size of below 1 nm, suitability with different electrolytes etc. giving possibility of securing high energy and power densities [27,29,30]. However, the major drawback of these carbon-based materials is their low specific capacitance and power density and as a consequence they cannot be considered directly in real time applications.

Pseudo-capacitors work on the reversible oxidation and reduction (Faradic) reactions (which occur in the electrolyte and electroactive species on the electrode surface). In general, the Faradic reactions achieve higher specific capacitance of pseudocapacitors and energy densities when its compared with EDLC capacitors owing to excess charges moved additionally within definite window potential. Low power density and their cycling lifetimes are not as better as compared with EDLC because of active electrode material's degradation with the involvement of Faradic reaction process and also because of low electronic conductivity. However, metal oxides and conducting polymers meet all the requirements to be electrode materials in pseudocapacitors [31]. Transition metal oxides normally have high specific capacitance and high energy densities. Metal oxides (Co₃O₄, Fe₂O₃, Fe₃O₄, MnO, MnO₂, MoO₃, NiO, RuO₂, TiO₂, V₂O₅ etc.,) in combination with conduction polymers (such as polyaniline), graphene, CNT etc., has improved the performance [32].

In asymmetric or hybrid type capacitors the physical dimensions of the two electrodes are not

the same; one electrode is larger than the other resulting in higher cell voltage and energy density. In these capacitors, a capacitor type electrode is used as an anode for providing high power while a battery type electrode is used as a cathode (Faradic) as an energy source [33,34]. In other words, the asymmetric concept uses two different electrochemical charge storage mechanisms which proceed on different electrodes of a cell such as the positive type of electrode uses the mechanism of the faradic process and negative type of electrode uses electric double layer phenomenon (non-faradic). Asymmetric type supercaps are mainly used to increase the range of operating voltage (and thus its energy density and power density) and to combine the different natures of two different electrodes in order to enhance its overall performance [35]. EDLCs offer excellent cyclic stability and superior power performance while pseudocapacitors offer huge specific capacitance. The most important approach in these type of supercaps is to develop novel hybrid systems wherein both battery and supercapacitor are together performing. To secure higher specific capacitance values, a combination of pseudo capacitive nature metal oxide composites and conducting polymers can be used as cathode and carbon materials such as activated carbon or graphene (high stability material), carbon aerogels, multiwalled carbon nanotubes (MWCNTs) can be used as anode [36] (Fig. 1.7). The synergic effect between the structural and different morphological properties of metal oxide combined with conductive graphene (for example AC//CNT-V₂O₅, AC//NiTe, AC//RuO₂, AC//Co₃O₄, AC//Fe₃O₄, AC//MoO₃, AC//LiMn₂O₄, AC//PEDOT, CNT//MnO₂, rGO//Ni (OH)₂, rGO//TiO₂) will play an important role [37-41].

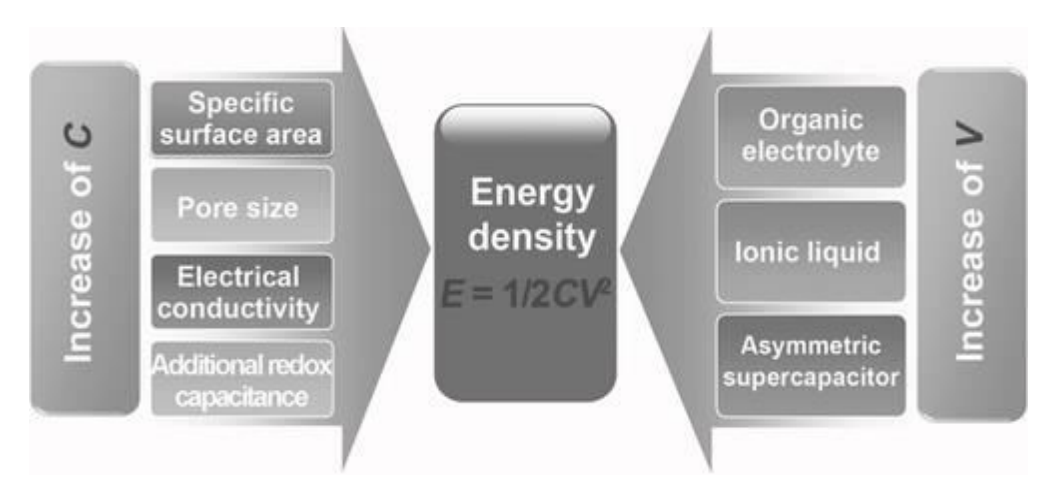


Figure 1.7. Schematic representation of different ways of improving a supercapacitor's performance [42].

A supercapacitor's specific capacitance and energy and power densities mainly depend upon the mass amount of material loading on the electrode surface. Besides, the type of substrates

Introduction

used in fabrication has a great influence on the supercapacitor's performance. To achieve better/higher specific capacitance, a less amount of quantity loading on the substrate will show a pathway of better transport for the diffusion of ions into electrode systems. On the other hand, loading of the higher mass quantity on the substrate can result in high series resistance and poor electrical conductivity which clearly indicates that only a partial amount of active material gets involved in oxidation-reduction (redox) reactions. It is one of the disadvantages of the metal oxide/hydroxide to obtain excellent specific capacitance and a high mass loading. The major drawback of these supercapacitors is its lower energy density. Even though the specific capacitance of transition metal oxides is high, because of their poor electrical conductivity there were was not commercialized. To resolve this problem, carbon allotropes namely graphene, carbon nanotubes etc., and conducting polymers were combined to make new composites. The supercapacitor bridges the gap between conventional supercapacitors and batteries because of their advantage of safe operation, low maintenance, long shelf life, high power density, faster dynamic discharge/charge or high rate capability. These can be used in many applications such as [43,44] hybrid electric vehicles (HEVs), portable electronics devices (PECS), power banks, rolled-up display devices, memory backup systems, large industrial equipment, renewable energy power plant etc.

1.2 Electrochemical Bio-sensors

1.2.1 General Background

An electrochemical biosensor is a type of device capable of detecting different types of biological analytes when its electrode has a physical contact with the analyte. The sensor transforms any sensitive biochemical information into a useful analytical signal either in current or potential form. During oxidation, electrons are transferred from the analyte while they leave the electrode during the reduction. Physical contact between the electrode and analyte is mandatory for the reactions to occur. The electrode output (in current or voltage form) is directly proportional to electrode material or compound concentration and also diffusion rate of compound concentration at the solution/electrode interface. Each and every material has its own fixed potential window for oxidation and reduction mechanism, which also depends on the material type of the electrode. The electrochemical sensors usually contain three electrodes and of course they can also work with two electrodes. The three electrodes are the working, reference and counter electrodes.

1.2.2 Requirements for Bio-sensing

The most important characteristics required for bio-sensing are selectivity and sensitivity of the electrochemical sensor for the detection of different analytes. Selectivity and sensitivity can be improved by using different surface modifications. The successful detection of analytes or target molecules can be measured using modified electrodes with fast response time or fast electron response time through different analytical techniques. Attributes such as economical usability, quick response, portable in nautre and simple to fabricate make the sensor outstanding. Recently, significant attention has been paid for the integration of recognition elements into electronic elements to develop novel electrochemical bio-sensors. With the use of functional nanomaterials (with large specific surface area) as electrode materials it is not only possible of generating a synergic effect but also produce catalytic effects, and improve conductivity and biocompatibility to speed up the signal transduction, but also increase biorecognition events with purposely designed signal tags rendering the sensors to be highly sensitive. It is well known that the material of the electrode mainly used in electrochemical detection must be conductive and stable. Examples of electrodes commonly used in commercial products are platinum, gold, carbon, and silicon. Materials with a large potential window can be used to detect selectively and simultaneously determine several types of analytes. Electrochemical bio-sensors mainly find their use in applications such as dopamine sensing and glucose monitoring.

1.2.3 Important Bio-molecules

Ascorbic acid (AA), dopamine (DA) and uric acid (UA) are crucial for human body's physiological function [45]. Insufficient or maladjustment levels of these can lead to many diseases [46,47]. The determination of AA, DA, and UA levels is therefore of great importance for the nerve physiology, to make a diagnosis and to control drugs. AA, DA, and UA co-exist in the central nervous system's fluidic content and it is difficult to simultaneously detect them owing to their interfering nature (due to similar oxidation potentials [48). Also, their individual or simultaneous electrochemical determination using traditional electrodes is complicated because they generally foul the electrodes. Different mechanisms have been proposed for the detection of biomolecules individually or simultaneously and to solve electrode-related issues [49]. In the fabrication of chemically modified electrochemical sensors for the detection DA, two essential factors should be taken into account: the first one is to boost the electrochemical activity and the second one is the selectivity of DA with different potentially interfering species such as AA, and UA. On the other hand, there are very popular analytical methods which are

currently in use for the detection of DA traces such as fluorescence, high-performance liquid chromatography (HPLC), chemiluminescence, and capillary electrophoresis [50-53]. Electrochemical techniques have stimulated huge interest among researchers because of their elevated selectivity, sensitivity, reproducibility, easy operation, high accuracy, real-time detection and low-cost expenditure fabrication of various advanced electrode materials to improve electrochemical sensing performance in detection of DA [54,55]. Dopamine (DA, 3, 4-dihydroxyphenethylamine) is a chemical compound of catecholamine in the central mammalian nervous system. DA has phenethylamine structure, which plays a neurotransmitter role in the brain and body functioning. It consists of a benzene ring having two hydroxyl groups (catechol) with a monoamine group attached. It operates as a chemical messenger to send the signal to other neurons to corroborate smooth muscle movement in the human body. Like other neurotransmitters, it cannot cross the blood-brain barrier. The use of prohibited drugs or substances such as cocaine, heroin, nicotine, and alcohol blocks the transport of DA which inhibits reabsorption of DA and increases the risk of depression and addiction of drugs [56,57]. Low-level concentration (0.01-1 µM) of DA in brain tissue was coupled with a variety of disease such as Alzheimer's disease (AD) [58], schizophrenia [59], epilepsy, attention deficit hyperactivity disorder (ADHD) [60] Huntington's syndrome. UA, which is a primary nitrogen heterocyclic compound in urine is a metabolic breakdown product of purine metabolism in the mammalian species. UA exists in blood and urine. Its abnormal concentration levels may result in several clinical disorders such as pneumonia, hyperuricemia, Lesch-Nyhan syndrome, gout, obesity, diabetes, hypertension, kidneys, and heart disease problems [61,62]. Numerous epidemiological studies on the elevation of serum in UA indicated a risk factor for cardiovascular disease. Therefore, to explore a simple, accurate and reliable method for the determination of UA has become a vital requirement. AA is a very common antioxidant, and dietary supplement found in the biological systems. It is also known as L-ascorbic acid or vitamin-C. AA is readily soluble in water. In human body metabolic process, it acts as an antioxidant (reducing agent) and plays an essential role in protecting biological development for example cell division, gene expressions, activation of natural defense mechanism from radical induced diseases [63,64]. The health benefits of AA are universally recognized. A rich amount of AA is found in animals, fruits and vegetables, which is well known that very well for health and on the other side Vitamin C based commercial products are also available in the market from the pharmaceutical industry. For the biological and agri-industries finding the concentration levels of AA in several natural products (vegetables, and fruits), prepared foods, drugs, pharmaceutical, and soft drinks is crucial. AA being an antioxidant, it effectively

removes radicals and reactive oxygen species (ROS), which are allied with tissue lesions and diseases, and aging course [65]. The excess concentration of AA in the blood can be excreted through urine even though it has low acute toxicity. A lower level of AA may cause scurvy disease (a syndrome occurring whose diet is quite a low intake of fresh fruits and vegetable). A higher level of AA dose may cause many problems like discomfort, nausea, headache, sleeping, gastrointestinal disturbance [66]. AA is helpful in treatment of Alzheimer's disease, cancer, atherosclerosis, and some infections related to HIV. AA is used to treat common cold, infertility, and mental illness, and AA can also act as anticancer agent [67].

1.3 Problem Definition and Objectives

LIBs and supercapacitors are the most promising energy storage devices. Their success depends mainly on the active electrode materials in them. In the case of LIBs, there is an attempt for quite some time to replace graphite with more efficient anode material. In this context, graphene-metal oxide composites have shown a great promise. However, these could not be commercialized yet due to the non-availability of synthesis methods that can be upscaled, high costs, time-consuming preparation methods and toxicity problems due synthesis. Therefore there is a great need to develop a suitable method to prepare efficient graphene-metal oxide composites that can be directly used as anode materials in LIBs. Some of these materials can also be suitable to be electrode materials in supercapacitors. This aspect has to be explored too. As discussed in the previous section, it is difficult to detect DA while AA and UA are interfering with DA's detection. Graphene-metal oxide composites can be suitable candidates as electrochemical sensor materials because they have suitable electrochemical behavior for such detection. However the use of such composites for electrochemical detection of DA was not explored when this thesis work was being planned.

In view of the above mentioned problem definition, the objectives of this thesis work are set as follows: (1) preparation of reduced graphene oxide (rGO) from GO by using microwave energy, (2) preparation and characterization of Fe₃O₄-FLG, Fe₂Mo₃O₈-FLG, and MnO-FLG composites by using graphenothermal reduction (GTR) method, (3) to test microwave reduced GO, Fe₃O₄-FLG, and Fe₂Mo₃O₈-FLG as anode materials in LIBs, (4) to test MnO-FLG composite as electrode material in aqueous supercapacitora and (5) to test Fe₃O₄-FLG composite as an electrochemical sensing material for the detection of DA while UA and AA are interfering with the detection of DA.

1.4 Overview of the Thesis

In Chapter 1, introduction to energy storage systems namely LIBs and supercapacitors and electrochemical bio-sensors is given. In this chapter, the motivation and main objectives of this thesis work and its outline are also explained. In Chapter 2, comprehensive literature review of relevant materials and devices to this thesis are presented. In Chapter 3, detailed experimental procedures involved in synthesis and characterization of materials and testing of devices are given. In Chapter 4, results and discussion of this thesis work are presented. This chapter is dived in three sections covering the results and discussion pertaining to LIBs, supercapacitor and bio-sensing. In Chapter 5, conclusions of this work and immediate future scope of research. Each chapter at its end has the sub-heading 'References' under which the references that are cited while presenting the discussion are listed.

References

- [1] Owusu PA, Asumadu-Sarkodie S. A review of renewable energy sources, sustainability issues and climate change mitigation. Cogent Engineering. 2016;3:1167990.
- [2] Reddy MV, Subba Rao GV, Chowdari BVR. Metal Oxides and Oxysalts as Anode Materials for Li Ion Batteries. Chemical Reviews. 2013;113:5364-457.
- [3] Lashof DA, Ahuja DR. Relative contributions of greenhouse gas emissions to global warming. Nature. 1990;344:529-31.
- [4] Chu S, Majumdar A. Opportunities and challenges for a sustainable energy future. Nature. 2012;488:294.
- [5] Nocera DG. Living healthy on a dying planet. Chemical Society Reviews. 2009;38:13-5.
- [6] Nadimi R, Tokimatsu K. Analyzing of Renewable and Non-Renewable Energy consumption via Bayesian Inference. Energy Procedia. 2017;142:2773-8.
- [7] Conway BE. Energy Density and Power Density of Electrical Energy Storage Devices. Electrochemical Supercapacitors: Scientific Fundamentals and Technological Applications. Boston, MA: Springer US; 1999. p. 417-77.
- [8] Winter M, Brodd RJ. What Are Batteries, Fuel Cells, and Supercapacitors? (Chem. Rev. 2003, 104, 4245–4269. Published on the Web 09/28/2004.). Chemical Reviews. 2005;105:1021-.
- [9] Tarascon JM, Armand M. Issues and challenges facing rechargeable lithium batteries. Nature. 2001;414:359.
- [10] Arbizzani C, Mastragostino M, Soavi F. New trends in electrochemical supercapacitors. Journal of Power Sources. 2001;100:164-70.
- [11] Shao Y, El-Kady MF, Sun J, Li Y, Zhang Q, Zhu M, et al. Design and Mechanisms of Asymmetric Supercapacitors. Chemical Reviews. 2018;118:9233-80.
- [12] Miller JR, Simon P. Electrochemical Capacitors for Energy Management. Science. 2008;321:651-2.
- [13] Teki R, Datta MK, Krishnan R, Parker TC, Lu T-M, Kumta PN, et al. Nanostructured Silicon Anodes for Lithium Ion Rechargeable Batteries. Small. 2009;5:2236-42.

- [14] Deng D, Kim MG, Lee JY, Cho J. Green energy storage materials: Nanostructured TiO2 and Sn-based anodes for lithium-ion batteries. Energy & Environmental Science. 2009;2:818-37.
- [15] Gruber PW, Medina PA, Keoleian GA, Kesler SE, Everson MP, Wallington TJ. Global Lithium Availability. Journal of Industrial Ecology. 2011;15:760-75.
- [16] Speirs J, Contestabile M, Houari Y, Gross R. The future of lithium availability for electric vehicle batteries. Renewable and Sustainable Energy Reviews. 2014;35:183-93.
- [17] Yoshino A. The Birth of the Lithium-Ion Battery. Angewandte Chemie International Edition. 2012;51:5798-800.
- [18] Deng D. Li-ion batteries: basics, progress, and challenges. Energy Science & Engineering. 2015;3:385-418.
- [19] Nitta N, Wu F, Lee JT, Yushin G. Li-ion battery materials: present and future. Materials Today. 2015;18:252-64.
- [20] Vikström H, Davidsson S, Höök M. Lithium availability and future production outlooks. Applied Energy. 2013;110:252-66.
- [21] Armand M, Tarascon JM. Building better batteries. Nature. 2008;451:652.
- [22] Goodenough JB. Evolution of Strategies for Modern Rechargeable Batteries. Accounts of Chemical Research. 2013;46:1053-61.
- [23] Wang Y, Xia Y. Recent Progress in Supercapacitors: From Materials Design to System Construction. Advanced Materials. 2013;25:5336-42.
- [24] Wang G, Zhang L, Zhang J. A review of electrode materials for electrochemical supercapacitors. Chemical Society Reviews. 2012;41:797-828.
- [25] Simon P, Gogotsi Y. Materials for electrochemical capacitors. Nature Materials. 2008;7:845.
- [26] Cheng JP, Zhang J, Liu F. Recent development of metal hydroxides as electrode material of electrochemical capacitors. RSC Advances. 2014;4:38893-917.
- [27] Zhang LL, Zhao XS. Carbon-based materials as supercapacitor electrodes. Chemical Society Reviews. 2009;38:2520-31.
- [28] Helmholtz H. Studien über electrische Grenzschichten. Annalen der Physik. 1879;243:337-82.
- [29] Frackowiak E. Carbon materials for supercapacitor application. Physical Chemistry Chemical Physics. 2007;9:1774-85.
- [30] Pandolfo AG, Hollenkamp AF. Carbon properties and their role in supercapacitors. Journal of Power Sources. 2006;157:11-27.
- [31] Feng X, Chen N, Zhang Y, Yan Z, Liu X, Ma Y, et al. The self-assembly of shape controlled functionalized graphene-MnO2 composites for application as supercapacitors. Journal of Materials Chemistry A. 2014;2:9178-84.
- [32] Lu Q, Chen JG, Xiao JQ. Nanostructured Electrodes for High-Performance Pseudocapacitors. Angewandte Chemie International Edition. 2013;52:1882-9.
- [33] Choudhary N, Li C, Moore J, Nagaiah N, Zhai L, Jung Y, et al. Asymmetric Supercapacitor Electrodes and Devices. Advanced Materials. 2017;29:1605336.
- [34] Rajkumar M, Hsu C-T, Wu T-H, Chen M-G, Hu C-C. Advanced materials for aqueous supercapacitors in the asymmetric design. Progress in Natural Science: Materials International. 2015;25:527-44.

- [35] Yang X, Niu H, Jiang H, Wang Q, Qu F. A high energy density all-solid-state asymmetric supercapacitor based on MoS2/graphene nanosheets and MnO2/graphene hybrid electrodes. Journal of Materials Chemistry A. 2016;4:11264-75.
- [36] Palanisamy S, Periasamy P, Subramani K, Shyma AP, Venkatachalam R. Ultrathin sheet structure Ni-MoS2 anode and MnO2/water dispersion graphene cathode for modern asymmetrical coin cell supercapacitor. Journal of Alloys and Compounds. 2018;731:936-44.
- [37] Jiang H, Li C, Sun T, Ma J. A green and high energy density asymmetric supercapacitor based on ultrathin MnO2 nanostructures and functional mesoporous carbon nanotube electrodes. Nanoscale. 2012;4:807-12.
- [38] Xia H, Meng YS, Yuan G, Cui C, Lu L. A Symmetric RuO2/RuO2 Supercapacitor Operating at 1.6 V by Using a Neutral Aqueous Electrolyte. Electrochemical and Solid-State Letters. 2012;15:A60-A3.
- [39] Yang P, Ding Y, Lin Z, Chen Z, Li Y, Qiang P, et al. Low-Cost High-Performance Solid-State Asymmetric Supercapacitors Based on MnO2 Nanowires and Fe2O3 Nanotubes. Nano Letters. 2014;14:731-6.
- [40] Cao J, Wang Y, Zhou Y, Ouyang J-H, Jia D, Guo L. High voltage asymmetric supercapacitor based on MnO2 and graphene electrodes. Journal of Electroanalytical Chemistry. 2013;689:201-6.
- [41] Chen H, Jiang J, Zhang L, Xia D, Zhao Y, Guo D, et al. In situ growth of NiCo2S4 nanotube arrays on Ni foam for supercapacitors: Maximizing utilization efficiency at high mass loading to achieve ultrahigh areal pseudocapacitance. Journal of Power Sources. 2014;254:249-57.
- [42] Yan J, Wang Q, Wei T, Fan Z. Recent Advances in Design and Fabrication of Electrochemical Supercapacitors with High Energy Densities. Advanced Energy Materials. 2014;4:1300816.
- [43] Eberle DU, von Helmolt DR. Sustainable transportation based on electric vehicle concepts: a brief overview. Energy & Environmental Science. 2010;3:689-99.
- [44] Zhang J, Zhao XS. On the Configuration of Supercapacitors for Maximizing Electrochemical Performance. ChemSusChem. 2012;5:818-41.
- [45] Sheng Z-H, Zheng X-Q, Xu J-Y, Bao W-J, Wang F-B, Xia X-H. Electrochemical sensor based on nitrogen doped graphene: Simultaneous determination of ascorbic acid, dopamine and uric acid. Biosensors and Bioelectronics. 2012;34:125-31.
- [46] Heien MLAV, Khan AS, Ariansen JL, Cheer JF, Phillips PEM, Wassum KM, et al. Real-time measurement of dopamine fluctuations after cocaine in the brain of behaving rats. Proceedings of the National Academy of Sciences of the United States of America. 2005;102:10023-8.
- [47] Dutt VVSE, Mottola HA. Determination of uric acid at the microgram level by a kinetic procedure based on a pseudo-induction period. Analytical Chemistry. 1974;46:1777-81.
- [48] Vellaichamy B, Periakaruppan P, Paulmony T. Evaluation of a New Biosensor Based on in Situ Synthesized PPy-Ag-PVP Nanohybrid for Selective Detection of Dopamine. The Journal of Physical Chemistry B. 2017;121:1118-27.
- [49] Han D, Han T, Shan C, Ivaska A, Niu L. Simultaneous Determination of Ascorbic Acid, Dopamine and Uric Acid with Chitosan-Graphene Modified Electrode. Electroanalysis. 2010;22:2001-8.

- [50] Mao Y, Bao Y, Han D, Li F, Niu L. Efficient one-pot synthesis of molecularly imprinted silica nanospheres embedded carbon dots for fluorescent dopamine optosensing. Biosensors and Bioelectronics. 2012;38:55-60.
- [51] Ye N, Gao T, Li J. Hollow fiber-supported graphene oxide molecularly imprinted polymers for the determination of dopamine using HPLC-PDA. Analytical Methods. 2014;6:7518-24.
- [52] Vuorensola K, Sirén H, Karjalainen U. Determination of dopamine and methoxycatecholamines in patient urine by liquid chromatography with electrochemical detection and by capillary electrophoresis coupled with spectrophotometry and mass spectrometry. Journal of Chromatography B. 2003;788:277-89.
- [53] Schöning MJ, Jacobs M, Muck A, Knobbe DT, Wang J, Chatrathi M, et al. Amperometric PDMS/glass capillary electrophoresis-based biosensor microchip for catechol and dopamine detection. Sensors and Actuators B: Chemical. 2005;108:688-94.
- [54] How GTS, Pandikumar A, Ming HN, Ngee LH. Highly exposed {001} facets of titanium dioxide modified with reduced graphene oxide for dopamine sensing. 2014;4:5044.
- [55] Ashoka NB, Swamy BEK, Jayadevappa H. Nanorod TiO2 sensor for dopamine: a voltammetric study. New Journal of Chemistry. 2017.
- [56] Di Chiara G, Bassareo V, Fenu S, De Luca MA, Spina L, Cadoni C, et al. Dopamine and drug addiction: the nucleus accumbens shell connection. Neuropharmacology. 2004;47:227-41.
- [57] Pandikumar A, Soon How GT, See TP, Omar FS, Jayabal S, Kamali KZ, et al. Graphene and its nanocomposite material based electrochemical sensor platform for dopamine. RSC Advances. 2014;4:63296-323.
- [58] Nobili A, Latagliata EC, Viscomi MT, Cavallucci V, Cutuli D, Giacovazzo G, et al. Dopamine neuronal loss contributes to memory and reward dysfunction in a model of Alzheimer's disease. 2017;8:14727.
- [59] Oak JN, Oldenhof J, Van Tol HHM. The dopamine D4 receptor: one decade of research. European Journal of Pharmacology. 2000;405:303-27.
- [60] Wang Y, Huang L, Zhang L, Qu Y, Mu D. Iron Status in Attention-Deficit/Hyperactivity Disorder: A Systematic Review and Meta-Analysis. PLoS ONE. 2017;12:e0169145.
- [61] Sakuta H, Suzuki K, Miyamoto T, Miyamoto M, Numao A, Fujita H, et al. Serum uric acid levels in Parkinson's disease and related disorders. Brain and Behavior. 2017;7:e00598-n/a.
- [62] Newman M. Uric Acid: Detection, Applications and Role in Health and Disease: Nova Science Publishers, Incorporated; 2016.
- [63] Pakapongpan S, Mensing JP, Phokharatkul D, Lomas T, Tuantranont A. Highly selective electrochemical sensor for ascorbic acid based on a novel hybrid graphene-copper phthalocyanine-polyaniline nanocomposites. Electrochimica Acta. 2014;133:294-301.
- [64] Yang L, Liu D, Huang J, You T. Simultaneous determination of dopamine, ascorbic acid and uric acid at electrochemically reduced graphene oxide modified electrode. Sensors and Actuators B: Chemical. 2014;193:166-72.
- [65] Arrigoni O, De Tullio MC. Ascorbic acid: much more than just an antioxidant. Biochimica et Biophysica Acta (BBA) General Subjects. 2002;1569:1-9.
- [66] Hemilä H. Vitamin C and Infections. Nutrients. 2017;9:339.

Introduction

[67] Padayatty SJ, Katz A, Wang Y, Eck P, Kwon O, Lee J-H, et al. Vitamin C as an Antioxidant: Evaluation of Its Role in Disease Prevention. Journal of the American College of Nutrition. 2003;22:18-35.

Chapter 2 Literature Review

2.1 Metal Oxide-FLG Composites as Anodes in LIBs

Rechargeable lithium ion batteries (LIBs) are the most reliable energy storage devices for laptops, mobile phones, and hybrid electric vehicles. Worldwide, a continuous effort for finding better anode materials for LIBs has been in progress. Recent studies focused on graphene-metal oxide nanocomposites that can overcome the drawbacks namely poor electrical conductivity, agglomeration, capacity fading, etc., of metal oxides as anode materials in LIBs. In addition, these nanocomposites can offer exceptionally high capacity, rate capability, and improved cycling stability. Among such nanocomposites, graphene $-A_2Mo_3O_8$ (where A = Mn, Fe, Co, Ni, Zn) have been drawing much attention owing to their unique performance in comparison to their constituents and many other compounds. Uniqueness in the performance of such nanocomposites is mainly owing to the crystal structure of A₂Mo₃O₈ compounds among which, Fe₂Mo₃O₈, Mn₂Mo₃O₈, Co₂Mo₃O, and Zn₂Mo₃O₈ are widely studied [1-14]. Laboratory-prepared A₂Mo₃O₈ compounds such as Fe₂Mo₃O₈ have a unique crystal structure with a hexagonal P63mc symmetry, which allows the MoO6 octahedral layers alternate with Fe-O₆ octahedral and Fe-O₄ tetrahedral layers of Fe-O honeycomb stacks along the c-axis. The Mo-O octahedron is constructed with Mo⁴⁺ ion in the centre and oxide ions surrounding it. Thus Fe₂Mo₃O₈ is structurally charge balanced rather than being stable stoichiometric wise. A₂Mo₃O₈ compounds store Li through a series of conversion reactions to yield very high Li storage capacities. For example, the typical conversion reactions that occur during lithiation of Fe₂Mo₃O₈ are

$$2Fe + 2Li_2O \leftrightarrow 2FeO + 4Li^+ + 4e^-$$
$$3Mo + 6Li_2O \leftrightarrow 3MoO_2 + 12Li^+ + 12e^-$$
$$Fe_2Mo_3O_8 + 16Li^+ + 16e^- \leftrightarrow 8Li_2O + 2Fe^0 + 3Mo^0$$

which involve 16 moles of Li insertion and extraction resulting in a high theoretical capacity of 813 mAh g⁻¹. Here, Mo₃–clusters play a major role in Li uptake. However, out of all the A₂Mo₃O₈ type compounds, Fe₂Mo₃O₈ is the least studied one for anodic application in Li-ion batteries. In the only study that is available on the use of Fe₂Mo₃O₈ in Li-ion battery application is about the use of Fe₂Mo₃O₈–reduced graphene oxide (RGO) composite as an anode material in Li-ion battery [15]. Fe₂Mo₃O₈–RGO composite performed excellently by exhibiting high discharge capacity of 835 mAh g⁻¹ (at a current density of 200 mAg⁻¹) even after 40th cycle. However, there is a need to synthesize Fe₂Mo₃O₈–RGO composite using easier and safer

methods. Herein, an easier one-pot synthesis of $Fe_2Mo_3O_8/Exfoliated$ Graphene Oxide (EG) and its use in anodic application in Li-ion battery are demonstrated. $Fe_2Mo_3O_8/FLG$ is synthesized by a solid-state method which was previously used to synthesize different RGO-metal oxide composites such as FLG -FeO, FLG-MnO, FLG-MoO₂, and few-layered graphene- $A_2Mo_3O_8$ (A = Co, Mn, Zn) composites. GTR method does not involve the use of any harmful or toxic chemicals. The reaction mixture is a dry powder mixture of GO, iron oxalate (FeC₂O₄·2H₂O) and MoO₃ in appropriate proportions. The main advantage of GTR approach is that the GO in the reaction mixture acts as a reducing agent as well as the source of FLG and because the method is a solid-state method, it facilitates the easy synthesis of bulk amounts of $Fe_2Mo_3O_8/FLG$. As-prepared $Fe_2Mo_3O_8/FLG$ composite is then tested as an anode material in Li-ion battery. As shown in Table 2.1 different types [16-20, 43] of rGO also performed very well as anode materials in Li-ion batteries.

2.2 Metal Oxide-FLG Composites as Electrodes in Supercapacitors

As shown in Table 2.2 different types [44-83] of rGO and different metal oxide-FLG composites performed very well as electrode materials in supercapacitors. In the context of this thesis, MnO and/or FLG containing composites are important. As-anticipated, due to FLG's high specific surface area, its contribution to the enhanced specific capacitance is known (Table 2.2). Different metal oxides [84-89] including manganese oxides (Mn_xO_x) [90-93] have also been independently used. Among Mn_xO_x, MnO is abundant, cheap, environmentally benign and more importantly it exhibits a very high theoretical specific capacitance of 1360 F/g [94-97]. The advantage of different possible oxidation states of Mn actively plays a role as oxidizing and reducing in redox systems and hence MnO is highly useful as electrode material in supercapacitors. However, due to poor processing methods (Table 2.2), MnO used to agglomerate and used to always suffer from poor cyclic stability, conductivity and loss of active surface sites [95,96]. One of the possible solutions to overcome the problems associated with MnO is to make a composite which contains MnO and graphenaceous materials such as FLG as in the present thesis work. Graphenaceous material in the composite is expected to enhance the charge transfer paths while providing a strong support for MnO particles and helping them not to agglomerate. Also, since such a composite does not have any binder as a constituent, the impedance across current collector/electrode is reduced. Lastly, by virtue of having MnO and EDLC type of material such as FLG in the composite, it exhibits high specific capacitance and excellent cyclic stability.

Table 2.1. Available literature on different rGOs and metal oxide-rGO composites as anode materials in Li-ion batteries.

Composite	Synthesis method	Potential	Current rate	Reversible capacity	Columbic efficiency
		window		(mAg^{-1})	(%)
S-RGO [16]	Solar irradiation	0.0 - 3.0	100 mA g ⁻¹	880	95
Thermal RGO [17]	Thermal reduction	0.0 - 4.0	100 mA g ⁻¹	1264	67
Chemical RGO [18]	Chemical reduction	0.01 - 3.0	1 C	650	70
S doped RGO [19]	Ionothermal	0.0-3.0	50 mA g ⁻¹	1400	98
N doped RGO [20]	Heat treatment	0.01 - 3.0	50 mA g	1043	43
B doped RGO [20]	Thermal	0.01 - 3.0	50 mA g	1549	55
RGO/Mn ₂ O ₃ [21]	Coprecipitatation	0.0 - 3.0	0.5 A g ⁻¹	1015	98
RGO/FeO [22]	Graphenothermal	0.005-3.0	50 mA g ⁻¹	857	98
RGO/Fe ₂ O ₃ [23]	Eelctrospun	0.005-3.0	0.1 C	820	96
C-Fe ₃ O ₄ [24]	Solvothermal	0.05 - 2.5	200 mAg ⁻¹	893	96
RGO/Fe ₃ O ₄ [25]	Micro wave	0.01 - 3	1 C	1272	98
RGO/Fe ₃ O ₄ [26]	Hydrothermal	0.0 - 3.0	0.5 A g ⁻¹	1108	
RGO/Fe ₂ O ₃ [27]	Micro wave	0.005-3.0	100 mA g ⁻¹	1227	
RGO/Fe ₃ O ₄ [28]	Hydrothermal	0.0 - 3.0	100 mA g ⁻¹	1032	61
RGO/Fe ₃ O ₄ /PANI [29]	Hydrothermal	0.0 - 3.0	0.1 A g ⁻¹	1214	96
Fe ₃ O ₄ /PANI [30]	Hydrothermal	0.05- 3.0	100 mA g ⁻¹	1350	98
Fe ₃ O ₄ /Fe/Carbon [31]	Sol-gel	0.0 - 3.0	50 mA g ⁻¹	600	98
RGO/ZnO [32]	Microwave	0.01-3.0	0.1 C	852	82
RGO/TiO ₂ [33]	Electrostatic	1.0 - 3.0	0.1 A g ⁻¹	262	100
RGO/MnO [34]	Wet chemical	0.01-3.0	0.2 A g ⁻¹	635	92
RGO/MnO [35]	Graphenothermal	0.005-3.0	75 mA g ⁻¹	936	99
RGO/MoO ₂ [36]	Graphenothermal	0.005-3.0	100 mA g ⁻¹	878	98
RGO/Zn ₂ Mo ₃ O ₈ [37]	Graphenothermal	0.005-3.0	60 mA g ⁻¹	448	58
RGO/Co ₂ Mo ₃ O ₈ [37]	Graphenothermal	0.005-3.0	60 mA g ⁻¹	907	67
Co ₂ Mo ₃ O ₈ [38]	Carbothermal	0.005-3.0	60 mA g ⁻¹	915	97
RGO/Co ₂ Mo ₃ O ₈ [39]	Graphenothermal	0.005- 3.0	60 mA g ⁻¹	1170	64
RGO/Mn ₂ Mo ₃ O ₈ [40]	Chemical	0.005- 3.0	60 mA g ⁻¹	932	69
RGO/Fe ₂ Mo ₃ O ₈ [41]	Chemical	0.005- 3.0	200 mA g ⁻¹	923	72
MgO/FLG [42]	Combustion	0.005- 3.0	1 C	1052	98
MWRGO [43]	Microwave	0.0 - 3.0	0.1 C	400	98

Table 2.2. Available literature on different rGOs and metal oxide-rGO composites for supercapacitors.

Electrode	Synthesis method	Potential	Electrolyte	Current	Specific capacitance
	,	window	J	density/Scan rate	(F/g)
RGO [44]	Chemical	0.0 -1.0	2 M H ₂ SO ₄	0.2 A g ⁻¹	141
ERGO [45]	Electrochemical	-1.0 -1.0	1 M Na ₂ SO ₄	10 mVS ⁻¹	136
TERGO [46]	Thermal reduction	-1.0 -1.0	0.1 M TEABF ₄	1 A g ⁻¹	85
CRGO [47]	Flame induced	-1.0 -1.0	6 M KOH	0.1 A g ⁻¹	260
HRGO [48]	Hydrothermal	-1.0 -1.0	1 M H ₂ SO ₄	1 A g ⁻¹	367
RGO/RuO ₂ [49]	Sol-gel	0.0 -1.0	1 M H ₂ SO ₄	1 A g ⁻¹	500
RGO/NiO [50]	Hydrothermal	0.0-0.6	1 M KOH	1 A g ⁻¹	387
RGO/Co ₃ O ₄ [51]	Hydrothermal	0.0-0.6	1 M KOH	200 mA g ⁻¹	278
RGO/CuO [52]	Green synthesis	-0.6 - 0.6	0.1 M H ₂ SO ₄	5 mVs^{-1}	185
RGO/SnO ₂ [53]	Wet chemical	-0.6 - 1	6 M KOH	5 mVs ⁻¹	818
RGO/MoO ₃ [54]	Hydrothermal	0-1	1M H ₂ SO ₄	0.2 A g ⁻¹	360
RGO/TiO ₂ [55]	Co-precipitation	-0.1-0.5	1 M Na ₂ SO ₄	5 mVs ⁻¹	192
RGO/ZnO [56]	Chemical	0.0-1.0	0.1 M Na ₂ SO ₄	1 Ag ⁻¹	308
RGO/Fe ₃ O ₄ [57]	Synthetic	-1.2 - 0.4	1 M KOH	5 A g ⁻¹	315
RGO/Fe ₃ O ₄ [58]	Solid state	-0.2 - 0.8	2 M KOH	10 mV s ⁻¹	498
RGO/CeO ₂ [59]	Co-precipitation	0.0 - 0.5	6 M KOH	3.0 A g ⁻¹	382
RGO/MgO [60]	CVD	0.0 -1.0	6 M KOH	0.5 A g ⁻¹	303
RGO/V ₂ O ₅ [61]	Microwave	0.0 - 0.8	1 M Na ₂ SO ₄	5 mVs^{-1}	250
RGO/MoS ₂ [62]	Hydrothermal	-1.0 -1.0	1 M Na ₂ SO ₄	1.2 A g ⁻¹	387
RGO/BiVO ₄ [63]	Hydrothermal	-0.0 - 0.6		0.15 mA g^{-1}	151
RGO/PEDOT [64]	Hydrothermal	-0.6 - 0.6	6 M KOH	10 mVS ⁻¹	102
RGO/PANI [65]	In-situ poly.	-0.4 – 1.2	1 M H ₂ SO ₄	100 mV S ⁻¹	250
RGO/PPy [66]	In-situ poly.	-0.4 - 0.6	1 M KCl	0.5 Ag^{-1}	557
RGO/SnO ₂ /PPy [67]	In-situ poly.	-0.2 - 0.5	1 M H ₂ SO ₄	1 mVS ⁻¹	616
CNT/RGO/PANI [68]	Chemical	-0.4 - 0.6	0.1 M NaNO ₃	0.1 A g ⁻¹	312
RGO/MoO ₃ /PANI [69]	Chemical	-0.4-0.6	1M H ₂ SO ₄	1 mVs ⁻¹	553
RGO/MOF/Co ₃ O ₄ [70]	Hydrothermal	-0.1 - 0.4	0.1 M KOH	4 A g ⁻¹	1300
RGO/CNT/MnO ₂ [71]	Hydrothermal	-0.2 - 0.8	1 M Na ₂ SO ₄	60 A g ⁻¹	222
Mn ₃ O ₄ [72]	Chemical	0.4 - 1.2	6 M KOH	1 A g ⁻¹	583
MnO ₂ /CeO ₂ [73]	Hydrothermal	-0.1 - 0.4	3 M KOH	500 mA g ⁻¹	273

Literature Review

MnO ₂ /TiO ₂ [74]	Electro deposition	0.0 - 1.2	0.1 M KOH	0.013 mA/cm ²	40 mF/cm ²
Carbon/MnO ₂ [75]	Hydrothermal	0.0-0.8	1.0 M NaOH	2 mVs^{-1}	252
Carbon/MnO [76]	Electro spinning	0.0 - 1.0	1 M Na ₂ SO ₄	1 A g ⁻¹	578
AC//Mn3O ₄ [77]	Calcination	0.0 - 1.0	1 M Na ₂ SO ₄	1 A g ⁻¹	522
AC//MnO ₂ [78]	Ultrasonication	0.0 - 3.0	1 M Et ₄ NBF ₄	10 mVs ⁻¹	228
RGO//MnO [79]	Microwave	-0.4 - 1.0	1M NaNO ₃	0.1 Ag ⁻¹	55
CNT/MnO ₂ [80]	Microwave	-0.2 - 1.0	1 M Na ₂ SO ₄	500 mVs ⁻¹	522
RGO/MnO ₂ [81]	Electrochemical	0.0 - 1.0	1 M Na ₂ SO ₄	$0.25~{\rm A~g^{-1}}$	473
RGO/Mn ₃ O ₄ [82]	Microwave	0.0 - 1.0	5 M NaOH	1 A g ⁻¹	344
VAGN/MnO [83]	MW-PECVD	0.0 - 1.0	0.5 M Na ₂ SO ₄	2 mVs^{-1}	790

2.3 Metal Oxide-FLG Composites for Electrochemical Detection of Dopamine

For the electrochemical detection of dopamine (DA), so far, researchers have prepared various metal and metal oxides decorated graphene. These works are tabulated in Table 2.3. Among the metal oxides, it has been touted that Fe₃O₄ could be excellent for electrochemical sensing [123].

Table 2.3. Available literature on electrochemical detection of interfering species dopamine (DA), ascorbic acid (AA), and uric acid (UA).

Electrode Material	Synthesis Method	Electrochemical Technique	Specie	Linearity (µM)	LOD (µM)
Fe ₃ O ₄ /RGO/GCE [98]	Wet chemical	DPV	AA	0.5-100	0.12
Fe ₃ O ₄ /GO/PG [99]	Co - precipitation	DPV	DA	3.0-30	0.18
Fe ₃ O ₄ /GCE [100]	Hydrothermal	DPV	DA	0.002-0.6	800
Fe ₃ O ₄ /CND/GCE [101]	Hydrothermal	DPV	DA	0.1-21	0.058
Fe ₃ O ₄ /GNS/Nafion/GCE [102]	Hydrothermal	DPV	DA	0.020-130	0.007
CQDS/Fe ₃ O ₄ /GCE [103]	Co – precipitation// hydrothermal	AM	UA	0.01-0.145	0.006
RGO/Fe ₃ O ₄ /GCE [104]	Sol-gel	AM	DA	0.010-0.270	0.005
RGO/TiO ₂ /GCE [105]	Wet chemical	AM	AA	1-1500	0.5
Fe ₃ O ₄ /Nafion/CPE [106]		DPV	DA	10-110	3.3
RGO/SnO ₂ [107]	Hydrothermal	DPV	DA, AA	5-50	1
Cu ₂ O/RGO [108]	Solvothermal		UA DA	1.0-138 0.05-109	0.112 0.15
Carbon/H-Fe ₃ O ₄ GCE	Solvothermal	DPV	DA AA	0.1-150 1.0-150	0.053 0.41
RGO/TiO ₂ /GCE [110]	Hydrothermal	DPV	DA AA	2-60 0.4-400	6 200
Fe ₃ O ₄ /Gr/GCE [111]	Hydrothermal	DPV	DA, UA, AC	5.0-160	0.78
RGO/GCE [112]	Chemical	DPV	DA UA AA	0.1-400 2-600 0.7-100	0.1 1 0.7
N doped RGO [113]	Thermal annealing	DPV	AA DA UA	5.0-130 0.5-170 0.1-20	2.2 0.2 0.045

Literature Review

			1	1
		DA	0.5-60	0.5
Electrochemical	DPV	UA	500-2000	300
		AA	0.5-60	0.5
Chemical	DPV	AA	4.0-4500	0.95
		DA	0.5-2000	0.12
		UA	0.8-2000	0.20
Electro deposition	DPV	AA	10-200	5.31
-		DA	0.2-8.0	0.04
		UA	0.2-16.0	0.17
		AA	6-350	1
Co precipitation	DPV	DA	0.5-50	0.1
		UA	1-90	0.2
		AC	0.4-32	0.05
		AA	5-235	0.24
CVD	DPV	DA	2.5-65	0.050
		UA	2.5-8.5	0.047
Solvothermal//	DPV	AA	5.0-1600	0.074
Hydrothermal		DA	0.2-38	0.126
		UA	1.8-850	0.056
One-pot	DPV	AA	50-2350	3.71
solution		UA	1-70	0.33
		DA	3-330	1.08
Solar	DPV	AA	150-300	30
irradiation		DA	0.44-3.3	0.12
		UA	2-15	0.46
CVD	DPV	AA	5.0-350	0.03
		DA	0.1-7	0.15
		UA	1-70	0.12
	Chemical Electro deposition Co precipitation CVD Solvothermal// Hydrothermal One-pot solution Solar irradiation	Chemical DPV Electro deposition DPV Co precipitation DPV CVD DPV Solvothermal// Hydrothermal One-pot solution DPV Solar irradiation DPV	Chemical DPV AA DA UA Electro deposition DPV AA Co precipitation DPV DA UA Co precipitation DPV DA UA AC AC AA CVD DPV DA UA Solvothermal// DPV AA Hydrothermal DPV AA Solution DPV AA Solution DPV AA Solution DPV AA CVD DPV AA UA CVD DPV AA UA DA CVD DPV AA SOlution DA UA DA CVD DPV AA DA	DPV

Note: AC: Acetaminophen, CND: Carbon nano dots, CQD: Carbon quantum dots, GCE: Glassy carbon electrode, SPE: screen printed electrode, DPV: Differential pulse voltammetry.

References

- [1] Cuny J, Gougeon P, Gall P. Redetermination of Zn(2)Mo(3)O(8). Acta Crystallographica Section E: Structure Reports Online. 2009;65:i51-i.
- [2] Biswas T, Ravindra P, Athresh E, Ranjan R, Avasthi S, Jain M. Optical Properties of $Zn_2Mo_3O_8$: Combination of Theoretical and Experimental Study. The Journal of Physical Chemistry C. 2017;121:24766-73.
- [3] Hibble SJ, Cooper SP, Patat S, Hannon AC. Total neutron diffraction: a route to the correct local structure of disordered LaMo₂O₅ and its application to the model compound Zn₂Mo₃O₈. Acta Crystallographica Section B. 1999;55:683-97.
- [4] Zhu Y, Zhong Y, Chen G, Deng X, Cai R, Li L, et al. A hierarchical Zn₂Mo₃O₈ nanodots-porous carbon composite as a superior anode for lithium-ion batteries. Chemical Communications. 2016;52:9402-5.
- [5] Torardi CC, McCarley RE. Synthesis, crystal structures, and properties of lithium zinc molybdenum oxide (LiZn₂Mo₃O₈), zinc molybdenum oxide (Zn3Mo₃O₈), and scandium zinc molybdenum oxide (ScZnMo₃O₈), reduced derivatives containing the Mo₃O₁₃ cluster unit. Inorganic Chemistry. 1985;24:476-81.
- [6] Kanazawa Y, Sasaki A. Structure of kamiokite. Acta Crystallographica Section C. 1986;42:9-11.
- [7] Le Page Y, Strobel P. Structure of iron(II) molybdenum(IV) oxide Fe₂Mo₃O₈. Acta Crystallographica Section B. 1982;38:1265-7.
- [8] Koyama K, Morishita M, Harada T, Maekawa N. Determination of standard gibbs energies of formation of Fe₂Mo₃O₁₂, Fe₂Mo₃O₈, Fe₂MoO₄, and FeMoO₄ of the Fe-Mo-O ternary system and μ phase of the Fe-Mo binary system by electromotive force measurement using a Y₂O₃-stabilized ZrO₂ solid electrolyte. Metallurgical and Materials Transactions B. 2003;34:653-9.
- [9] Das B, Reddy MV, Krishnamoorthi C, Tripathy S, Mahendiran R, Rao GVS, et al. Carbothermal synthesis, spectral and magnetic characterization and Li-cyclability of the Mocluster compounds, LiYMo3O8 and Mn₂Mo₃O₈. Electrochimica Acta. 2009;54:3360-73.
- [10] Das B, Reddy MV, Tripathy S, Chowdari BVR. A disc-like Mo-metal cluster compound, Co₂Mo₃O₈, as a high capacity anode for lithium ion batteries. RSC Advances. 2014;4:33883-9.
- [11] Marka SK, Petnikota S, Srikanth VVSS, Reddy MV, Adams S, Chowdari BVR. Co2Mo3O8/reduced graphene oxide composite: synthesis, characterization, and its role as a prospective anode material in lithium ion batteries. RSC Advances. 2016;6:55167-75.
- [12] Petnikota S, Marka SK, Srikanth VVSS, Reddy MV, Chowdari BVR. Elucidation of few layered graphene-complex metal oxide (A₂Mo₃O₈, A=Co, Mn and Zn) composites as robust anode materials in Li ion batteries. Electrochimica Acta. 2015;178:699-708.
- [13] Sun Y, Hu X, Luo W, Huang Y. Hierarchical Self-assembly of Mn₂Mo₃O₈-graphene Nanostructures and their Enhanced Lithium-storage Properties. Journal of Materials Chemistry. 2011;21:17229-35.
- [14] McAlister SP, Strobel P. Magnetic order in $M_2Mo_3O_8$ single crystals (M = Mn, Fe, Co, Ni). Journal of Magnetism and Magnetic Materials. 1983;30:340-8.
- [15] Sun Y, Hu X, Luo W, Shu J, Huang Y. Self-assembly of hybrid Fe₂Mo₃O₈-reduced graphene oxide nanosheets with enhanced lithium storage properties. Journal of Materials

- Chemistry A. 2013;1:4468-74.
- [16] Puttapati SK, Gedela V, Srikanth VVSS, Reddy MV, Adams S, Chowdari BVR. Unique reduced graphene oxide as efficient anode material in Li ion battery. Bulletin of Materials Science. 2018;41:53.
- [17] Lian P, Zhu X, Liang S, Li Z, Yang W, Wang H. Large reversible capacity of high quality graphene sheets as an anode material for lithium-ion batteries. Electrochimica Acta. 2010;55:3909-14.
- [18] Wang G, Shen X, Yao J, Park J. Graphene nanosheets for enhanced lithium storage in lithium ion batteries. Carbon. 2009;47:2049-53.
- [19] Yan Y, Yin Y-X, Xin S, Guo Y-G, Wan L-J. Ionothermal synthesis of sulfur-doped porous carbons hybridized with graphene as superior anode materials for lithium-ion batteries. Chemical Communications. 2012;48:10663-5.
- [20] Wu Z-S, Ren W, Xu L, Li F, Cheng H-M. Doped Graphene Sheets As Anode Materials with Superhigh Rate and Large Capacity for Lithium Ion Batteries. ACS Nano. 2011;5:5463-71.
- [21] Jadhav HS, Thorat GM, Kale BB, Seo JG. Mesoporous Mn₂O₃/reduced graphene oxide (rGO) composite with enhanced electrochemical performance for Li-ion battery. Dalton Transactions. 2017;46:9777-83.
- [22] Petnikota S, Marka SK, Banerjee A, Reddy MV, Srikanth VVSS, Chowdari BVR. Graphenothermal reduction synthesis of 'exfoliated graphene oxide/iron (II) oxide' composite for anode application in lithium ion batteries. Journal of Power Sources. 2015;293:253-63.
- [23] Zhang X, Liu H, Petnikota S, Ramakrishna S, Fan HJ. Electrospun Fe₂O₃—carbon composite nanofibers as durable anode materials for lithium ion batteries. Journal of Materials Chemistry A. 2014;2:10835-41.
- [24] Chen JS, Zhang Y, Lou XW. One-Pot Synthesis of Uniform Fe₃O₄ Nanospheres with Carbon Matrix Support for Improved Lithium Storage Capabilities. ACS Applied Materials & Interfaces. 2011;3:3276-9.
- [25] Bhuvaneswari S, Pratheeksha PM, Anandan S, Rangappa D, Gopalan R, Rao TN. Efficient reduced graphene oxide grafted porous Fe3O4 composite as a high performance anode material for Li-ion batteries. Physical Chemistry Chemical Physics. 2014;16:5284-94.
- [26] Zhu S, Fan L, Lu Y. Highly uniform Fe₃O₄ nanoparticle–rGO composites as anode materials for high performance lithium-ion batteries. RSC Advances. 2017;7:54939-46.
- [27] Zhu X, Zhu Y, Murali S, Stoller MD, Ruoff RS. Nanostructured Reduced Graphene Oxide/Fe₂O₃ Composite As a High-Performance Anode Material for Lithium Ion Batteries. ACS Nano. 2011;5:3333-8.
- [28] Huang W, Xiao X, Engelbrekt C, Zhang M, Li S, Ulstrup J, et al. Graphene encapsulated Fe₃O₄ nanorods assembled into a mesoporous hybrid composite used as a high-performance lithium-ion battery anode material. Materials Chemistry Frontiers. 2017;1:1185-93.
- [29] Bahadur A, Iqbal S, Shoaib M, Saeed A. Electrochemical study of specially designed graphene-Fe₃O₄-polyaniline nanocomposite as a high-performance anode for lithium-ion battery. Dalton Transactions. 2018;47:15031-7.
- [30] Wang X, Liu Y, Han H, Zhao Y, Ma W, Sun H. Polyaniline coated Fe₃O₄ hollow nanospheres as anode materials for lithium ion batteries. Sustainable Energy & Fuels. 2017;1:915-22.

- [31] Zhao X, Xia D, Zheng K. Fe₃O₄/Fe/Carbon Composite and Its Application as Anode Material for Lithium-Ion Batteries. ACS Applied Materials & Interfaces. 2012;4:1350-6.
- [32] Hsieh C-T, Lin C-Y, Chen Y-F, Lin J-S. Synthesis of ZnO@Graphene composites as anode materials for lithium ion batteries. Electrochimica Acta. 2013;111:359-65.
- [33] Zheng P, Liu T, Su Y, Zhang L, Guo S. TiO₂ nanotubes wrapped with reduced graphene oxide as a high-performance anode material for lithium-ion batteries. Scientific Reports. 2016;6:36580.
- [34] Hsieh C-T, Lin C-Y, Lin J-Y. High reversibility of Li intercalation and de-intercalation in MnO-attached graphene anodes for Li-ion batteries. Electrochimica Acta. 2011;56:8861-7.
- [35] Petnikota S, Srikanth VVSS, Nithyadharseni P, Reddy MV, Adams S, Chowdari BVR. Sustainable graphenothermal reduction chemistry to obtain MnO nanonetwork supported exfoliated graphene oxide composite and its electrochemical characteristics. ACS Sustainable Chemistry & Engineering. 2015;3:3205-13.
- [36] Petnikota S, Teo KW, Chen L, Sim A, Marka SK, Reddy MV, et al. Exfoliated graphene oxide/MoO₂ composites as anode materials in lithium-ion batteries: An insight into intercalation of li and conversion mechanism of MoO₂. ACS Applied Materials & Interfaces. 2016;8:10884-96.
- [37] Petnikota S, Marka SK, Srikanth VVSS, Reddy MV, Chowdari BVR. Elucidation of few layered graphene-complex metal oxide ($A_2Mo_3O_8$, A = Co, Mn and Zn) composites as robust anode materials in Li ion batteries. Electrochimica Acta. 2015;178:699-708.
- [38] Park S, An J, Jung I, Piner RD, An SJ, Li X, et al. Colloidal Suspensions of Highly Reduced Graphene Oxide in a Wide Variety of Organic Solvents. Nano Letters. 2009;9:1593-7.
- [39] Green AA, Hersam MC. Solution Phase Production of Graphene with Controlled Thickness via Density Differentiation. Nano Letters. 2009;9:4031-6.
- [40] Achee TC, Sun W, Hope JT, Quitzau SG, Sweeney CB, Shah SA, et al. High-yield scalable graphene nanosheet production from compressed graphite using electrochemical exfoliation. Scientific Reports. 2018;8:14525.
- [41] Chakrabarti A, Lu J, Skrabutenas JC, Xu T, Xiao Z, Maguire JA, et al. Conversion of carbon dioxide to few-layer graphene. Journal of Materials Chemistry. 2011;21:9491-3.
- [42] Petnikota S, Rotte NK, Reddy MV, Srikanth VVSS, Chowdari BVR. MgO-Decorated Few-Layered Graphene as an Anode for Li-Ion Batteries. ACS Applied Materials & Interfaces. 2015;7:2301-9.
- [43] Petnikota S, Rotte NK, Srikanth VVSS, Kota BSR, Reddy MV, Loh KP, et al. Electrochemical studies of few-layered graphene as an anode material for Li ion batteries. Journal of Solid State Electrochemistry. 2014;18:941-9.
- [44] Rajagopalan B, Chung JS. Reduced chemically modified graphene oxide for supercapacitor electrode. Nanoscale Research Letters. 2014;9:535.
- [45] Liu X, Qi X, Zhang Z, Ren L, Hao G, Liu Y, et al. Electrochemically reduced graphene oxide with porous structure as a binder-free electrode for high-rate supercapacitors. RSC Advances. 2014;4:13673-9.
- [46] Nam PT, Van Khanh N, Thom NT, Phuong NT, Van Trang N, Xuyen NT, et al. Synthesis of reduced graphene oxide for high-performance supercapacitor. Vietnam Journal of Chemistry. 2018;56:778-85.

- [47] Liu Y-Z, Chen C-M, Li Y-F, Li X-M, Kong Q-Q, Wang M-Z. Crumpled reduced graphene oxide by flame-induced reduction of graphite oxide for supercapacitive energy storage. Journal of Materials Chemistry A. 2014;2:5730-7.
- [48] Johra FT, Jung W-G. Hydrothermally reduced graphene oxide as a supercapacitor. Applied Surface Science. 2015;357:1911-4.
- [49] Amir FZ, Pham VH, Dickerson JH. Facile synthesis of ultra-small ruthenium oxide nanoparticles anchored on reduced graphene oxide nanosheets for high-performance supercapacitors. RSC Advances. 2015;5:67638-45.
- [50] Feng X, Zhou J, Wang L, Li Y, Huang Z, Chen S, et al. Synthesis of shape-controlled NiO–graphene nanocomposites with enhanced supercapacitive properties. New Journal of Chemistry. 2015;39:4026-34.
- [51] Numan A, Duraisamy N, Saiha Omar F, Mahipal YK, Ramesh K, Ramesh S. Enhanced electrochemical performance of cobalt oxide nanocube intercalated reduced graphene oxide for supercapacitor application. RSC Advances. 2016;6:34894-902.
- [52] Sudhakar YN, Hemant H, Nitinkumar SS, Poornesh P, Selvakumar M. Green synthesis and electrochemical characterization of rGO–CuO nanocomposites for supercapacitor applications. Ionics. 2017;23:1267-76.
- [53] Velmurugan V, Srinivasarao U, Ramachandran R, Saranya M, Grace AN. Synthesis of tin oxide/graphene (SnO2/G) nanocomposite and its electrochemical properties for supercapacitor applications. Materials Research Bulletin. 2016;84:145-51.
- [54] Zhou J, Song J, Li H, Feng X, Huang Z, Chen S, et al. The synthesis of shape-controlled α -MoO3/graphene nanocomposites for high performance supercapacitors. New Journal of Chemistry. 2015;39:8780-6.
- [55] Fulari AV, Ramana Reddy MV, Jadhav ST, Ghodake GS, Kim D-Y, Lohar GM. TiO₂/reduced graphene oxide composite based nano-petals for supercapacitor application: effect of substrate. Journal of Materials Science: Materials in Electronics. 2018;29:10814-24.
- [56] Chen Y-L, Hu Z-A, Chang Y-Q, Wang H-W, Zhang Z-Y, Yang Y-Y, et al. Zinc Oxide/Reduced Graphene Oxide Composites and Electrochemical Capacitance Enhanced by Homogeneous Incorporation of Reduced Graphene Oxide Sheets in Zinc Oxide Matrix. The Journal of Physical Chemistry C. 2011;115:2563-71.
- [57] Das AK, Sahoo S, Arunachalam P, Zhang S, Shim J-J. Facile synthesis of Fe₃O₄ nanorod decorated reduced graphene oxide (RGO) for supercapacitor application. RSC Advances. 2016;6:107057-64.
- [58] Rosaiah P, Zhu J, Hussain OM, Qiu Y. Facile and cost-effective synthesis of flower-like RGO/Fe3O4 nanocomposites with ultra-long cycling stability for supercapacitors. Ionics. 2019;25:655-64.
- [59] Deng D, Chen N, Xiao X, Du S, Wang Y. Electrochemical performance of CeO₂ nanoparticle-decorated graphene oxide as an electrode material for supercapacitor. Ionics. 2017;23:121-9.
- [60] Wang H, Sun X, Liu Z, Lei Z. Creation of nanopores on graphene planes with MgO template for preparing high-performance supercapacitor electrodes. Nanoscale. 2014;6:6577-84.
- [61] Ramadoss A, Saravanakumar B, Kim SJ. Vanadium Pentoxide/Reduced Graphene Oxide Composite as an Efficient Electrode Material for High-Performance Supercapacitors and Self-

- Powered Systems. Energy Technology. 2015;3:913-24.
- [62] Saraf M, Natarajan K, Mobin SM. Emerging Robust Heterostructure of MoS₂–rGO for High-Performance Supercapacitors. ACS Applied Materials & Interfaces. 2018;10:16588-95.
- [63] Patil SS, Dubal DP, Deonikar VG, Tamboli MS, Ambekar JD, Gomez-Romero P, et al. Fern-like rGO/BiVO₄ Hybrid Nanostructures for High-Energy Symmetric Supercapacitor. ACS Applied Materials & Interfaces. 2016;8:31602-10.
- [64] Ahmed S, Rafat M. Hydrothermal synthesis of PEDOT/rGO composite for supercapacitor applications. Materials Research Express. 2018;5:015507.
- [65] Kumar NA, Choi H-J, Shin YR, Chang DW, Dai L, Baek J-B. Polyaniline-Grafted Reduced Graphene Oxide for Efficient Electrochemical Supercapacitors. ACS Nano. 2012;6:1715-23.
- [66] Qian T, Yu C, Wu S, Shen J. A facilely prepared polypyrrole—reduced graphene oxide composite with a crumpled surface for high performance supercapacitor electrodes. Journal of Materials Chemistry A. 2013;1:6539-42.
- [67] Wang W, Hao Q, Lei W, Xia X, Wang X. Graphene/SnO₂/polypyrrole ternary nanocomposites as supercapacitor electrode materials. RSC Advances. 2012;2:10268-74.
- [68] Kumar MS, Yasoda KY, Batabyal SK, Kothurkar NK. Carbon-polyaniline nanocomposites as supercapacitor materials. Materials Research Express. 2018;5:045505.
- [69] Xia X, Hao Q, Lei W, Wang W, Wang H, Wang X. Reduced-graphene oxide/molybdenum oxide/polyaniline ternary composite for high energy density supercapacitors: Synthesis and properties. Journal of Materials Chemistry. 2012;22:8314-20.
- [70] Vilian ATE, Dinesh B, Rethinasabapathy M, Hwang S-K, Jin C-S, Huh YS, et al. Hexagonal Co₃O₄ anchored reduced graphene oxide sheets for high-performance supercapacitors and non-enzymatic glucose sensing. Journal of Materials Chemistry A. 2018;6:14367-79.
- [71] Jiang H, Dai Y, Hu Y, Chen W, Li C. Nanostructured Ternary Nanocomposite of rGO/CNTs/MnO₂ for High-Rate Supercapacitors. ACS Sustainable Chemistry & Engineering. 2014;2:70-4.
- [72] Luo Y, Yang T, Li Z, Xiao B, Zhang M. High performance of Mn_3O_4 cubes for supercapacitor applications. Materials Letters. 2016;178:171-4.
- [73] Zhang H, Gu J, Tong J, Hu Y, Guan B, Hu B, et al. Hierarchical porous MnO₂/CeO₂ with high performance for supercapacitor electrodes. Chemical Engineering Journal. 2016;286:139-49.
- [74] Huang Y-G, Zhang X-H, Chen X-B, Wang H-Q, Chen J-R, Zhong X-X, et al. Electrochemical properties of MnO2-deposited TiO₂ nanotube arrays 3D composite electrode for supercapacitors. International Journal of Hydrogen Energy. 2015;40:14331-7.
- [75] Zhao Y, Meng Y, Jiang P. Carbon@MnO₂ core—shell nanospheres for flexible high-performance supercapacitor electrode materials. Journal of Power Sources. 2014;259:219-26.
- [76] Ramadan M, Abdellah AM, Mohamed SG, Allam NK. 3D Interconnected Binder-Free Electrospun MnO@C Nanofibers for Supercapacitor Devices. Scientific Reports. 2018;8:7988.
- [77] Nagamuthu S, Vijayakumar S, Muralidharan G. Synthesis of Mn₃O₄/Amorphous Carbon Nanoparticles as Electrode Material for High Performance Supercapacitor Applications. Energy & Fuels. 2013;27:3508-15.

- [78] Wang H-Q, Li Z-S, Huang Y-G, Li Q-Y, Wang X-Y. A novel hybrid supercapacitor based on spherical activated carbon and spherical MnO2 in a non-aqueous electrolyte. Journal of Materials Chemistry. 2010;20:3883-9.
- [79] Antiohos D, Pingmuang K, Romano MS, Beirne S, Romeo T, Aitchison P, et al. Manganosite–microwave exfoliated graphene oxide composites for asymmetric supercapacitor device applications. Electrochimica Acta. 2013;101:99-108.
- [80] Yan J, Fan Z, Wei T, Cheng J, Shao B, Wang K, et al. Carbon nanotube/MnO₂ composites synthesized by microwave-assisted method for supercapacitors with high power and energy densities. Journal of Power Sources. 2009;194:1202-7.
- [81] Ali GAM, Yusoff MM, Algarni H, Chong KF. One-step electrosynthesis of MnO₂/rGO nanocomposite and its enhanced electrochemical performance. Ceramics International. 2018;44:7799-807.
- [82] Zhang H, Huang Z, Li Y, Chen Y, Wang W, Ye Y, et al. Microwave-assisted in situ synthesis of reduced graphene oxide/Mn₃O₄ composites for supercapacitor applications. RSC Advances. 2015;5:45061-7.
- [83] Liao Q, Li N, Cui H, Wang C. Vertically-aligned graphene@MnO nanosheets as binder-free high-performance electrochemical pseudocapacitor electrodes. Journal of Materials Chemistry A. 2013;1:13715-20.
- [84] Soudan, P., Gaudet, J., Guay, D., Bélanger, D. & Schulz, R. Electrochemical Properties of Ruthenium-Based Nanocrystalline Materials as Electrodes for Supercapacitors. Chemistry of Materials 14, 1210–1215, https://doi.org/10.1021/cm010721c (2002).
- [85] Yu, M. et al. Valence-Optimized Vanadium Oxide Supercapacitor Electrodes Exhibit Ultrahigh Capacitance and Super-Long Cyclic Durability of 100000 Cycles. Advanced Functional Materials 25, 3534–3540, https://doi.org/10.1002/adfm.201501342 (2015).
- [86] Ren, X. et al. Facile Synthesis of Hierarchical Mesoporous Honeycomb-like NiO for Aqueous Asymmetric Supercapacitors. ACS Applied Materials & Interfaces 7, 19930–19940, https://doi.org/10.1021/acsami.5b04094 (2015).
- [87] Pawar, S. M. et al. Multi-functional reactively-sputtered copper oxide electrodes for supercapacitor and electro-catalyst in direct methanol fuel cell applications. Scientific reports 6, 21310, https://doi.org/10.1038/srep21310 (2016).
- [88] Iqbal, N. et al. Flexible Fe3O4@Carbon Nanofibers Hierarchically Assembled with MnO2 Particles for High-Performance Supercapacitor Electrodes. Scientific Reports 7, 15153, https://doi.org/10.1038/s41598-017-15535-x (2017).
- [89] Banerjee, A. N., Anitha, V. C. & Joo, S. W. Improved electrochemical properties of morphology-controlled titania/titanate nanostructures prepared by in-situ hydrothermal surface modification of self-source Ti substrate for high-performance supercapacitors. Scientific Reports 7, 13227, https://doi.org/10.1038/s41598-017-11346-2 (2017).
- [90] Wei, W., Cui, X., Chen, W. & Ivey, D. G. Manganese oxide-based materials as electrochemical supercapacitor electrodes. Chemical Society Reviews 40, 1697–1721, https://doi.org/10.1039/C0CS00127A (2011).
- [91] Wei, C. et al. Two-Dimensional β-MnO2 Nanowire Network with Enhanced Electrochemical Capacitance. Scientific Reports 3, 2193, https://doi.org/10.1038/srep02193 (2013).
- [92] Sun, P. et al. Ultrathin MnO2 nanoflakes deposited on carbon nanotube networks for

- symmetrical supercapacitors with enhanced performance. Journal of Power Sources 341, 27–35, https://doi.org/10.1016/j.jpowsour.2016.11.112 (2017).
- [93] Kim, G., Ryu, I. & Yim, S. Retarded saturation of the areal capacitance using 3D-aligned MnO2 thin film nanostructures as a supercapacitor electrode. Scientific Reports 7, 8260, https://doi.org/10.1038/s41598-017-09039-x (2017).
- [94] Yang, M. et al. Ultrasmall MnO@N-rich carbon nanosheets for high-power asymmetric supercapacitors. Journal of Materials Chemistry A 2, 12519–12525, https://doi.org/10.1039/C4TA02055C (2014).
- [95] Liao, Q., Li, N., Cui, H. & Wang, C. Vertically-aligned graphene@MnO nanosheets as binder-free high-performance electrochemical pseudocapacitor electrodes. Journal of Materials Chemistry A 1, 13715–13720, https://doi.org/10.1039/C3TA13102E (2013).
- [96] Sun, G. et al. Rational design of uniformly embedded metal oxide nanoparticles into nitrogen-doped carbon aerogel for highperformance asymmetric supercapacitors with a high operating voltage window. Journal of Materials Chemistry A 4, 16576–16587, https://doi.org/10.1039/C6TA07240B (2016).
- [97] Qu, D. et al. Synthesis of MnO nano-particle@Flourine doped carbon and its application in hybrid supercapacitor. Applied Surface Science 413, 344–350, https://doi.org/10.1016/j.apsusc.2017.03.305 (2017).
- [98] Peik-See T, Pandikumar A, Nay-Ming H, Hong-Ngee L, Sulaiman Y. Simultaneous electrochemical detection of dopamine and ascorbic acid using an iron oxide/reduced graphene oxide modified glassy carbon electrode. Sensors (Basel). 2014;14:15227-43.
- [99] Cai L, Hou B, Shang Y, Xu L, Zhou B, Jiang X, et al. Synthesis of Fe3O4/graphene oxide/pristine graphene ternary composite and fabrication electrochemical sensor to detect dopamine and hydrogen peroxide. Chemical Physics Letters. 2019;736:136797.
- [100] Huang Y, Zhang Y, Liu D, Li M, Yu Y, Yang W, et al. Facile synthesis of highly ordered mesoporous Fe3O4 with ultrasensitive detection of dopamine. Talanta. 2019;201:511-8.
- [101] Luo N, Yang Z, Tang F, Wang D, Feng M, Liao X, et al. Fe3O4/Carbon Nanodot Hybrid Nanoparticles for the Indirect Colorimetric Detection of Glutathione. ACS Applied Nano Materials. 2019;2:3951-9.
- [102] Zhang W, Zheng J, Shi J, Lin Z, Huang Q, Zhang H, et al. Nafion covered core—shell structured Fe3O4@graphene nanospheres modified electrode for highly selective detection of dopamine. Analytica Chimica Acta. 2015;853:285-90.
- [103] Abbas MW, Soomro RA, Kalwar NH, Zahoor M, Avci A, Pehlivan E, et al. Carbon quantum dot coated Fe3O4 hybrid composites for sensitive electrochemical detection of uric acid. Microchemical Journal. 2019;146:517-24.
- [104] Rani GJ, Babu KJ, kumar GG, Rajan MAJ. Watsonia meriana flower like Fe3O4/reduced graphene oxide nanocomposite for the highly sensitive and selective electrochemical sensing of dopamine. Journal of Alloys and Compounds. 2016;688:500-12.
- [105] Fu L, Zheng Y-H, Fu Z-X. Ascorbic acid amperometric sensor using a graphene-wrapped hierarchical TiO2 nanocomposite. Chemical Papers2015. p. 655.
- [106] Lai G-S, Zhang H-L, Han D-Y. Electrocatalytic Response of Dopamine at an Iron Nanoparticles—Nafion—Modified Carbon Paste Electrode. Analytical Letters. 2008;41:3088-99.
- [107] Nurzulaikha R, Lim HN, Harrison I, Lim SS, Pandikumar A, Huang NM, et al. Graphene/SnO2 nanocomposite-modified electrode for electrochemical detection of dopamine. Sensing and Bio-Sensing Research. 2015;5:42-9.

- [108] Mei L-P, Feng J-J, Wu L, Chen J-R, Shen L, Xie Y, et al. A glassy carbon electrode modified with porous Cu2O nanospheres on reduced graphene oxide support for simultaneous sensing of uric acid and dopamine with high selectivity over ascorbic acid. Microchimica Acta. 2016;183:2039-46.
- [109] Song H, Xue G, Zhang J, Wang G, Ye B-C, Sun S, et al. Simultaneous voltammetric determination of dopamine and uric acid using carbon-encapsulated hollow Fe3O4 nanoparticles anchored to an electrode modified with nanosheets of reduced graphene oxide. Microchimica Acta. 2017;184:843-53.
- [110] How GTS, Pandikumar A, Ming HN, Ngee LH. Highly exposed {001} facets of titanium dioxide modified with reduced graphene oxide for dopamine sensing. Scientific Reports. 2014;4:5044.
- [111] Venkataprasad G, Madhusudana Reddy T, Lakshmi Narayana A, Hussain OM, Shaikshavali P, Venu Gopal T, et al. A facile synthesis of Fe3O4-Gr nanocomposite and its effective use as electrochemical sensor for the determination of dopamine and as anode material in lithium ion batteries. Sensors and Actuators A: Physical. 2019;293:87-100.
- [112] Wang H, Ren F, Wang C, Yang B, Bin D, Zhang K, et al. Simultaneous determination of dopamine, uric acid and ascorbic acid using a glassy carbon electrode modified with reduced graphene oxide. RSC Advances. 2014;4:26895-901.
- [113] Sheng Z-H, Zheng X-Q, Xu J-Y, Bao W-J, Wang F-B, Xia X-H. Electrochemical sensor based on nitrogen doped graphene: Simultaneous determination of ascorbic acid, dopamine and uric acid. Biosensors and Bioelectronics. 2012;34:125-31.
- [114] Yang L, Liu D, Huang J, You T. Simultaneous determination of dopamine, ascorbic acid and uric acid at electrochemically reduced graphene oxide modified electrode. Sensors and Actuators B: Chemical. 2014;193:166-72.
- [115] Ping J, Wu J, Wang Y, Ying Y. Simultaneous determination of ascorbic acid, dopamine and uric acid using high-performance screen-printed graphene electrode. Biosensors and Bioelectronics. 2012;34:70-6.
- [116] Zhang Y, Ji Y, Wang Z, Liu S, Zhang T. Electrodeposition synthesis of reduced graphene oxide—carbon nanotube hybrids on indium tin oxide electrode for simultaneous electrochemical detection of ascorbic acid, dopamine and uric acid. RSC Advances. 2015;5:106307-14.
- [117] Liu M, Chen Q, Lai C, Zhang Y, Deng J, Li H, et al. A double signal amplification platform for ultrasensitive and simultaneous detection of ascorbic acid, dopamine, uric acid and acetaminophen based on a nanocomposite of ferrocene thiolate stabilized Fe3O4@Au nanoparticles with graphene sheet. Biosensors and Bioelectronics. 2013;48:75-81.
- [118] Fernandes DM, Costa M, Pereira C, Bachiller-Baeza B, Rodríguez-Ramos I, Guerrero-Ruiz A, et al. Novel electrochemical sensor based on N-doped carbon nanotubes and Fe3O4 nanoparticles: Simultaneous voltammetric determination of ascorbic acid, dopamine and uric acid. Journal of Colloid and Interface Science. 2014;432:207-13.
- [119] Wu D, Li Y, Zhang Y, Wang P, Wei Q, Du B. Sensitive Electrochemical Sensor for Simultaneous Determination of Dopamine, Ascorbic Acid, and Uric Acid Enhanced by Aminogroup Functionalized Mesoporous Fe3O4@Graphene Sheets. Electrochimica Acta. 2014;116:244-9.
- [120] Zhang X, Zhang Y-C, Ma L-X. One-pot facile fabrication of graphene-zinc oxide composite and its enhanced sensitivity for simultaneous electrochemical detection of ascorbic acid, dopamine and uric acid. Sensors and Actuators B: Chemical. 2016;227:488-96.
- [121] Nancy TEM, Kumary VA. Synergistic electrocatalytic effect of graphene/nickel hydroxide composite for the simultaneous electrochemical determination of ascorbic acid, dopamine and uric acid. Electrochimica Acta. 2014;133:233-40.
- [122] Zhao L, Li H, Gao S, Li M, Xu S, Li C, et al. MgO nanobelt-modified graphene-tantalum wire electrode for the simultaneous determination of ascorbic acid, dopamine and uric acid.

Literature Review

Electrochimica Acta. 2015;168:191-8.

[123] Wu W, Wu Z, Yu T, Jiang C, Kim WS. Recent progress on magnetic iron oxide nanoparticles: synthesis, surface functional strategies and biomedical applications. Science and technology of advanced materials. 2015;16:023501.

Chapter 3 Experimental Details

3.1 Synthesis of Materials

3.1.1 Graphene Oxide

Graphene oxide (GO) was prepared by using conventional Hummers method by slight modifications. In brief, natural Graphite flakes (size ≤ 47 µm) of 1 g were in 69 mL of concentrated sulfuric acid (H2SO4) for intercalation of graphene layers in graphite and stirred for few minutes to obtain a uniform mix. The reaction mixture was shifted to an ice bath to evade excess temperature generated during the addition of oxidizers. To this mixture, 1.5 g of sodium nitrate (NaNO3) was added and stirred for 30 min. Till this stage, all the steps are carried out under room conditions. The idea behind oxidation is to increase the inter-planar spacing between two basal plans in graphite. Subsequently, 9 g of potassium permanganate (KMnO4) was added gradually and reaction temperature during this addition was maintained at 0 °C with the aid of an ice bath as this oxidation process is highly exothermic. The reactions carried out in an ice bath until the dark greenish color appeared. Then the reaction mixture was removed from the ice bath and was allowed to cool under stirring. After some time, the reaction mixture becomes thickening with decreasing effervescence. At the end of 5 h, the mixture became a brownish grey thick paste. Consequently, distilled water (138 mL) was added drop by drop to the mixture causing violent effervescence and internal temperature of the resultant solution rises up to the 98 °C. The reaction mixture was maintained at this temperature for 15 min. After cooling the mixture to room temperature it was further diluted warm distilled water of 420 mL and a small amount of 30% H2O2 of 3 mL was added to remove the residual permanganate and manganese dioxide to colorless soluble manganese sulfate when treating with peroxide, the suspension turned bright yellow. The obtained final suspension was washed for several times until the pH becomes neutral. After that the paste was washed with DI water followed by ethanol using Remi centrifuge at 3000 rpm speed to discard unreacted products and dried for overnight in vacuum oven at 80 °C. The filtrate was collected and kept in a hot oven at 100 °C for 12 h to obtain GO powder.

3.1.2 Reduced Graphene Oxide

GO obtained as above was subjected to microwave irradiation (MWI) (900 W and 2.45 GHz) inside a household microwave oven for few seconds to get exfoliation of graphene sheets and removal of attached functional groups which are mostly epoxide and hydroxyl groups during

the MWI. As resulted graphene worms, which is further ultra-probe sonicated in ethanol for 1 h to obtain a uniform suspension of graphene sheets (reduced graphene oxide).

3.1.3 Fe₃O₄/FLG Composite

In this present study, Fe₂O₃ was obtained by heating FeC₂O₄.2H₂O slowly 3 °C/min at 600 °C temperature in presence of air. Here the GO was prepared with different degree of oxidation by varying oxidizing agents KMnO₄. To obtain GO1 with low DO, 1 g of graphite flakes was dispersed in 25 mL of H₂SO₄ at a temperature less than 5 °C. In next step, 0.5 g of NaNO₃ and 3 g of KMnO₄ were mixed very slowly one after the other. After stirring for some time 30 minutes at room temperature 25 mL of DI water was added to the above reaction mixture. As a result, the internal temperature of the reaction mixture (RM1) was raised up to approximately 98 °C and it was stirred for 1h at the same temperature. Afterwards, the reaction mixture was allowed to cool to room temperature. Finally, 1 mL of H₂O₂ (35 wt. %) was added to the reaction mixture resulting sedimentation. The final suspension was subjected to multiple washes with DI water until the supernant's pH became ~7. The resultant material indicated with a code as GO1. In other experiment to get GO with higher DO (GO2), the above mentioned process was repeated except for using 98% H₂SO₄ and 50 mL of DI water. Both GO1 and GO2 were dried for 12 h in hot air oven at 80 °C. Then, two reaction mixtures (RM), GO1 and Fe₂O3 (RM1), and GO2 and Fe₂O₃ (RM2) were prepared by mechanical mixing for 30 min.

Another sample of Fe₃O₄/FLG composite was synthesized in the following manner: 2 mole of GO was taken for 1 mole of Fe₂O₃. Molecular formula C₂HO was used for GOs for molar calculations. Then both reaction powders, 6 g each, were taken into separate ceramic boats and heated separately in a tubular furnace (Carbolite, UK). Heating of both reaction powders was carried out in Ar environment at heating and cooling rates of 5 °C min⁻¹. Thermal treatment of reaction powders was carried out in the temperature range 650–750 °C and time range 2–8 h. As a result of heating, black colored fine powders of Fe₃O₄/FLG composites of ~3 g each were obtained.

3.1.4 Fe₂Mo₃O₈/FLG Composite

The as-synthesized GO was dried in the vacuum oven at 65 °C for 12 h and was used in the composite synthesis. A dry powder mixture of 3.5 moles of GO, FeC₂O₄·2H₂O, and MoO₃ is heated at 750 °C for 8 h under Ar atmosphere in a tubular furnace and the resultant black colored material is Fe₂Mo₃O₈/FLG composite. The obtained composite was tested for anode

material in Li ion battery applications.

3.1.5 MnO/FLG Composite

Firstly, 6 g of dried powders of GO and MnO₂ was mechanically mixed for 1 h. The mixture was transferred into a ceramic boat. After it was moved into a tubular furnace heating system and then it was flushed with Ar gas to remove air before preceding the experiment. The temperature was maintained at 650 °C for 8 h at a rate of 5 °C min⁻¹ under Ar atmosphere. After that, the furnace was cooled down to room temperature at a rate of 5 °C min⁻¹. Finally, 3 g of fine MnO/FLG powder was obtained, which was characterized to study the crystalline structure, morphological features, elemental composition, etc., and tested for its supercapacitor application.

3.2 Materials Characterization

3.2.1 Electron Microscopy

The powder samples of graphene and metal oxide nanocomposite were carried out by using FEGSEM, Model Zeiss Ultra 55 imaging was done at an accelerating voltage of 5 kV and elemental mapping were carried out using Model FEI NOVA NanoSem 450. The assynthesized graphene nanocomposite having conductive nature due to that it was not sputter coated with any gold or carbon while only graphene oxide was coated because it was having insulating nature. In the same way, to find out the elemental composition of FLG/metal oxide nanocomposite using Energy dispersive analysis of X-rays (EDAX) and elemental mapping techniques was employed. The morphological analysis of metal oxide/FLG composites was examined also by using high resolution transmission electron microscopy technique (Model No: FEI Technai G² S-Twin) operated at an accelerating voltage of 200 KV. All the powder samples were sonicated in ethanol solution and few drops of solution cast on carbon-coated Cu grids 200 mesh. It was dried for half an hour at 90 °C on hot woven. After the drying process, it was used to examining at a different location of the sample. The low and high-resolution TEM was employed for all samples to get lattice fringes and selected area electron diffraction (SAED) pattern. Gatan Digital Micrograph software used to convert DM3 files into images and FFT, IFFT patterns, profiles were done using this software.

3.2.2 X-ray Diffraction

The structural information of FLG/metal oxide nanocomposite was studied by using X-ray diffraction technique to obtain phase identification. The XRD pattern for the obtained powder

samples were recorded 2θ in the range from 5 to 90° . Brucker D8 Advanced instrument was used with using Cu K α radiation as the X-ray source (λ =1.54 Å). To find indexing of reflection XRD peaks Crystallographica search-match software was used to find the phase identification, crystal structure, d-spacing. TOPAS software was also utilized for Rietveld refinement.

3.2.3 Raman Scattering

A micro-Raman scattering was carried out using a Witech Raman 2000 system. Raman studies were carried out on as-synthesized samples to understand the bonding structure of the samples. The powder sample was placed thin glass slides and a laser wavelength of 532 nm was irradiated to get the Raman spectrum. It was operated at room temperature condition and Raman spectra recorded wave number in the 100 to 4500 cm⁻¹.

3.2.4 X-ray Photoelectron Spectroscopy

X-ray photoelectron spectroscopy (XPS) was used to analyze different oxidation states of individual elements and their possible bonding with other species present in the nanocomposites. It is a quantitative surface sensitive technique it gives the elements present in the sample but also gives the element which is bonded to it. The binding energy (B.E) values are evaluated from the obtained survey spectra with the Model No: AXIS ultra DLD spectrometer, Krotos analytica with a monochromatic AlKα radiation source. The obtained survey spectrum was analyzed using Casa XPS software. Survey spectrum recorded in the range from 0 to 1200 eV. Further, the bonding possibilities were understood from the deconvolution of individual high-resolution spectra by using peak fit (version 4.05) software.

3.2.5 Thermogravimetric Analysis

Thermogravimetric analysis (TGA) is a thermal analysis technique in which mass of powder sample measured correspondingly with respect to time as well as change of temperature. The as synthesized of FLG/Fe₃O₄, Fe₂Mo₃O₈/FLG powder samples were carried to find out individual weight percentages of graphene and metal oxide weight percentages using the Model No: TA Instruments 2960 (DTA-TGA) in air atmosphere temperature in the range of 25-1000 °C at a heating rate of 10 °C min⁻¹.

3.2.6 BET Surface Area Measurement

To know the surface area and porosity of the powder samples analyzed Nitrogen (N₂) physisorption experiments at 77 K on Micromeritics (Model Tri-Star 3000, USA) using Brunauer-Emmett-Teller (BET) method.

3.3 Li-ion Cell Testing

Electrodes are made by mixing highly crystalline few layered graphene (hcFLG) and Fe₂Mo₃O₈/FLG, polyvinylidene fluoride (PVDF) binder and Super-Li carbon in 55:30:15 wt.%. The electrodes are 16 mm diameter circular discs with a geometrical area of around 2 cm² and mass of the active material was in the range of 2-4 mg (total electrode mass with 55 wt. % by not including/excluding the weight of Cu foil). CR2016 type coin cells with Fe₂Mo₃O₈/EG as anode and Li metal (18 mm circular disc) as cathode are made inside the glove box filled with an argon atmosphere. 1 M LiPF₆ in ethylene carbonate and diethyl carbonate (EC and DEC with 1:1 volume) while Whatman glass micro-fiber filter was used as the electrolyte and separators. All the battery testing experiments were carried out in the voltage range 0.005–3.0 V but after 8 h of relaxation of the coin cells at the room temperature. Cyclic voltammetry (CV) experiments were performed using SOLARTRON 1470E equipment at a scan rate of 0.1 mV/s. The galvanostatic charge-discharge testing was carried out using NEWARE battery system at current rates starting from 50 to 3000 mA g⁻¹.

3.4 Supercapacitor Testing

The electrode material was prepared using MnO/FLG, PVDF binder, carbon black (weight percentage ratios of 80:10:10). First, to obtain a uniform mixture these materials were finely grounded using mortar and pestle for a 1h. After that, NMPs were added to the grounded fine powder to make slurry. The working electrode was made by slurry coated on a Ni substrate (1 cm x 0.5 cm) and allowed to immediately dry under a sunlamp for a few minutes. After being moved into the oven and the fabricated electrode annealed at 80 °C for 8 h before the electrochemical test. To study the electrochemical behavior of the MnO/FLG coated suspension obtained on a Ni substrate at the room temperature using a conventional threeelectrode configuration (aqueous region). The collected material was weighed before and after noting that 0.4 mg of the suspension was coated. The as-fabricated MnO/FLG@Ni used as working electrode, Ag/AgCl as a reference electrode and Pt as the counter electrode in the presence of 1M Li₂SO₄ solution. In the working electrode, only the square rectangle part is allowed for intercalation because it has been covered with white tape. The electrochemical property measurements of MnO/FLG using cyclic voltammetry (CV), galvanostatic chargedischarge and electrochemical impedance spectroscopy (ESI) was carried out using the three electrode method in the 1M LiSO₄ (aqueous region). The electrochemical configuration of three electrode cells were connected to a computer controlled potentiostat.

3.5 Fe₃O₄/FLG-Glassy Carbon Electrode

To fabricate modified FLG/Fe₃O₄-GCE, first the glassy carbon electrode with 3 mm diameter was prepared by polishing with 0.05, 0.3, 1.0 µm alumina slurry on micro cloth pads to get a mirror like finish and rinsed with double distilled water. It was ultra-sonicated carefully with HNO₃, ethanol and washed with double distilled water. 5 µL of Fe₃O₄/FLG is dropped on the GCE and allow drying it for 6 min. A standard three-electrode cell system was employed to carry out electrochemical sensing properties for the detection of dopamine, where the Ag/AgCl (saturated) as the reference and platinum (Pt) wire served as a counter electrode, respectively. The Dopamine Hydrochloride solution was prepared by adding a few drops of perchloric acid and the uric acid solution was prepared by dissolving in 0.1 sodium hydroxides and AA in Millipore water. Phosphate buffer solution (PBS) developed with 0.1M NaH₂PO₄ and 0.1M Na₂HPO₄.

Chapter 4 Results and Discussion

4.1 Anode Materials in Li Ion Batteries

4.1.1 Highly Crystalline Few Layered Graphene

The morphology of GFs, GO, GWs and hcFLG as seen using FESEM is shown in Fig. 4.1. GFs are thick, implying that each GF is constituted by a stack of numerous graphene layers. GO is crumpled due to attachment of functional groups during the oxidation process of GF. After MWI, GO transforms to worm-like structures named here as GWs, which are swollen along the c-axis of graphite implying that the graphene sheets are loosely bonded along the c-axis. Ultra-sonication of GWs resulted in the formation of thin sheets of hcFLG (each hcFLG particle has 5-20 layers of graphene). The semitransparent nature of hcFLG as seen in Fig. 4.1 (d-f) signifies that hcFLG is thicker than the previously reported FLG [1].

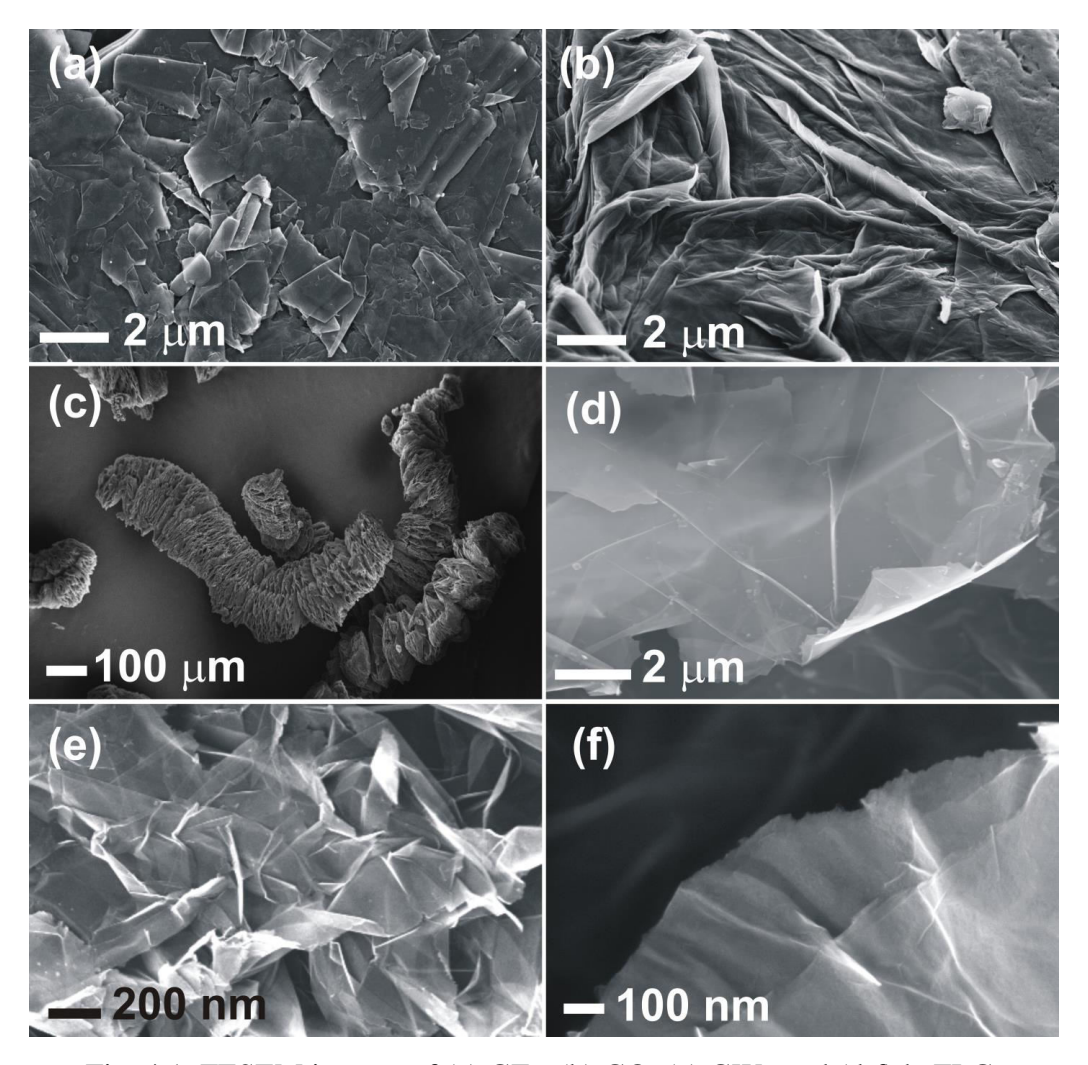


Fig. 4.1. FESEM images of (a) GFs, (b) GO, (c) GWs and (d-f) hcFLG.

TEM observations on hcFLG (w.r.t morphology) shown in Fig. 4.2 comply with FESEM observations. The HRTEM image shown in Fig. 4.2(e) of a folded region of hcFLG confirms its few-layered nature while the electron diffraction pattern shown in Fig. 4.2(f) confirms the hexagonal crystal structure and few/multiple layered nature of hcFLG. Moreover, the high order electron diffraction spots displaying almost similar intensities as those of lower order diffraction spots indicates highly crystalline nature of FLG unlike in the previous case of FLG [1]. Further, the XRD pattern of hcFLG in comparison to that of graphite and GO is shown in Fig. 4.3. XRD pattern of pristine graphite depicts a high intensity sharp peak at $(2\theta =) 26.6^{\circ}$ corresponding to (002) basal plane with an interlayer spacing of 0.335 nm in highly crystalline graphite. In the case of GO, (002) peak has shifted to 11.8° indicating oxidation of graphite (interlayer spacing of 0.749 nm). In the case of hcFLG, (002) peak has shifted to 23.4° indicating reduction of GO to hcFLG (interlayer spacing of 0.34 nm) while maintaining excellent crystallinity.

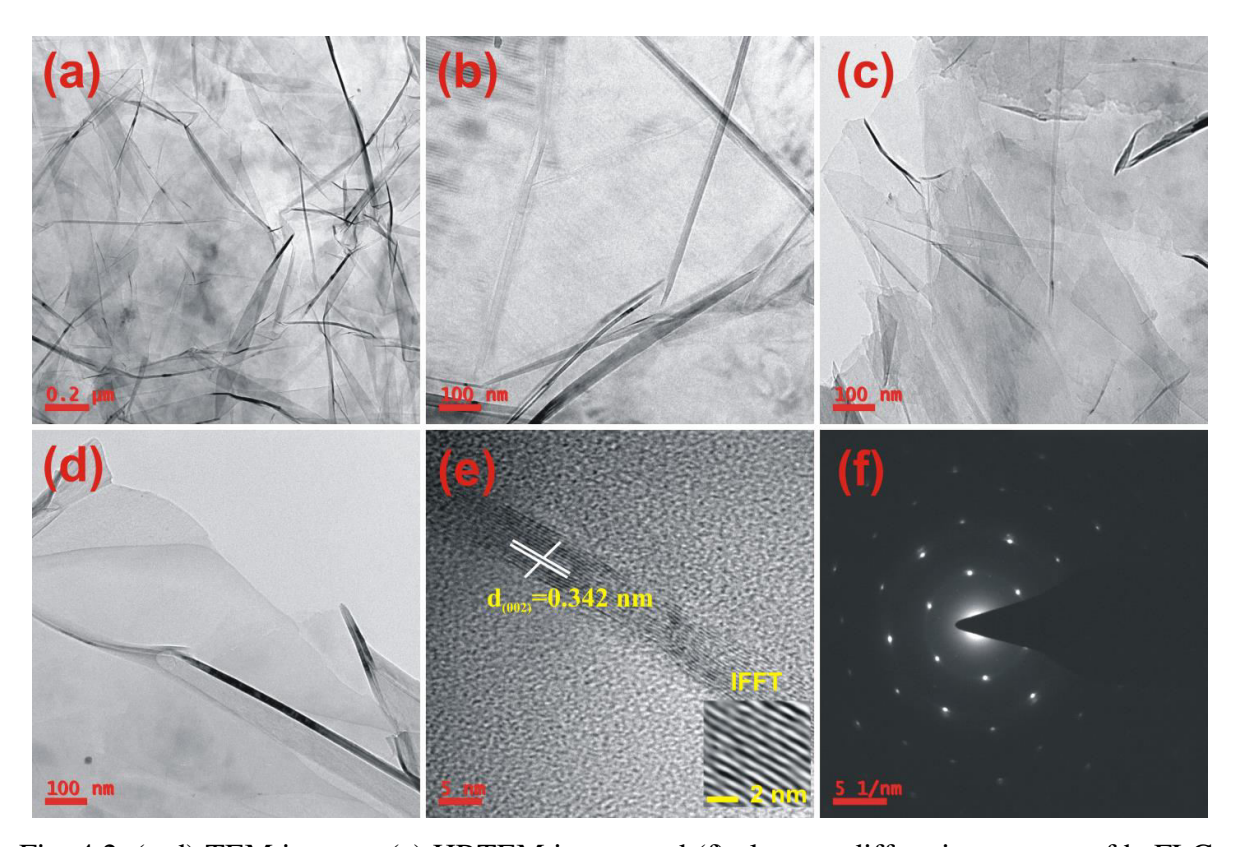


Fig. 4.2. (a-d) TEM images, (e) HRTEM image and (f) electron diffraction pattern of hcFLG. Inverse Fast Fourier Transform (IFFT) image (inset in (e)) showing multiple graphene layers.

The bonding structure of hcFLG in comparison to that of GFs and GO was examined using Raman spectra shown in Fig. 4.4. In Raman spectra of graphite or graphene based materials three characteristic bands namely G band assigned to the first order scattering of the E_{2g} phonon

from sp² carbon (graphite lattice), and the D, and 2D bands resulting from the first and second order phonon scattering, respectively from the structural imperfections created by the functional groups on the carbon basal plane [1] are typically observed. In this study, G, D and 2D bands in the case of GFs are found at 1349.89, 1582.94, and 2714.38 cm⁻¹, respectively. On the other hand, G, D and 2D bands in the case of GO are found at 1352.36, 1581.38, and 2678.46 cm⁻¹, respectively, confirming disorder due to oxidation process. In the case of hcFLG, G, D and 2D bands are found at 1348.57, 1581.74, and 2710.24 cm⁻¹, respectively, confirming the reduced and stacked nature of hcFLG. The intensity ratio of D band to G band (I_D/I_G) in the case of GFs, GO and hcFLG is found to be ~0.16, ~0.95, and ~0.63, respectively complying with the structural observations made using XRD study [1,2]. The intensity ratio of D band to 2D band (I_G/I_{2D}) is ~1.41 in the case of hcFLG indicating its few-layered nature [1,2].

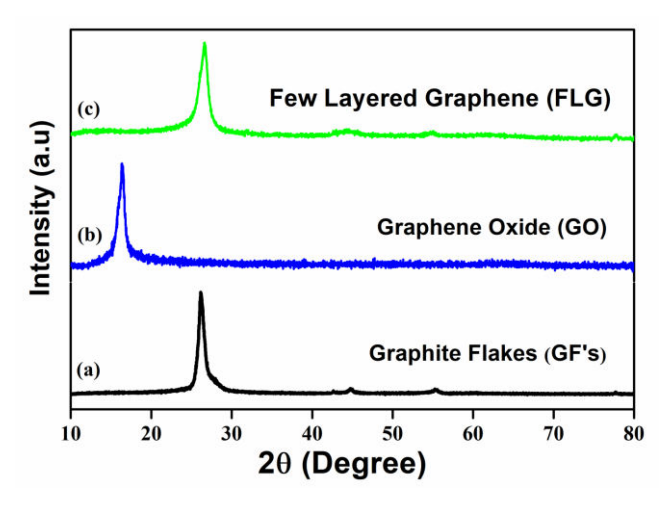


Fig. 4.3. XRD patterns of (a) GFs, (b) GO and (c) hcFLG.

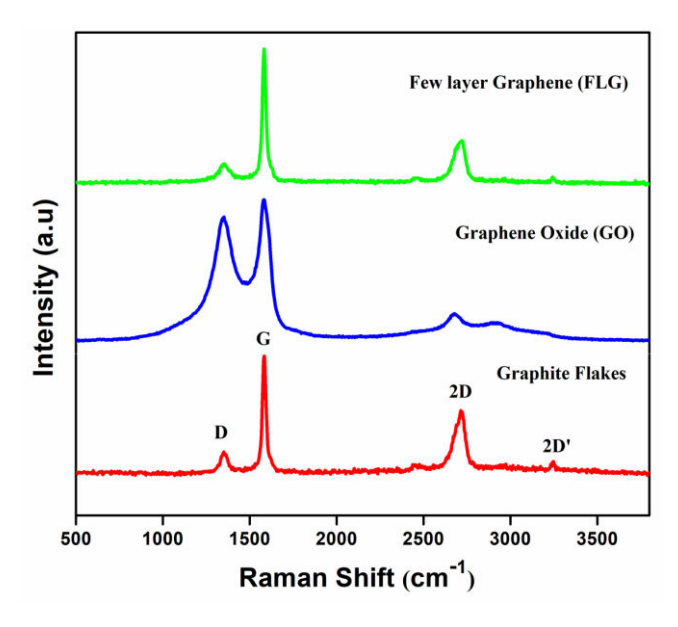


Fig. 4.4. Raman spectra of GFs, GO, and hcFLG.

Lithiation characteristics of hcFLG and CG are understood using CV data (Fig. 4.5(a-f)) obtained at a scan rate of 0.1 mV s⁻¹ in the voltage window of 0.005–3.0 V. During the first cathodic scan of hcFLG, four reduction peaks are noticed at ~1.44, ~0.66, ~0.18 and ~0.035 V, which are typical in the case of graphenaceous materials (Fig. 4.5(a-b)) [1,3]. Out of these four peaks, the first two, i.e., the peaks at ~1.44 and ~0.66 V did not appear from the second cycle onwards (Fig. 4.5(a)). These two peaks appear because of electrolyte decomposition on hcFLG that results in irreversible covalent compounds that contribute to solid electrolyte interphase (SEI) formation [1,3]. The latter two, i.e., the peaks at ~0.18 and ~0.035 V are observed throughout the cycling (Fig. 4.5(a-b)); these correspond to lithium intercalation into hcFLG [1,3,4]. In the anodic scan, three constant oxidation peaks at ~0.12, ~0.16 and ~0.24 V are observed as shown in Fig. 4.5(a-b). These peaks have evolved because of lithium deintercalation from hcFLG [1,3,4]. On the other hand, CG showed a small SEI peak at ~0.67 V and inseparable intercalation (reduction) peaks in the range 0.2–0.005 V whilst there is only one broad oxidation peak in the range 0.005–0.35 V (Fig. 4.5(c-d)).

The clear and distinct peaks observed in the case of hcFLG but not observed in the case of commercial graphite (CG) are signatures of various Li-stages as shown in Fig. 4.6 [4]. CG is also capable of visualizing such Li-stages but it needs to be very thin [4]. This inference signifies that hcFLG is built-in with far less number of graphene (basal planes) layers than CG as indicated by the microstructural analysis. The difference between first and second reduction curves is very high in the case of hcFLG (Fig. 4.5(a)) and in comparison to that of CG (Fig. 4.5(c)) implying that in CG there is lager SEI formation and that it has higher extent of disorder, which is in good agreement with Raman scattering results. The non-zero redox current in between 0.3 V and 3.0 V is due to electrochemical adsorption/desorption of Li onto hcFLG surfaces (Fig. 4.5(a)). This current is almost zero in the case of CG (Fig. 4.5(c)); this once again exposes the highly disordered nature of CG.

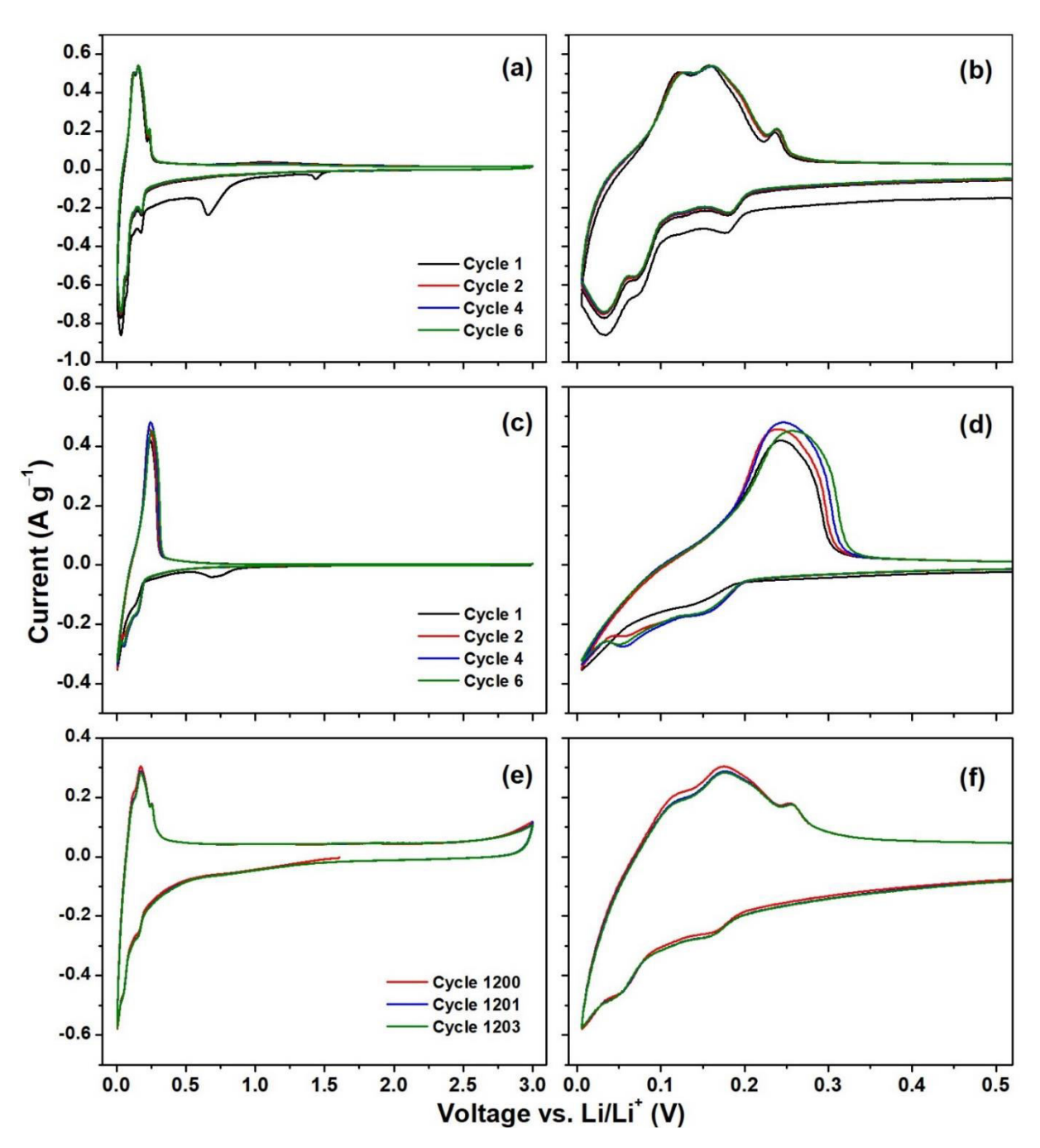


Fig. 4.5. CV profiles of hcFLG (a, b, e, f) and CG (c, d) at a scan rate of 0.1 mV/s.

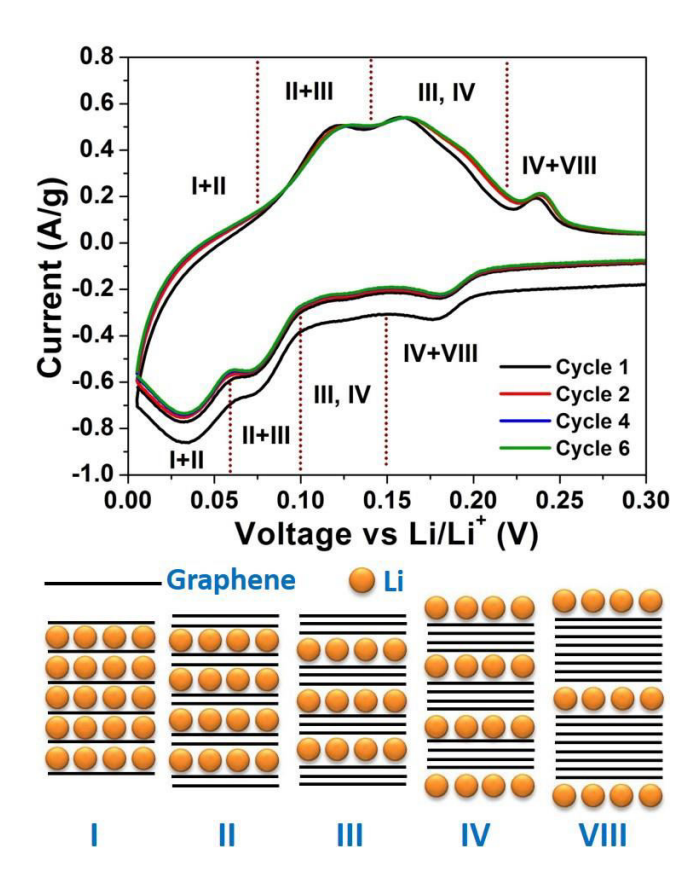


Fig. 4.6. Li stages in hcFLG; Roman number defines stage [4].

The voltage-capacity (charge-discharge) profiles of hcFLG and the CG at a current density of 0.1 C at a Voltage in between 0.005 V and 3.0 V are shown in Fig. 4.7. The changes in the slopes of charge-discharge curves of both cases are consistent with the CV results as well as the previously reported work [1]. The hcFLG's first discharge and charge capacities are found to be 779 and 398 mAh g⁻¹, respectively whereas respective capacities of CG are found to be 410 and 342 mAh g⁻¹. The larger ICL (the main difference between first discharge and charge capacities due to the formation of SEI) of ~381 mAh g⁻¹ was observed in the case of hcFLG in comparison to that of CG (~68 mAh g⁻¹). The CV profiles of hcFLG mainly differed from CG by showing quasi-continuous sloping plateaus as shown in Fig. 4.7(a) and (c). Almost all the charge-discharge capacities of CG lie in-between 0.3 V and 0.005 V (Fig. 4.7(b)) and strictly related to Li-ion intercalation/de-intercalation (diffusion) into Vander Waal gaps of perfectly ordered graphene layers (basal planes). These capacities of CG mainly originate from absorption/desorption of one lithium to one hexagon of carbons i.e., in-plane LiC6 configuration [1]. Thus, diffusion of Li-ion (primary lithiation mechanism) is the only source of CG capacities.

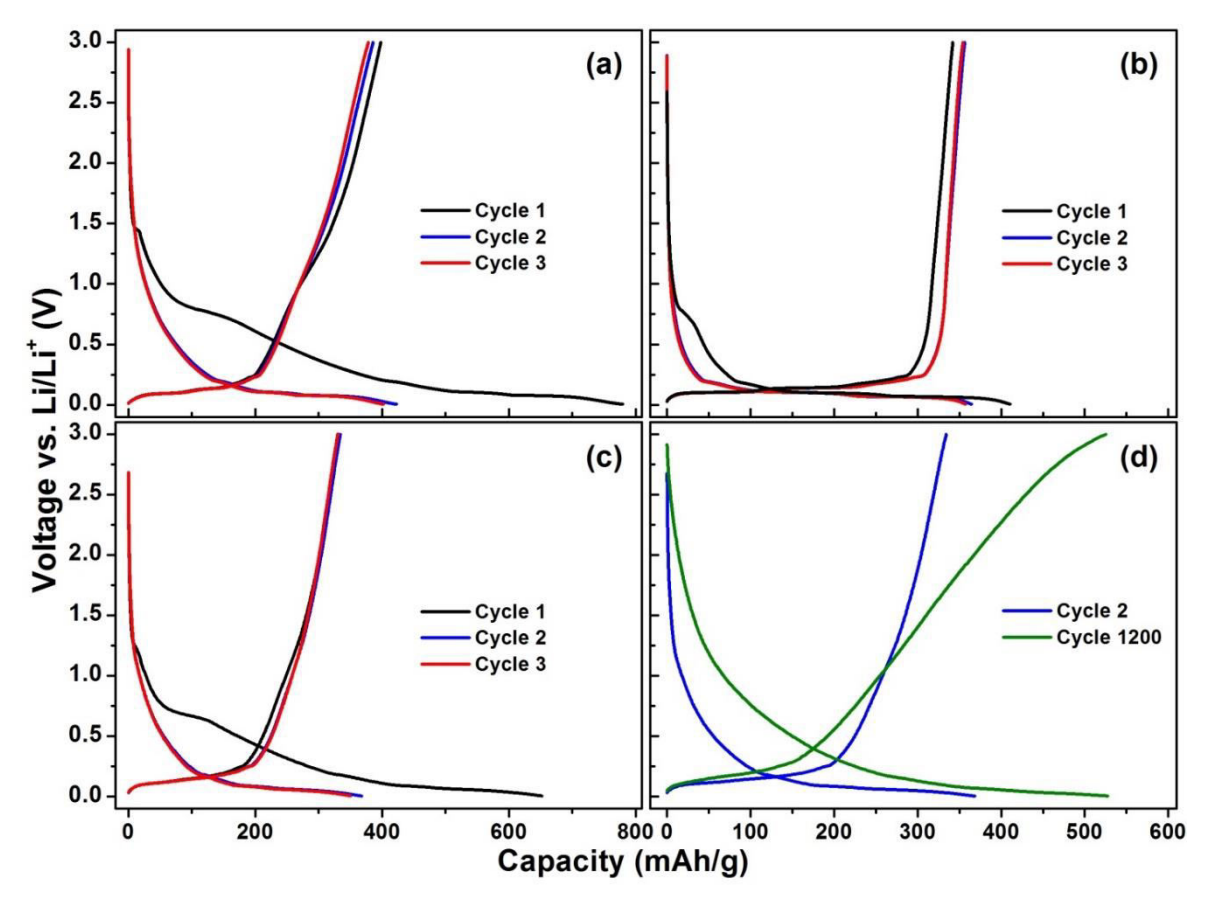


Fig. 4.7. Charge-discharge characteristics of hcFLG at 0.1C (a), 1.0 C (c) and (d), in comparison with CG at 0.1 C (b).

hcFLG shows continuous sloping plateaus above 0.3 V that is due to a combination of Li-ions surface absorption and quasi-diffusion processes (secondary lithiation mechanism). Below 0.3 V, the profile features are found similar to that of CG and obviously, capacities are from primary lithiation mechanism. At the end of second discharge, hcFLG delivered a capacity of ~423 mAh g⁻¹ out of which ~26% (110 mAh g⁻¹) is due to secondary lithiation mechanism and a similar trend is noticed while charging (Fig. 4.7(a). At 1.0 C current rate hcFLG exhibited a voltage-capacity profile similar to 0.1 C rate (Fig. 4.7(c)) and its cyclability is as shown in Fig. 4.8(a). During the first cycle, discharge and charge capacities are found to be 651 and 329 mAh g⁻¹, respectively and account for Coulombic efficiency (QE) of ~51%. QE enhanced to more than 90% in the second cycle and kept on increasing to >98 and >99 at 10th and 20th cycles onward, respectively. From 20th cycle onward hcFLG delivered very stable capacities of ~310 mAh g⁻¹ with QE >99% over 100 cycles. It retained 94% initial charge capacity at the end of the 100th cycle. Further, it exhibited excellent rate capability with a current rate ranging from 0.1 to 10.0 C as shown in Fig. 4.8(b). Even at 10.0 C, it delivered a charge capacity of ~215 mAh g⁻¹ with QE >99%. A slight increase in capacity is noticed when current rate switched

from 10.0 C to 1.0, 0.5 and 0.1 C. The observed increase in capacity took place more profoundly during long-term cycling about 1200 cycles at 1.0 and 2.0 C as shown in Fig. 4.8(c). Such an increase of capacity is owing to further in-situ electrochemical exfoliation of graphene sheets that creates more room for additional lithium [2]. Due to this, in-situ exfoliation backed extra lithiation, capacity boosted up from 330 to 555 mAh g⁻¹ at 1175th cycle at 1.0 C. This increase in capacity is equivalent to ~0.6 moles of additional lithium. Even at 2.0 C, initial charge capacity of about 200 mAh g⁻¹ shot up to 365 mAh g⁻¹ at 1160th cycle corresponding to 0.44 moles of extra lithium. Even at the 1200th cycle of 1.0 C rate, the charge-discharge profile is found similar to 2nd cycle but capacity features slightly shifted to higher Voltages as shown in Fig. 4.7(d). The total second discharge capacity constituted by capacity above and below 0.3 V is found to be 86 (~23%) to 282 (~77%) mAh g⁻¹, respectively. Respective capacity values at 1200th discharge are found to be 203 (~38%) to 325 (~62%) mAh g⁻¹. Thus, capacity above 0.3 V is increased by 2.36 times whilst capacity below 0.3 V slightly increased by 1.15 times only. Therefore, the increase in capacity is mainly due to increased secondary lithiation mechanism whilst capacity from primary lithiation mechanism is almost intact.

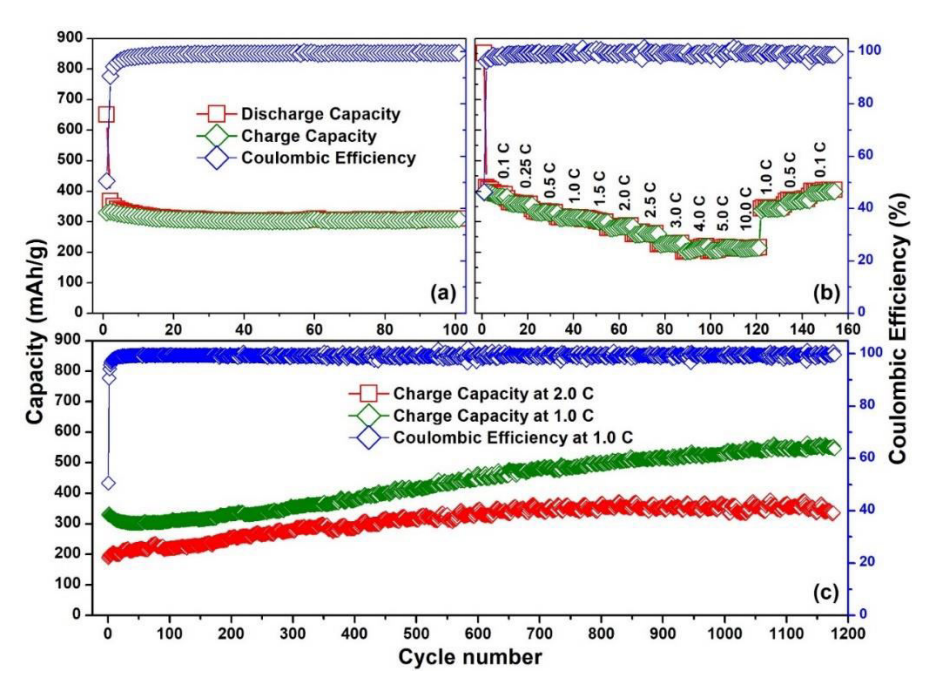


Fig. 4.8. Capacity versus cycle number profiles of hcFLG (a) at 1.0 C (b) rate capability test and (c) long-term cycling at 1.0 and 2.0 C.

The lithiation performance of hcFLG is far superior to that of CG as well as other reported similar materials as mentioned in Table 4.1. hcFLG clearly outperformed microcrystalline graphite (MCG), graphite modified (MG) with MWI, KCl, LiAlO₂, and FLGs prepared by

MWI, jet cavitation (JC) *etc*. The lithiation performance of hcFLG outdid the graphite that was pre-treated with Li₂SO₄, and needed special electrode preparation and sulfolane (SL) based electrolyte. It also outperformed the CG and natural graphite (NG) that are coated with TiO_{2-x}, Al₂O₃ (cycled at 50 °C), AlPO₄ and AlF₃. Similar to hcFLG, increasing capacity trends after few initial cycles of formation has been observed in the cases of JC-FLG, MWI-MG, and MWI-FLG. It seems pure FLGs and MGs commonly exhibit capacity increase over the course of cycling. However, hcFLG is a worthy selection for the real-time application in view of its simplicity and time-saving synthesis, superior capacities and long-lasting cyclability with increasing capacities, especially at higher current rates.

Table 4.1. Performance comparison of hcFLG with various modified graphite and FLGs.

Name	DCa	CC_p	DC	CC	Current
	1 st Cycle	1 st Cycle	nth Cycle	n th Cycle	Rate
hcFLG [this thesis]	651	330	548	547	1.0 C
			@ 1200 th	@ 1200 th	
JC-FLG [5]	410	369	374 @ 40 th	371 @ 40 th	0.1 C
MCG [6]	423		387 @ 30 th		0.2 C
MWI-MG [7]	710	325	371 @ 400 th	370 @ 400 th	0.27 C
Li ₂ SO ₄ -Graphite [8]	317	314		254 @ 60 th	0.2 C
SL-Graphite [9]	370	340		330 @ 60 th	0.5 C
LiAlO ₂ -Graphite [10]	298		320 @ 100 th		0.5 C
KCl-Graphite [11]	525		270 @ 200 th		1.0 C
TiO _{2-x} -Graphite [12]		360		350 @ 100 th	1.0 C
		@ 100 th			
MWI-FLG [1]	455	281	262 @ 60 th	261 @ 60 th	1.0 C
AlF ₃ -CG [13]	400	337		320 @ 300 th	0.5 C
	@0.05 C	@0.05 C			
Al ₂ O ₃ -coated NG [14]		360		350	0.1 C
AlPO ₄ -coated NG [15]	386	368		291	1.0 C

 $^{{}^{}a}DC$ – discharge capacity, ${}^{b}CC$ – charge capacity (mAh/g), some capacity values assumed from images if not clearly specified.

Post-cycling CV features after long-term cycling at 1.0 C rate as shown in Fig. 4.5 (e) and (f) is in accordance with GC profile shown in Fig. 4.7(d). The area under the curves in-between 0.3-3.0 V increased in a greater proportion compared to the first few cycles (Fig. 4.5(a)). Even after the 1200^{th} cycle, the Li-staging phenomenon is clearly visible as shown in Fig. 4.5(f) with individual staging boundaries slightly overlapped with each other when compared with that shown in Fig. 4.5(b). This is attributed to the increased interplanar distance between individual graphene layers due to in-situ exfoliation [3]. It is clear from both GC and CV that above 0.3 V secondary lithiation mechanism is mainly contributing to the capacity increase.

Post-cycling structural study of hcFLG was carried out to probe in-situ electrochemical exfoliation. XRD patterns pertaining to hcFLG electrodes in fresh, 100th charge and 1200th charge conditions are shown in Fig. 4.9. The typical graphitic (002) peak of fresh and 100th charge electrode is found at 26.5° corresponding to the interplanar distance (d) of 0.336 nm. The intensity count of (002) peak of 100th charge is enhanced plausibly more in in-plane orientation of hcFLG sheets due to electrode formation effect. But no change in the peak position signifies that early stage cycling has not much effect on the structural changes of hcFLG. For this reason, very stable capacity values are noticed as shown in Fig. 4.8(a). After the 1200th charge, the graphitic peak is slightly shifted to a lower 20 of 26.3° that is equivalent to a small increase in d ~ 0.339 nm. The small increase in d value suggests perfect graphene layers and negligible exfoliation. For this reason, the Li-staging phenomenon is clearly visible as seen in Fig. 4.5(f). Further, a broad hump is noticed in-between $10-25^{\circ}$ that is characteristic of in-situ exfoliation of graphene layers associated with disorders [3]. Therefore hcFLG is a mixture of perfect and disordered graphene layers. Thus, XRD analysis confirms that the increase in capacity is by secondary lithiation mechanism, which is due to in-situ exfoliation of disordered graphene layers. Capacity increase by primary lithiation mechanism is held stable due to the intact structural integrity of perfect graphene layers.

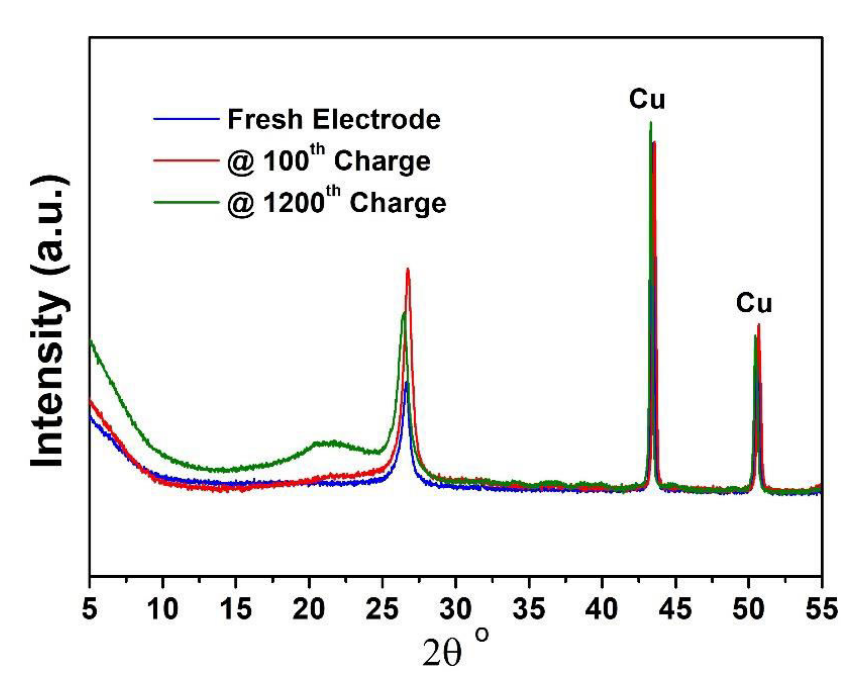


Fig. 4.9. XRD patterns of hcFLG electrodes afresh, after 100 and after 1200 cycles.

4.1.2 Fe₃O₄/FLG Composite

TEM images of two different graphene oxides (GO1-left and GO2-right) are shown in Fig. 4.10. The respective insets in Fig. 4.10 show the selected area electron diffraction (SAED) patterns of the two graphene oxides. GO1 was identified as a GO with lower degree of oxidation (i.e., C/O ratio) as compared with GO2. FESEM and TEM images of Fe₃O₄/FLG obtained from GO1 and GO2 are shown in Figs. 4.11 and 4.12, respectively. Both FESEM and TEM images show that Fe₃O₄ particles are spread across FLG surfaces and formed a network around edges of FLG. It is also clear from FESEM and TEM images that the Fe₃O₄ particles adhered well to graphene sheets. From the XRD pattern (Fig. 4.13) it was calculated that Fe₃O₄ possess an average crystallite size of 57.6 nm with lattice parameter a = 8.4086 Å when refined w.r.t space group Fd-3m (PDF#75-449).

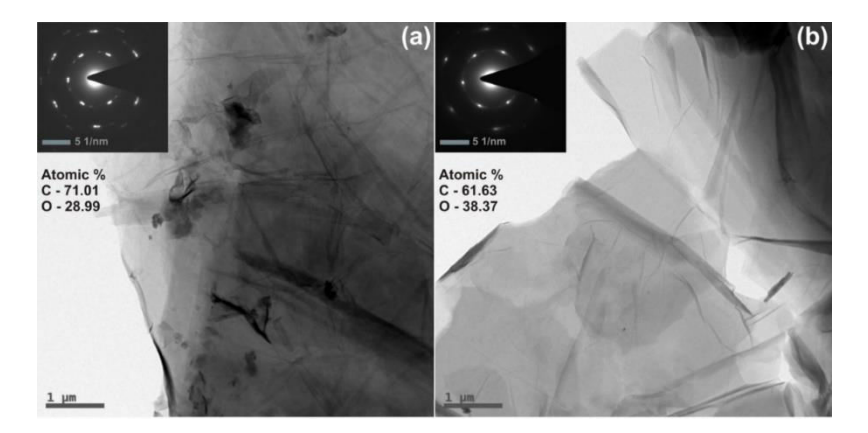


Fig. 4.10. TEM images of GO1 and GO2. Insets show the respective SAED patterns.

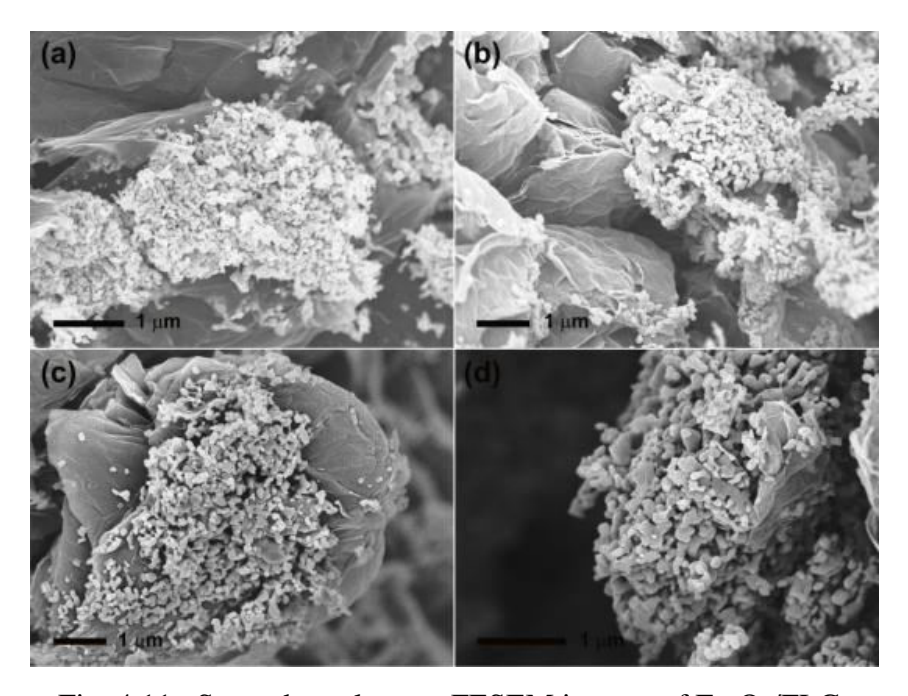


Fig. 4.11. Secondary electron FESEM images of Fe₃O₄/FLG.

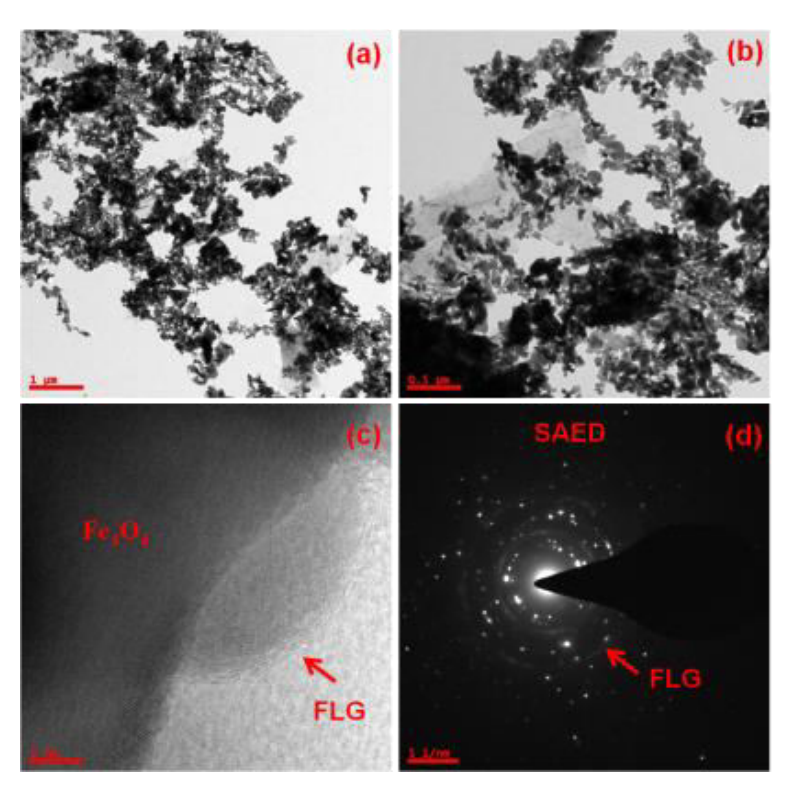


Fig. 4.12. TEM images (a-c) of Fe₃O₄/FLG at diffrent magnifications. (c) HRTEM image and (d) SAED pattern of Fe₃O₄/FLG.

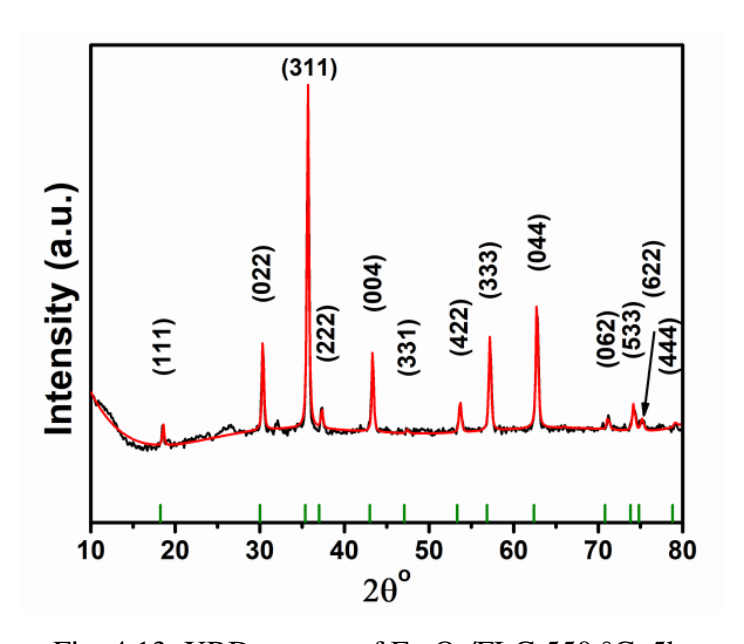


Fig. 4.13. XRD pattern of Fe₃O₄/FLG 550 °C–5h.

Electrochemical characterization results of Fe₃O₄/FLG–550 °C–5h as an anode material in LIB in a typical half-cell configuration are shown in Fig. 14. The observed CV (Fig. 14(a)) and charge-discharge (Fig. 14(b)) characteristics are consistent with each other. For example large reduction current and redox couple noticed in CV are in accordance with large discharge

capacity and charge-discharging potentials of galvanostatic cycling, respectively. The large reduction current in first cathodic scan of CV and large first discharge capacity are a combined consequence of electrolyte decomposition as well as electrochemical reaction between Li and Fe₃O₄ to form elemental Fe and Li₂O compounds [16-18]. These characteristic reactions are partially reversible and that is why they do not appear from first anodic scan and first charging onwards. The broad current peaks centered on 0.9 and 0.18 V correspond to multiple redox reactions between Li/Fe₃O₄ and Li₂O/Fe, respectively [16-18]. In both testing modes the entire non-zero current and capacity at all voltages other than redox reactions of iron oxide originates from (de)lithiation by FLG [1,19]. These overall electrochemical features are commensurate with other Fe₃O₄/FLG composites reported elsewhere [16-18].

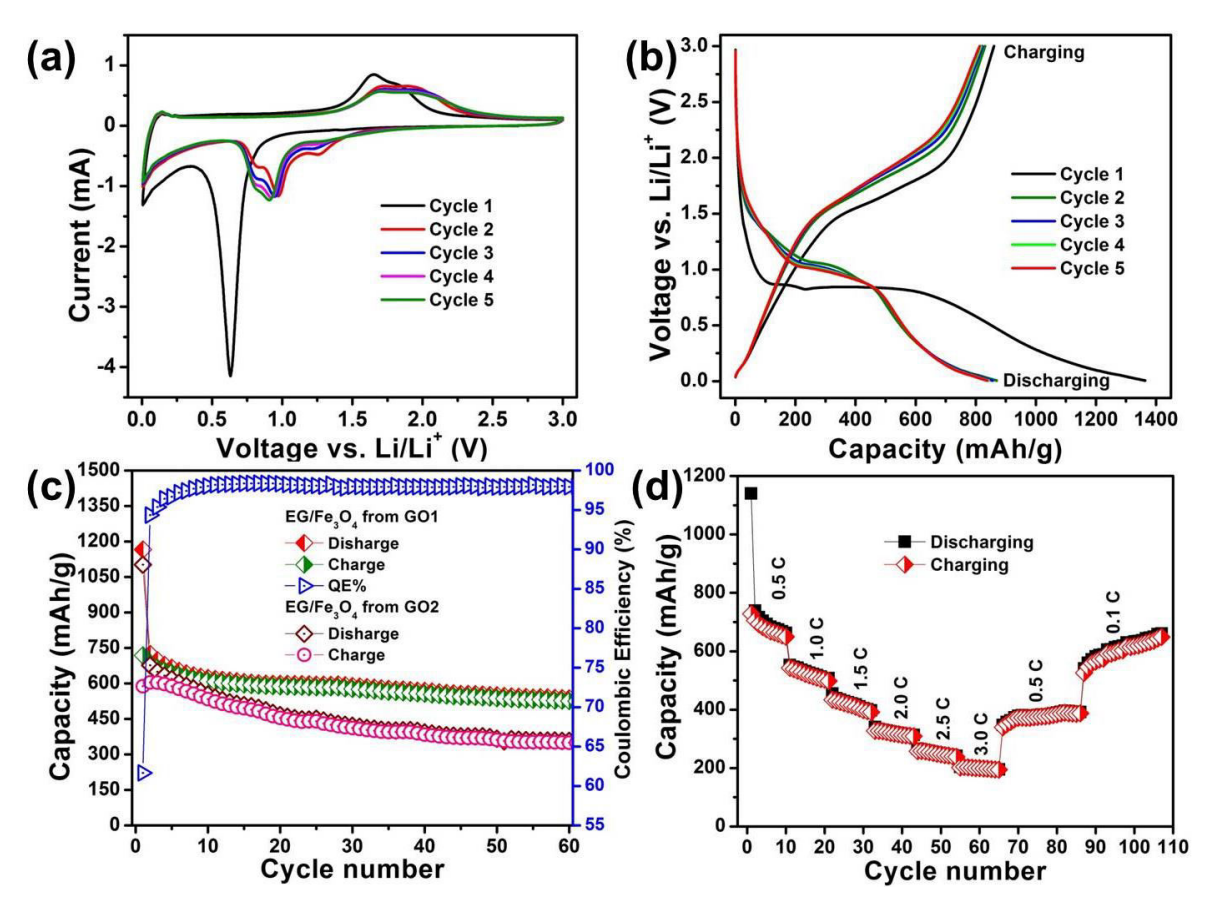


Fig. 4.14. Electrochemical characterization results of Fe₃O₄/FLG–550 °C–5h as an anode material in LIB in half cell configuration; (a) CV curves at 0.1 mV/s, (b) charge-discharge curves at 0.1 C, (c) cyclic performance at 0.5 C in comparison of Fe₃O₄/FLG–650 °C–5h and (d) rate capability.

During first discharging at 0.1 C rate Fe₃O₄/FLG–550 °C–5h is found capable of storing lithium up to maximum of 1364 mAh/g but out of this, 860 mAh/g of capacity can be reversible during

first charge that is equivalent to 63% of Coulombic efficiency (QE). Soon after first few cycles onwards QE values are found about 98% till the end of cycling as shown in Fig. 4.14(c) for 0.5 C cycling. The rapid capacity decay occurred up to first five cycles of 0.5 C cycling is a consequence of electrode formation effect in which anode matrix undergoes structural changes to achieves improved electrical contacts and proper percolation of electrolyte. In addition SEI formation and partly irreversible electrochemical rupturing of Fe₃O₄ crystals during first cycle are also responsible for the observed capacity decay. Once the electrode formation completes stable capacities will be achieved as observed in Fig. 4.14(c). These combination of loses increases with increasing current rate and for this reason 0.1 C (Fig. 4.14(b)) cycling differs slightly from 0.5 C (Fig. 4.14(c)). Here Fe₃O₄/FLG–550 °C–5h showed good cycling stability with 150 mAh/g of more capacity than Fe₃O₄/FLG-650 °C-5h. Fe₃O₄/FLG 550 °C-5h exhibited good rate capability at current rates ranging from 0.5 to 3.0 C as shown in Fig. 4.14(d). When current was switched back to 0.5 C from 3.0 C, the full capacity was not regained but increasing capacity trend at both 0.5 and 0.1 C signifies it takes longer aging time to come back to the starting capacity values. The observed capacity increase is a consequence either from in-situ electrochemical exfoliation of FLG [19] or enhancement of iron oxides reversibility or contribution from both the factors simultaneously. Fe₃O₄/FLG-550 °C-5h showed better capacity values than its class of materials such as FeO/FLG, graphene-Fe₃O₄ composites [17-20]. Fe₃O₄/FLG-550 °C-5h could outperform other advanced graphene-Fe₃O₄ composites [18,21-26] if clustering is avoided and uniform distribution of Fe₃O₄ nanoparticles on FLG surfaces is achieved. Such improvements can be pursued by mixing initial reagents in solution medium.

4.1.3 Fe₂Mo₃O₈/FLG Composite

Physical morphology of the as-synthesized Fe₂Mo₃O₈/FLG composite powder observed by FESEM at different magnifications is as shown in Fig. 4.15. As seen in the Fig. 4.15(a), (d) and (f), Fe₂Mo₃O₈ particulates possess disc like hexagon shaping are densely populated with very less FLG phase. In another region such as Fig. 4.15(b) and (c) Fe₂Mo₃O₈ discs are piled up on the surface of large FLG sheet. But this kind of scenarios are less in numbers whilst Fig. 4.15(a) and (f) morphology is the most commonly observed. Thickness and lateral sizes of the individual discs found at the order of 200 nm and 1 μm, respectively, which are very high compared to controlled compounds Co₂Mo₃O₈, Mn₂Mo₃O₈ and Zn₂Mo₃O₈ whose respective dimensions are around 55 and 300 nm [27]. Further TEM analysis (Fig. 4.16(a) and (d)) revealed that surfaces of Fe₂Mo₃O₈ discs are free from EG or FLG sheets which is quite

opposite to our previous morphological studies on similar composites [27]. EG or FLG is very rarely present near to the discs (Fig. 4.16(c)) but its abundance is more where the crystal growth appeared incomplete that most plausibly took place due to lack of Fe or Mo-precursors. Whatever EG or FLG left seems to be half consumed as suggested by selected area electron diffraction (SAED) pattern depicted (diffused ring) in inset of Fig. 4.16(b) that indication for purely amorphous nature. The SAED pattern of Fe₂Mo₃O₈ disc depicted in Fig. 4.16(d) belongs to [024] facet of hcp system. Thus FESEM and TEM studies clearly evidenced the formation Fe₂Mo₃O₈/FLG in tune with each other. XRD pattern of as-synthesized Fe₂Mo₃O₈/EG before and after Rietveld refinement is shown in Fig. 4.17. It contained strong intense reflections mainly from of Fe₂Mo₃O₈ phase and weak residual graphitic peak at 26.5° adjacent to the (102) peak. The pattern of Fe₂Mo₃O₈ phase matches with hcp (PDF # 36-526) structure. Lattice parameters of Fe₂Mo₃O₈ are found from the refinement are a = b = 5.781(3) Å and c = 10.062(5) Å with an average crystallite size of 39.8 nm.

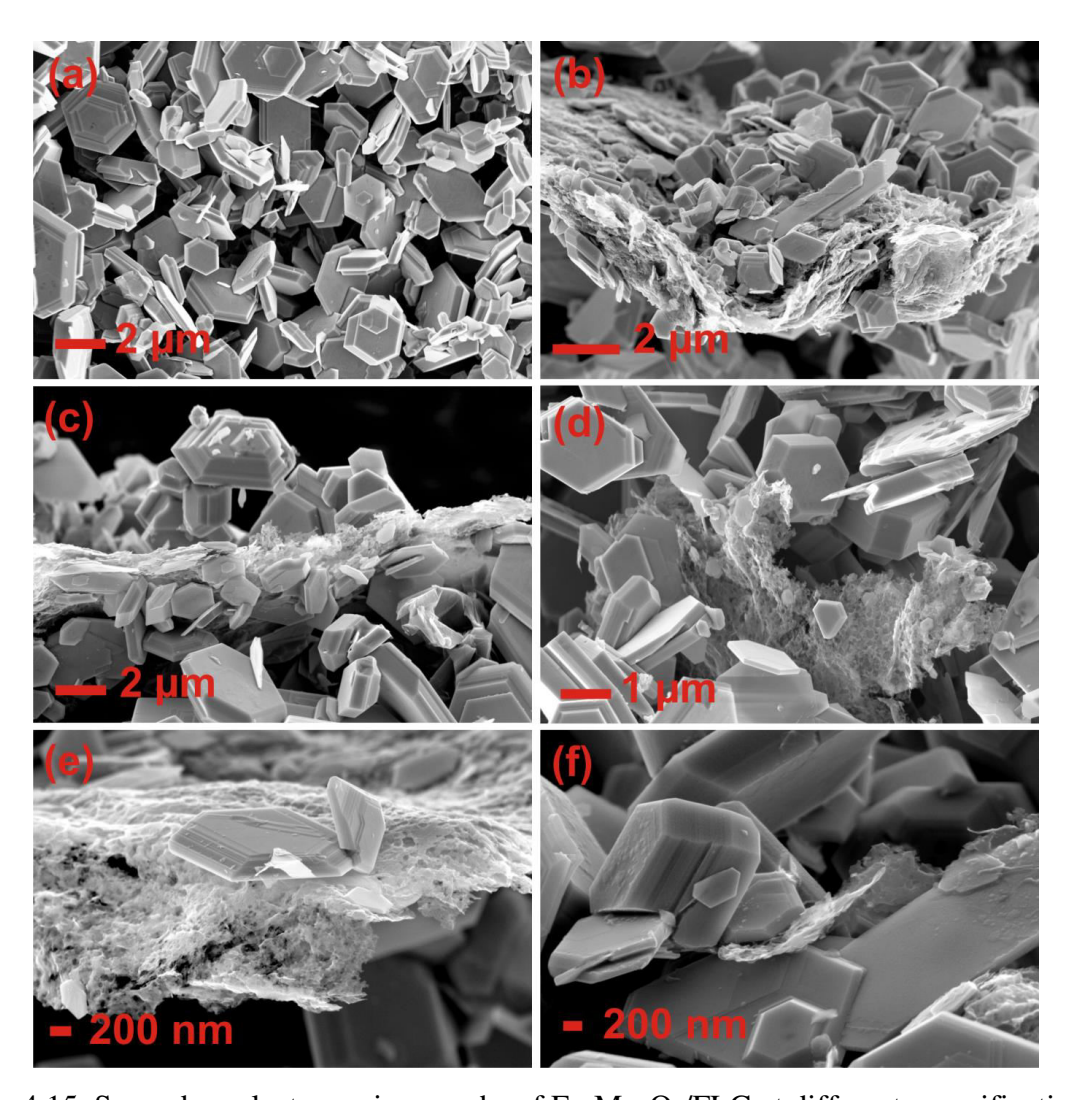


Fig. 4.15. Secondary electron micrographs of Fe₂Mo₃O₈/FLG at different magnifications.

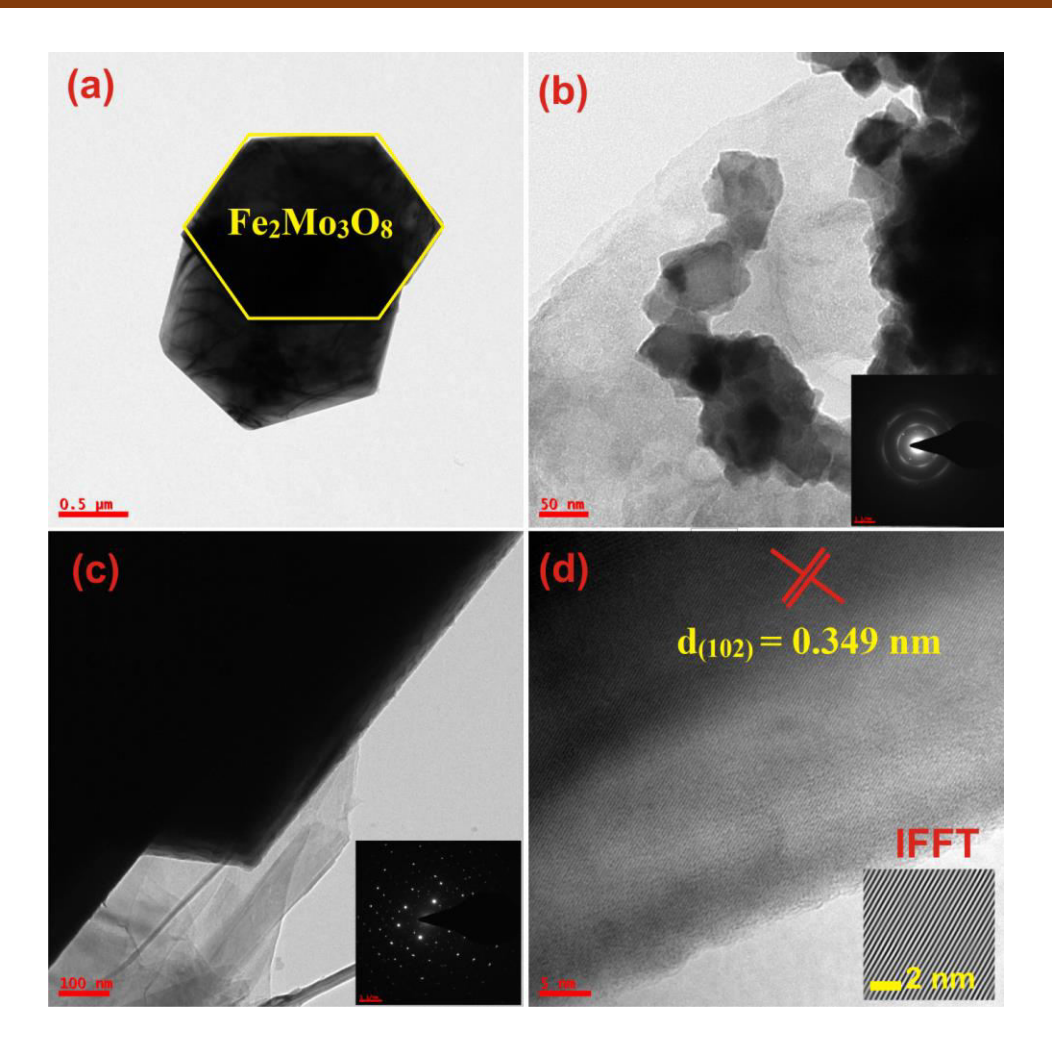


Fig. 4.16. TEM images of Fe₂Mo₃O₈/FLG at different magnifications; inset in (c) is the selected area electron diffraction pattern while that in (d) is inverse fast Fourier transform image of (102) lattice fringes corresponding to Fe₂Mo₃O₈.

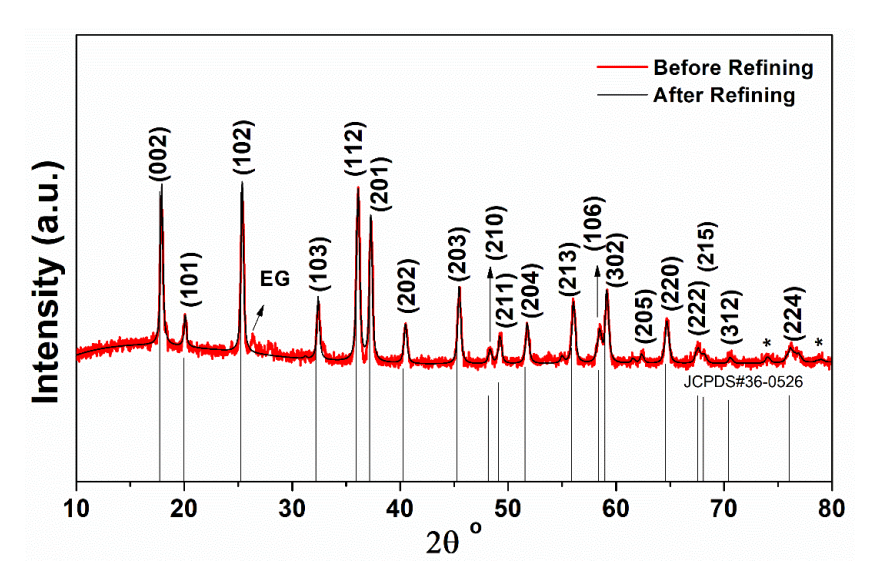


Fig. 4.17. X ray diffraction (XRD) pattern of Fe₂Mo₃O₈/Few layer graphene (FLG) along with Rietveld refined data and JCPDS data of Fe₂Mo₃O₈.

Raman spectrum of Fe₂Mo₃O₈/FLG G in comparison to GO is shown in Fig. 4.18. Fe₂Mo₃O₈/EG spectrum contained strong bands at 274, 344, 745, 812 and 926 cm⁻¹ that originates from different modes of vibration in Fe₂Mo₃O₈ crystal system [27]. Additionally, it contained characteristic D and G-bands of FLG at 1355 and 1573 cm⁻¹ those are found at 1355 and 1588 cm⁻¹ in the case of GO. This peak positions indicates decrease in number of graphene layers of EG when compared to GTR synthesized FLG-A₂Mo₃O₈ composites in which D and G-bands were found at 1360 and 1599 cm⁻¹ [27]. This shift in the band positions of towards lower wave number not only suggest less number of graphene layers but also decrease in weight content consistent with physical morphology seen in electron micrographs. The intensity ratio I_D/I_G of FLG is found to be ~0.79 whereas in the case of GO it was ~1.02. The higher I_D/I_G ratio of GO is an indication for high extent of oxidation that creates more number of sp³ domains which means nothing but an increase in disorder [2]. After heat treatment of the reaction mixture GO loses most of the functional groups in order to transform into FLG and thus a rapid conversion of sp³ domains to sp² takes place [2]. As a consequence, I_D/I_G ratio decreases to 0.79 (from 1.02) due to reduction in sp³ domain population and thus FLG acquires more ordering. The 2D-band of GO seems to be feeble around 2700 cm⁻¹ but its re-appearance in EG indicates recovery of stalking order along crystallographic c-axis direction [2]. That is why a residual graphitic (002) peak is observed in XRD analysis that is a common feature in the family of FLG-A₂Mo₃O₈ composites [27].

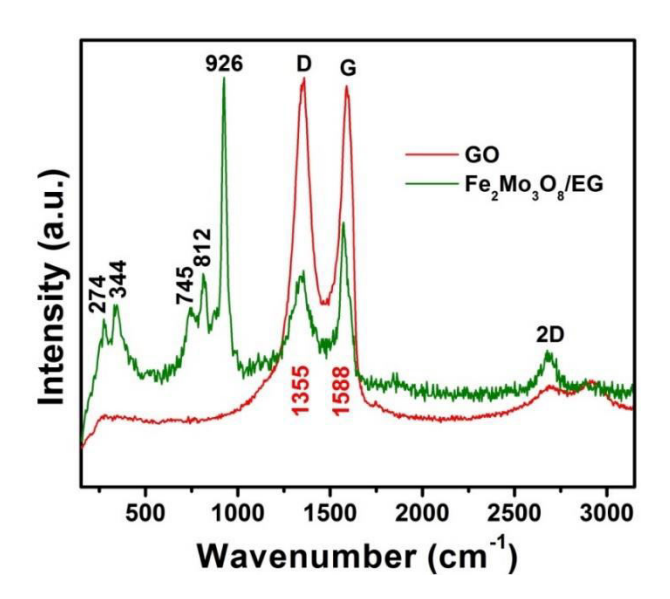


Fig. 4.18. Raman spectrum of Fe₂Mo₃O₈/FLG in comparison with that of GO.

To further understand the oxidation states of various elements in the as-synthesized $Fe_2Mo_3O_8/FLG$ composite, high-resolution XPS data (Fig. 4.19) was collected. Fe 2p X-ray photoelectron spectrum (Fig. 4.19(a)) of the composite showed two distinct binding energy (BE) peaks at 711.8 and 717.9 eV corresponding to Fe $2p_{3/2}$ and $2p_{1/2}$ orbitals, respectively. The difference between the peak positions is ~ 6 eV confirming +2 oxidation state of Fe. In addition, the absence of any satellite peaks in-between the peak positions corresponding to Fe $2p_{3/2}$ and $2p_{1/2}$ orbitals is in good agreement with previously reported XPS data on Fe 2p for Fe^{2+} . Mo 3d core level (Fig. 4.19(b)) was found to split into two characteristic doublets at $\sim 230.9-234.1$ eV (Mo $3d_{5/2}-3d_{3/2}$ doublet) and $\sim 233.1-236.2$ eV corresponding to the confirmation of +4 oxidation state of Mo and Mo^{6+} as a consequence of either surface oxidation or degradation as noticed in the case of $Co_2Mo_3O_8$ -rGO composite, respectively [29].

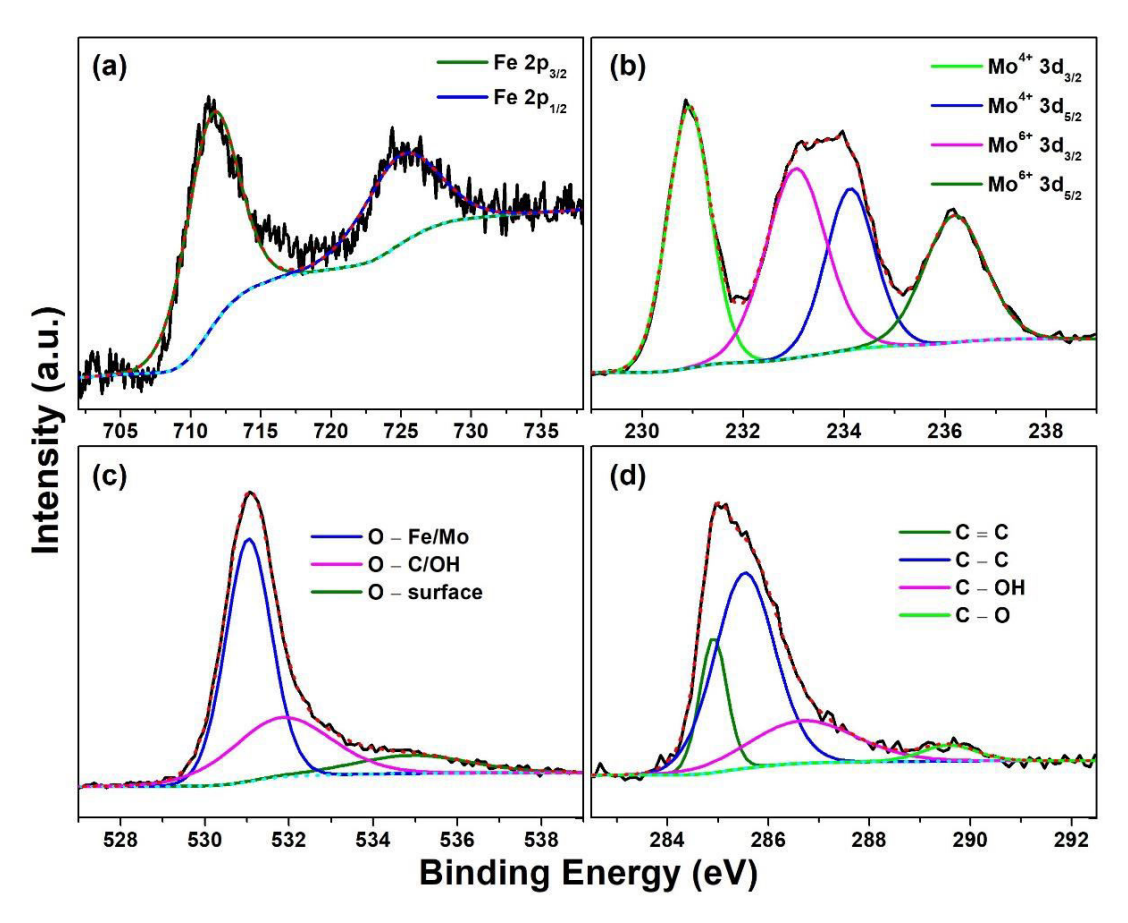


Fig. 4.19. X-ray photoelectron spectra of Fe₂Mo₃O₈/FLG; (a) Fe 2p (b) Mo 3d (c) O 1s (d) C 1s.

O 1s X-ray photoelectron spectrum (Fig. 4.19(c)) contains three peaks at \sim 531, \sim 532 and \sim 535 eV confirming the presence of oxygen that bonded to either Mo or Fe at crystallographic sites, carbon directly or through hydroxyl group and surface adsorbed moisture, respectively. C 1s X-ray photoelectron spectrum (Fig. 4.19(d)) shows four peaks at \sim 284.9, 285.5, 286.7 and 289.6 eV which matches with C = C (sp²), C - C (sp³), C - OH and C - O bonding modes,

respectively. Thus, XPS analysis confirmed that Fe and Mo elements in Fe₂Mo₃O₈/FLG composite are found in II and IV oxidation states while FLG is in excellent reduced form of GO.

Fig. 4.20(a) shows N₂ adsorption and desorption isotherms of Fe₂Mo₃O₈/FLG composite. The isotherms resemble type III and IV isotherms of BET classification, respectively. BET analysis shows that the composite possesses a low specific surface area of ~3 m² g⁻¹ with an average pore size of ~8 nm and pore volume ~0.006 cm³ g⁻¹. The small hysteresis between adsorption and desorption and the low specific surface area indicate low porosity, which might be plausibly due to less amount of FLG and high crystalline quality of micron-sized Fe₂Mo₃O₈ platelets as discussed above. Thermo gravimetric analysis (TGA) plot of Fe₂Mo₃O₈/FLG composite is shown in Fig. 4.20(b). The initial weight gain of ~4.7% originates from the oxidation of Fe₂Mo₃O₈ to form intermediate compounds such as Fe₂Mo₃O₁₂ in which Fe and Mo are present in +3 and +6 oxidation states [28-30]. Such higher oxidation state compounds eventually decompose above 800 °C to different Fe and Mo compounds. The subsequent weight loss of ~1.88% in the temperature range 540-800 °C is a consequence of graphene basal plane's oxidative decomposition which represents the overall weight content of FLG present in the composite as noticed in similar cases [2,3,17,27,28,30-32]. Because of this low FLG content, the low specific surface area might have resulted in BET measurement as perfect Fe₂Mo₃O₈ crystals are unable to adsorb N₂ molecules. Thus, Fe₂Mo₃O₈ and FLG are in 98 and 2 wt.%, respectively in the composite and therefore correspond to a theoretical lithiation capacity of 871 mAh g⁻¹.

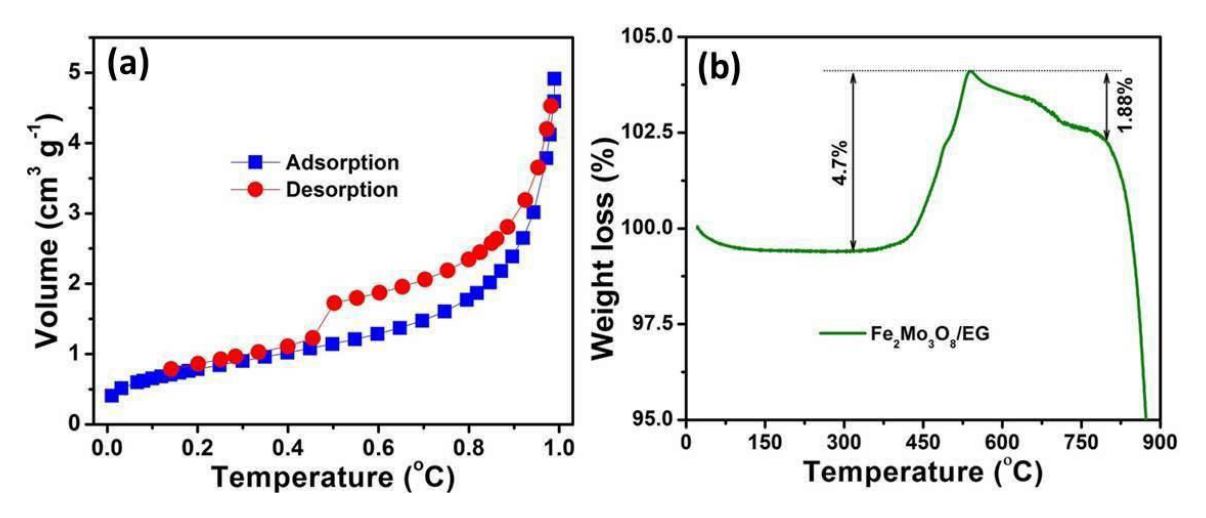


Fig. 4.20. (a) BET N₂ adsorption-desorption isotherms (b) TGA of Fe₂Mo₃O₈/FLG.

Lithiation characteristics of Fe₂Mo₃O₈/FLG are probed using Cyclic Voltammetry (CV) and galvanostatic cycling (GC) testing and are shown in Fig. 4.21. During the first cathodic scan, CV curve depicts peaks at 1.45, 0.68 and 0.005 V with increasing intensity (Fig. 4.21(a)). These three peaks collectively originate from crystal destruction (amorphization) of Fe₂Mo₃O₈ during lithiation and electrolyte decomposition on both Fe₂Mo₃O₈ and EG phases [27,28]. These peaks were not observed from second cathodic scan onwards indicating that part of the first lithiation process is irreversible. Such irreversible reactions lead to solid electrolyte interface (SEI) formation. The residual functional groups such as – OH and – O groups as revealed by XPS analysis and disordered carbon in EG as revealed by Raman scattering mainly account for the irreversible SEI compounds such as LiOH, Li₂C₂, Li₂CO₃ etc. The majority of current from 1.5 to 0.005 V comes from lithiation by conversion reactions presented under Introduction and remaining non-zero current in the voltage range 3.0-0.005 V is a consequence of electrochemical adsorption of Li onto FLG [3,33].

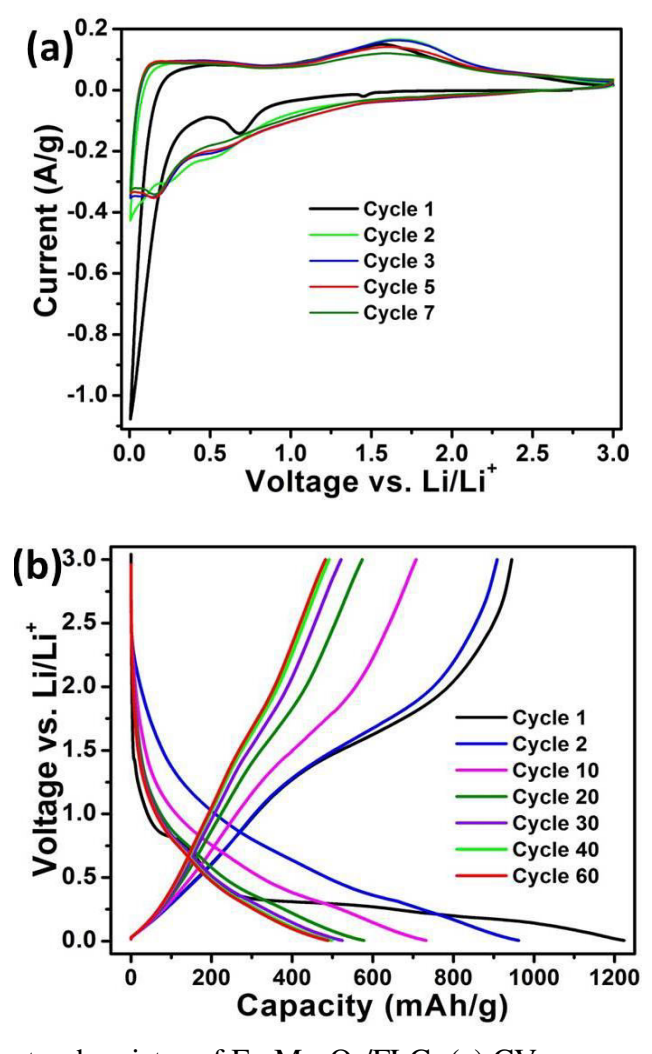


Fig. 4.21. Anodic electrochemistry of Fe₂Mo₃O₈/FLG: (a) CV curves at a scan rate of 0.1 mV/s and (b) GC charge-discharge profile at a current density of 50 mA/g.

There are no peaks noticed in the entire anodic scan except for a broad band that extended from 1.0 V to 2.2 V, which might correspond to de-lithiation from amorphous phase conversion reactions [27,28,30,34]. The remaining non-zero oxidizing current observed in-between 0.005-3.0 V comes from electrochemical desorption of lithium from FLG. The reactions (1-3) are in good agreement with Fe in +2 and Mo in +4 oxidation states as clearly observed in Fe 2p and Mo 3d XPS spectra, respectively.

$$2Fe + 2Li_2O \leftrightarrow 2FeO + 4Li^+ + 4e^- \qquad (1)$$

$$3Mo + 6Li_2O \leftrightarrow 3MoO_2 + 12Li^+ + 12e^- \qquad (2)$$

$$Fe_2Mo_3O_8 + 16Li^+ + 16e^- \leftrightarrow 8Li_2O + 2Fe^0 + 3Mo^0 \qquad (3)$$

All in all, the CV features resembled pseudo-capacitance behavior and are in close agreement with the characteristics of a similar class of materials. Voltage versus charge-discharge characteristics of Fe₂Mo₃O₈/FLG (Fig. 4.21(b) are consistent with CV observations. The plateaus around 1.5 and 0.7 V that extend to 0.005 V observed during the 1st discharge are in good agreement with 1st cathodic CV peaks. To complete 1st discharge to 0.005 V, Fe₂Mo₃O₈/FLG composite exhibited a high capacity of 1224 mAh g⁻¹, which is 1.5 times the theoretical capacity (813 mAh g⁻¹ for 16 moles of Li uptake as per the conversion reactions) of the bare metal cluster and approximately equals to 24 moles of Li uptake. The 2nd and subsequent discharge curves bear similar features except for the capacity fading, which is also noticed in the charging case. During the 1st charge, a plateau-like feature noticed in the voltage range 1.0-2.0 V corresponds to the broad hump in the CV curve in the same voltage range. The decrease in intensity of this broad hump as observed during CV cycling re-appeared as the capacity gradually faded (as observed in GC) with each charge.

A high reversible capacity of 945 mAh g⁻¹ is observed at the end of the first charge to 3.0 V which is ~78 % (Coulombic efficiency, QE) of the first discharge capacity. This capacity and QE values are superior to a similar class of materials as summarized in Table 4.2. A gradual capacity fading all across the 40th cycle (Fig. 4.22(a)) is noticed, from where capacity stabilized nearby 500 mAh g⁻¹. Despite this capacity fading, QE values remained as 98-99% throughout the cycling except for first few cycles. Further, rate capability (Fig. 4.22(b)) is found fairly good compared to its familial materials namely FLG-Mn₂Mo₃O₈ [27], FLG-Zn₂Mo₃O₈ [28], commercial graphite etc. The inferior cycling performance w.r.t capacity value is due to lack of proper amount of graphene (FLG) as evidenced in electron micrographs and TGA. Literature data presented in Table 4.2 suggests that an increase in FLG weight content say 10 to 20%

could boost up capacity values similar to Fe₂Mo₃O₈-RGO and Co₂Mo₃O₈-rGO composites [28,34]. It is essential to have higher amounts of FLG which brings good synergy with Fe₂Mo₃O₈ platelets to ease superior performance despite inevitable initial losses.

Compound Name	Graphene (wt.%)	Current (mA g ⁻¹)	1 st Charge Capacity (mAh g ⁻¹)	1 st QE (%)	50 th Charge Capacity (mAh g ⁻¹)
Fe ₂ Mo ₃ O ₈ /FLG (present work)	1.88	50	945	77	490
FLG-Co ₂ Mo ₃ O ₈ [27]	17.2	60	907	67	785
FLG-Mn ₂ Mo ₃ O ₈ [27]	7.7	60	937	69	495
FLG-Zn ₂ Mo ₃ O ₈ [27]	6.7	60	448	53	630
Co ₂ Mo ₃ O ₈ -rGO [28]	22	60	1170	64	997
Mn ₂ Mo ₃ O ₈ -rGO [30]	10.3	200	663	72	
Fe ₂ Mo ₃ O ₈ -RGO [34]	8.3	200	923	72	

Table 4.2. Cyclic performance of Fe₂Mo₃O₈/FLG in comparison to several reported works.

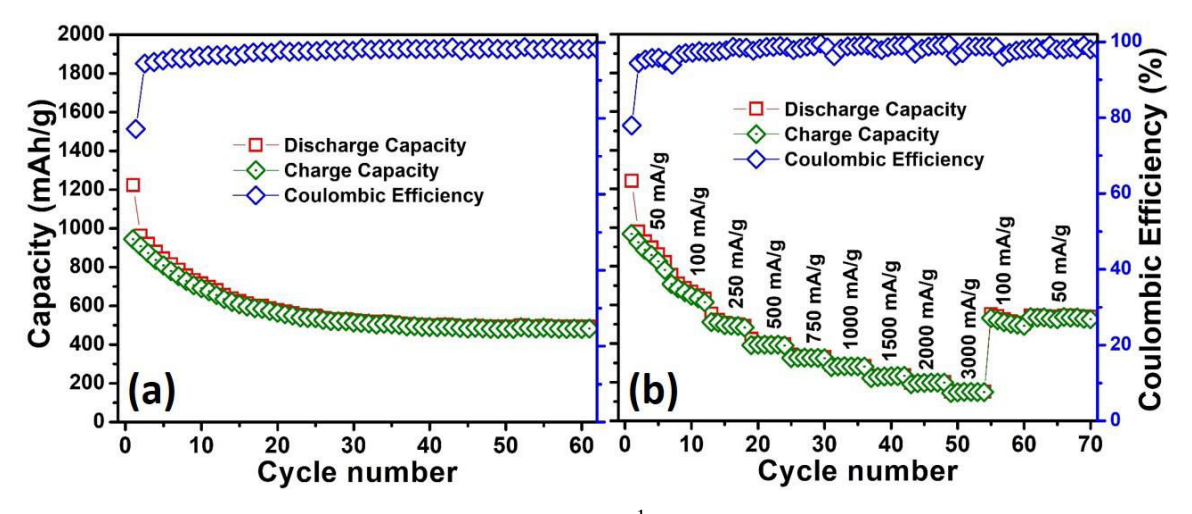


Fig. 4.22. (a) Cycling performance at 50 mA g⁻¹ and (b) rate capability of Fe₂Mo₃O₈/FLG.

4.2 MnO/FLG Composite as Electrode Material in Supercapacitor

FESEM images showing the morphology of the as-synthesized MnO/FLG composite are shown in Fig. 4.23. From the images it is clear that lumps of MnO nanoparticles are distributed on the surfaces of the exfoliated graphene sheets. High magnification image of one such lump (Fig. 23(d)) shows a network MnO nanoparticles. To further study the morphology and crystallinity of MnO/FLG, TEM analysis was carried out on the powder sample. TEM images (recorded at different magnifications) of the as-synthesized MnO/FLG composite are shown in Fig. 4.24. Low magnification TEM image (Fig. 4.24(a)) shows micron and nano sized MnO particles, and lumps of MnO particles (as observed under FESEM) are distributed on the

graphene sheets. Fig. 4.24(b) shows MnO nanoparticles are uniformly decorated on FLG sheets. Fig. 4.24(c) shows one MnO particle and its SAED pattern with well-ordered bright spots (inset of Fig. 4.24(c)) clearly indicating highly crystalline nature of MnO. Fig. 4.24(d) shows the HRTEM image of the composite. HRTEM clearly shows the lattice fringes corresponding to (111) planes of MnO with an interlayer spacing of 0.257 nm. In the same HRTEM image, FLG is also observed. The above observations clearly show that cyrstalline MnO particles are decorated on the exfoliated graphene sheets. XRD patterns of GO and MnO/FLG are shown in Fig. 4.25. In the case of GO, the peak at 20 equals to 10.8° is indexed to (001) graphitic peak corresponding to the interlayer spacing of 0.86 nm due to the oxidation of graphite. In the case of MnO/FLG powder, the XRD peaks are matching with the JCPDS cart no 75-257 and space group Fm-3m (no. 225) corresponding to crystalline MnO. From the above analysis, MnO₂ is converted into MnO phase. Elemental mapping of MnO/FLG at low magnification as shown in Fig. 4.26, confirms the presence carbon (C), Manganese (Mn), oxygen (O).

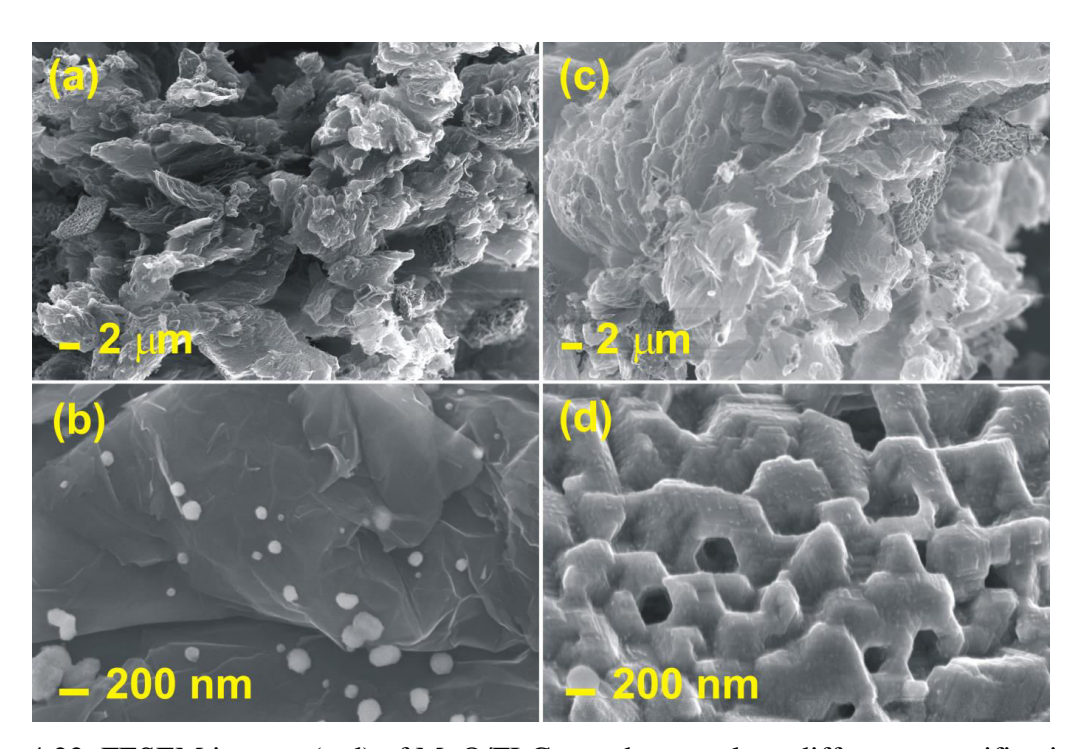


Fig. 4.23. FESEM images (a-d) of MnO/FLG powder sample at different magnifications.

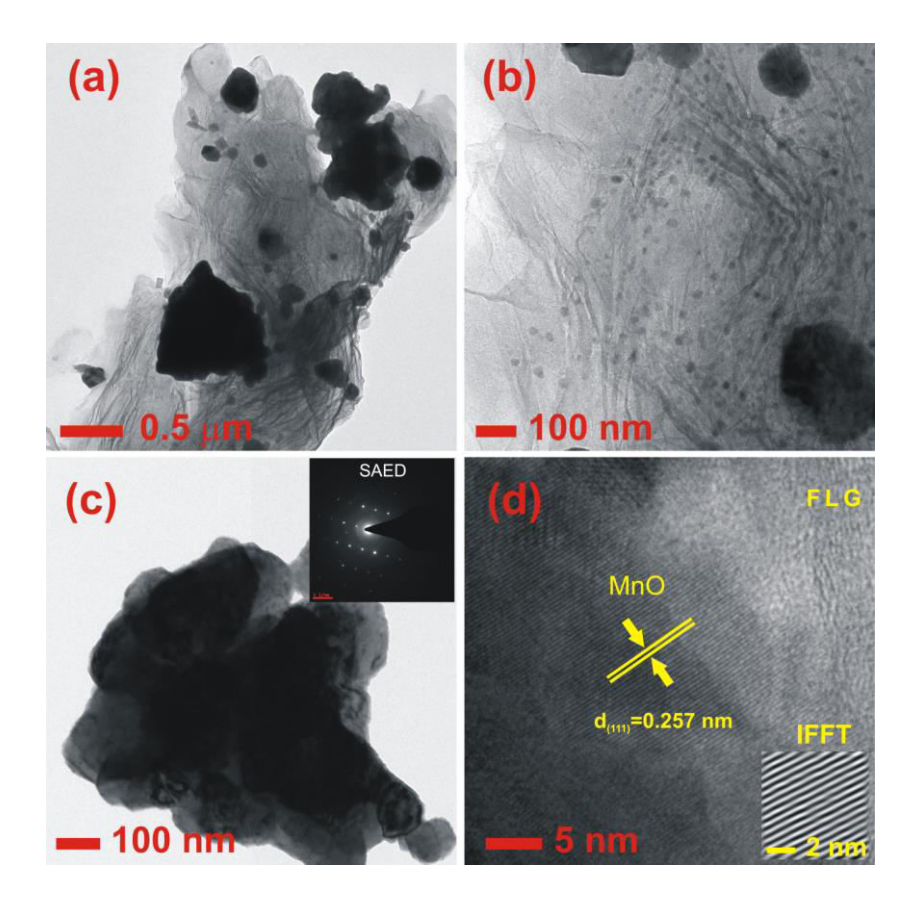


Fig. 4.24. (a) and (b) representative TEM images of MnO/FLG nanocomposite, (c) high magnification TEM image of one MnO particle with SAED patter in the inset and (d) HRTEM image of FLG/MnO nanocomposite.

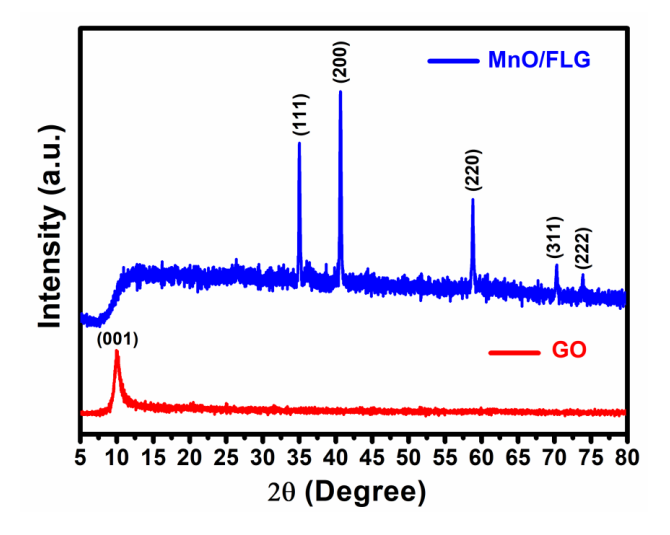


Fig. 4.25. XRD patterns of GO and MnO/FLG nanocomposite.

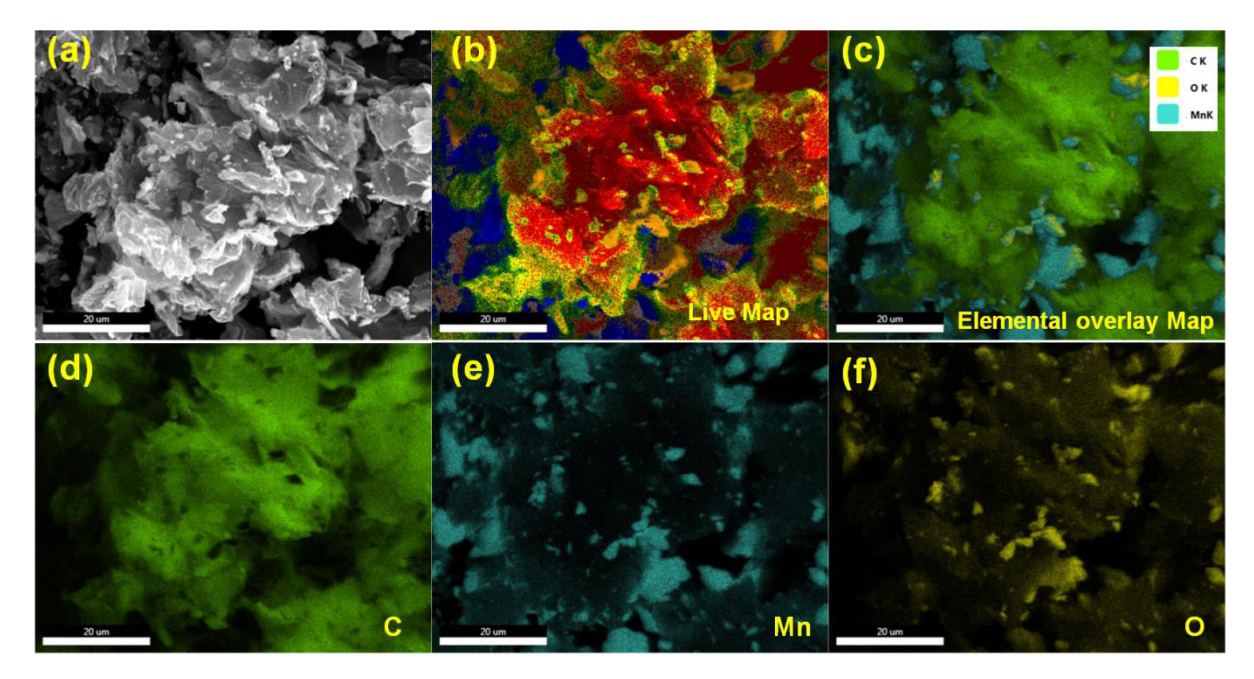


Fig. 4.26. Elemental (C, Mn and O) maps (FESEM based) of MnO/FLG composite.

Fig. 4.27 shows Raman spectra of graphite, GO, and MnO/FLG nanocomposite. In the case of graphite, the three fingerprint bands namely D-band, G-band, and 2D-band are observed at 1348.57, 1577.7 and 2703.27 cm⁻¹, respectively. In the case of GO, the same bands are observed at 1352.72, 1593.82, and 2692.2 cm⁻¹, respectively. In the case of MnO/FLG, the D-band and G-band are observed at 1348.57 and 1597.85 cm⁻¹, respectively and a small peak observed at 661.24 cm⁻¹ has been designated to Mn-O vibration mode.

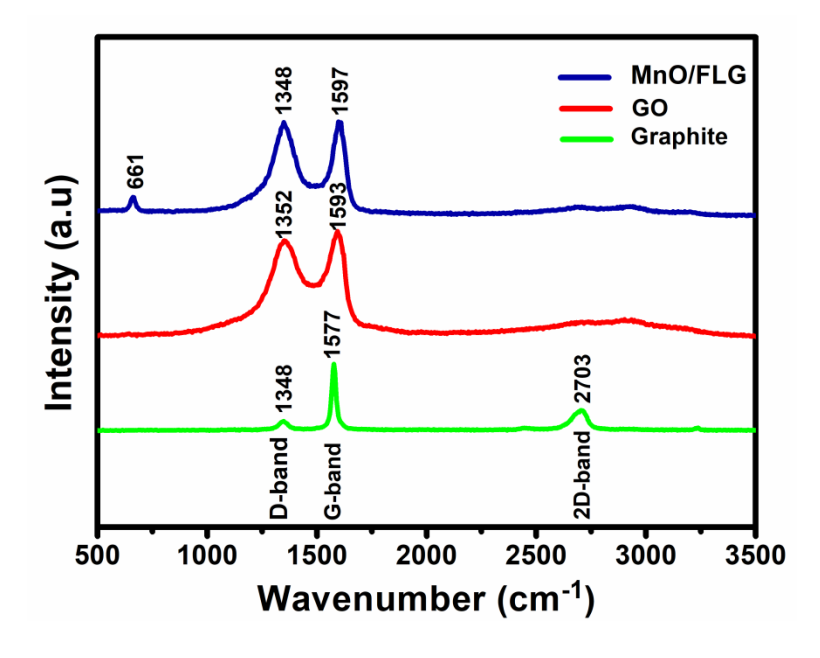


Fig. 4.27. Raman spectra of graphite, GO and MnO/FLG nanocomposite.

To study the electrochemical performance of the as-fabricated MnO/FLG composite, cyclic (CV), voltammogram galvanostatic charge/discharge, electrochemical impedance spectroscopy (EIS) techniques were used in the presence of 1M lithium sulphate (Li₂SO₄) aqueous solution using three electrode configuration. CV has been considered as an appropriate technique to study the occurrence of faradic or non-faradic reactions in the electrode [36]. CV measurements are carried in a Voltage window range between 0.0 to +1.0 V at different scan rates of 1, 3, 5, 8, 10, and 20 mV S⁻¹ and the corresponding capacitance values are 751, 586, 458, 321, 289, and 192 Fg⁻¹, respectively. The observed CV curves of MnO/FLG are shown in Fig. 4.28(a). Broad pair of anode and cathode peaks can be observed at 0.82 and 0.25 V. The broadness of peaks signifies pseudo-capacitive nature of the electrode. The cathodic peak observed at 0.82 V indicates insertion of 2 Li⁺ ions into MnO structure while the anodic peak observed at 0.25 V is attributed to extraction of 2 Li⁺ ions. All in all, the CV peaks are the redox pairs of MnO to Mn conversion [36,37] according to the following reaction:

$$MnO + 2 Li^+ + 2e^- \longrightarrow Li_2O + Mn$$

It can be observed that with increasing scan rates the current response and integral area of CV curves increased indicating a good rate capability of the composite. The polarization value is also decreased from 1-20 mV s⁻¹ confirm increasing charge transfer kinetics of the composite owing to utilization of highly active Mn species [38]. Therefore the obtained increased current for MnO/FLG composite is attributed to the combined contribution of redox pseudocapacitance of MnO and the electrical double layer capacitance of FLG [39].

Galvanostatic charge/discharge technique was used to further evaluate the performance of MnO/FLG composite as a super capacitive electrode material. A plot of potential versus time at various current densities (0.5, 1, 10, 50, 100 mA g⁻¹) with the potential window range between 0 to +1V is shown in Fig. 4.28(c). The nonlinear nature of the charge/discharge curves exhibited by MnO/FLG composite is representative of pseudo capacitive behavior. The discharge time decreased by increasing from low to high current densities which are due to the kinetics of the redox reaction of MnO/Mn within this voltage range and consistence with CV curves. At higher current densities, it is clear that the electrolyte ions are unable to enter the internal structure of the electrode material. The standard equation used to estimate the specific capacitance of the electrode from galvanostatic test [40] is $S_C = \frac{I}{m(\frac{dv}{dt})}$ where S_C (Fg⁻¹) is

the specific capacitance, I (Ampere) represents the response of current density, m (g) is the mass of the active FLG/MnO electrode material loaded on substrate, and dv/dt is the slope of the discharge curve.

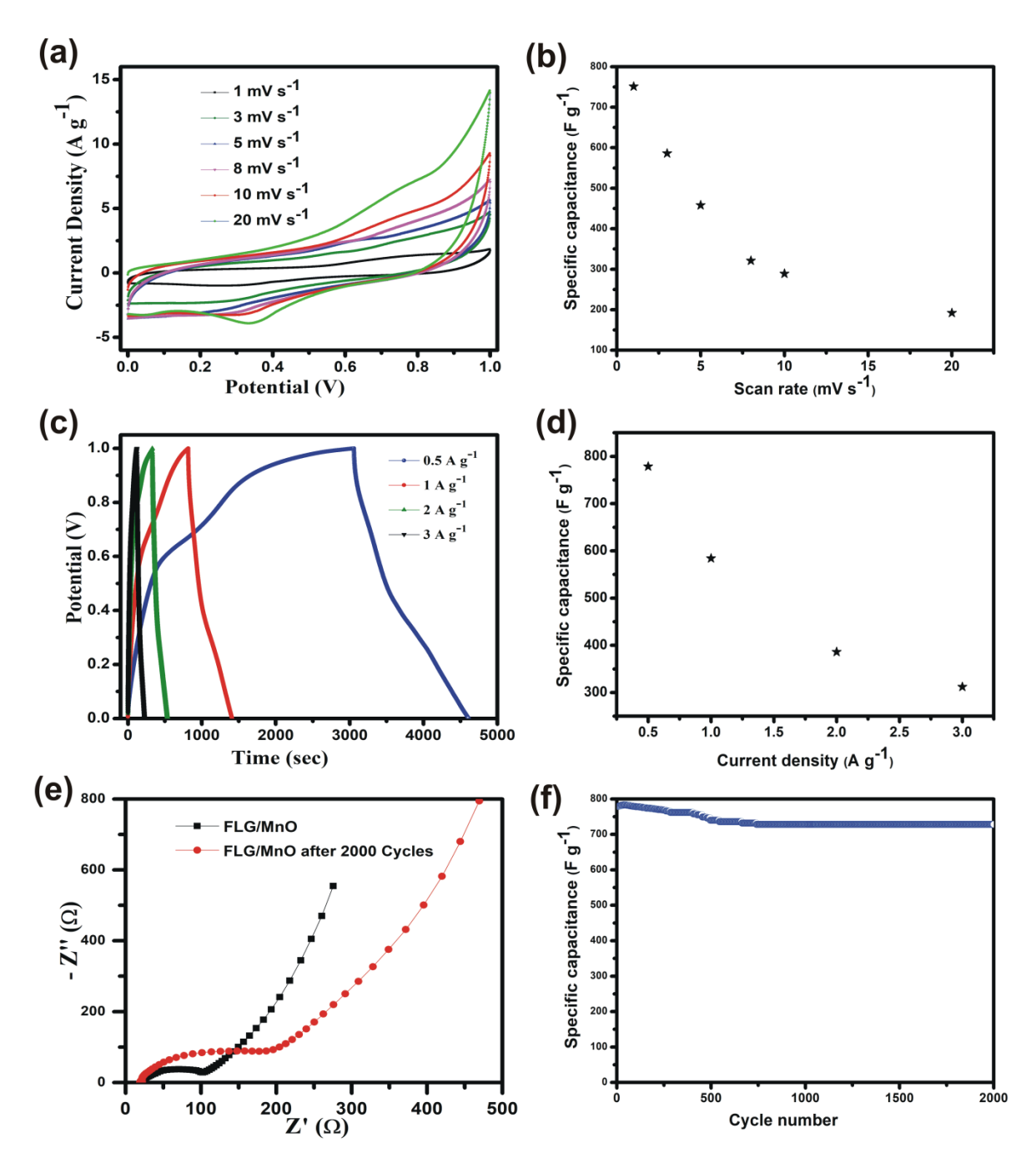


Fig. 4.28. (a) Cyclic Voltammetry curves at different scan rates (b) specific capacitance Vs. scan rates (CV based) (c) Galvanostatic charge /discharge curves at different current densities (d) specific capacitance Vs. current densities (GC based) (e) Nyquist plot before and after 2000 cycles and (f) long term cycling for 2000 cycles at 1 mAg⁻¹ of MnO/FLG composite.

The specific capacitance values of MnO/FLG composite electrode calculated from the charge/discharge curves at various current densities of 0.5, 1, 2 and 3 A g⁻¹ are 778.5, 584, 386, and 312 Fg⁻¹, respectively. As we know from previous reports, typical reduced graphene oxide has very less specific capacitance (around 120 Fg⁻¹) and MnO is very less reported w.r.t specific

capacitance but its theoretical capacitance is 1370 Fg⁻¹, however both of these have drawbacks when used individually as supercapacitor electrode material. In this work, the highest capacitance value is as high as 778.5 Fg⁻¹ at 0.5 A g⁻¹ owing to the synergic effect between FLG and MnO. It is clear from the microstructural observations that the 3D MnO networks made possible the M-N porous structured network and as a consequence the composite offered a high contact surface area of electrode/electrolyte resulting in enhancement of the transport of cations and decrease the polarization, which is beneficial to shorten the cation path into the electrode matrix and thereby improving the overall discharge capacitance. The capacitance is monotonically decreased with increase in current density due to the rapid movement of electrolyte ions and thereby cannot intercalate with the active MnO electrode material, which obviously led to low specific capacitance.

Fig. 4.28(e) shows the EIS spectra of MnO/FLG composite electrodes for 1st and after 2000th discharge cycle. It is confirmed that the MnO/FLG composite has higher charge transfer capacticy as represented by the diameter of the semicircle in the medium frequency region. Both EIS curves are composed of three parts. The interception of X-axis at high frequency indicates that the solution resistance or ohmic resistance (Rs) contributed by the electrolyte. The depressed semicircle at high to intermediate frequency range originated evidence of the charge transfer resistance R_{ct} corresponding to solid state diffusion of Li⁺ in the bulk of the active material and the contact phase angle element (CPE) includes double layer capacitance [41]. Further, in the low-frequency region, a straight line is ascribed to the Warburg impedance corresponding to the Li-ion diffusion through the MnO electrode. The depressed semicircle of MnO/FLG composite is (charge transfer resistance) higher electronic and ionic conductivity. It is also clear to infer that the lower charge transfer resistance congruence to the smaller electrochemical polarization leads to better cycling performance. Here R_s indicates solution resistance, Rct charge transfer resistance, and CPE is constant phase element instead of double layer capacitance, and Zw is Warburg impedance. Results indicate that MnO/FLG composite (1^{st} cycle) , and MnO/FLG composite (after 2000th cycle) electrodes have $R_s = 30\Omega$, 40Ω , $R_{ct} =$ 150 Ω , 270 Ω , respectively. Therefore, EIS confirm that the graphene is not only improved electron conductivity but also provide fast migration/transport of Li - ions to reach the interior of M-N structured lumps.

A long cycle life is very important for a supercapacitor in order for it to be commercialized. The long-term cycling stability of MnO/FLG electrode investigated by repeating galvanostatic charge/discharge measurements between the potential windows 0 to 1 V at a current density of 1 mAg⁻¹ for 2000 cycles. From Fig. 4.28(f) it is clear that MnO/FLG composite electrode

exhibits a specific capacitance of 824 Fg⁻¹ and it still remained 774 Fg⁻¹ even after 2000 discharge cycles implying a capacity retention of 93%. The main reason for the decrease of the specific capacitance could be the slow dissolution of the electrode materials in the electrolyte solution. However, the observed long term cycle stability in the case of MnO/FLG composite makes it suitable for the next generation electrochemical energy storage devices.

4.3 Fe₃O₄/FLG Composite for Electrochemical Detection of Dopamine

Fig. 4.29(a-b) show low magnification FESEM images of Fe₃O₄/FLG (synthesized at 650 °C for 5 h) powder sample. It is clear from these images that Fe₃O₄ nanoparticles are distributed densely on the edges of the exfoliated graphene sheets. Slight aggregation of Fe₃O₄ nanoparticles was observed due to their super paramagnetic nature [42-45]. At the same time, the aggregation was also controlled because of the presence of exfoliated graphene sheets. Fig. 4.29(c) shows high magnification image of highly exfoliated graphene sheets decorated with Fe₃O₄ nanoparticles. In Fig. 4.29(d) it can be clearly observed that the Fe₃O₄ particles (of no particular shape) are uniformly anchored onto the exfoliated graphene sheets.

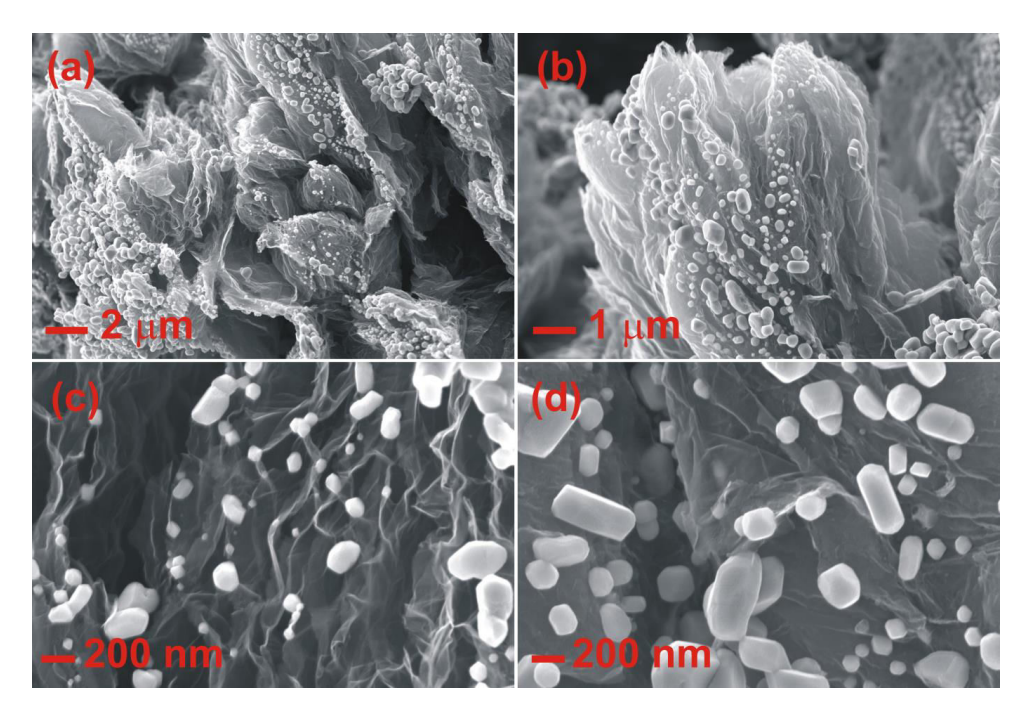


Fig. 4.29. FESEM images (a-d) of Fe₃O₄/FLG composite sample at different magnifications.

Fig. 4.30 shows the low magnification TEM micrographs of Fe₃O₄ particles which are tightly bonded together in a group wrapped by few layer graphene sheets. Fig. 4.30(a) shows larger sized (100-230 nm) Fe₃O₄ particles while Fig. 4.30(b) shows nano-sized (26 to 37 nm) Fe₃O₄ particles. Fig. 4.30(c) shows high-resolution TEM micrograph depicting (311) lattice fringes

with a spacing of 0.259 nm, which is consistent with the XRD results (Fig. 4.31)). Fig. 4.30(d) shows Fe₃O₄ particles are covered by surfaces and edges of the exfoliated graphene sheets and its inset shows SAED pattern showing bright diffraction spots pattern confirms highly crystalline in nature of Fe₃O₄. The TEM micrographs of Fe₃O₄/FLG are in good agreement with FESEM images. Moreover, electron micrographs show that the interfaces between Fe₃O₄ and FLG are clear and this is an important characteristic for electrochemical sensing of dopamine with Fe₃O₄/FLG as the sensing material. Fig. 4.31 shows the XRD patters on of assynthesized GO and Fe₃O₄/FLG. In the case of GO (inset of Fig. 4.31) (002) graphitic plane appears at 2θ equals to 11.2° corresponding to an interlayer spacing of 0.77 nm indicating the attachment of functional groups due to oxidation of graphite. In the case of graphite, (002) plane appears at 26.4° corresponding to a interlayer spacing of 0.34 nm. The XRD pattern of as-synthesized Fe₃O₄/FLG is indexed to cubic magnetite phase with a space group: Fd-3mZ (JCPDS cart No. 89-691). Fe₃O₄ crystallite size is found to be 67.82 nm indicating that the particles observed in electron micrographs are constituted by smaller crystallites.

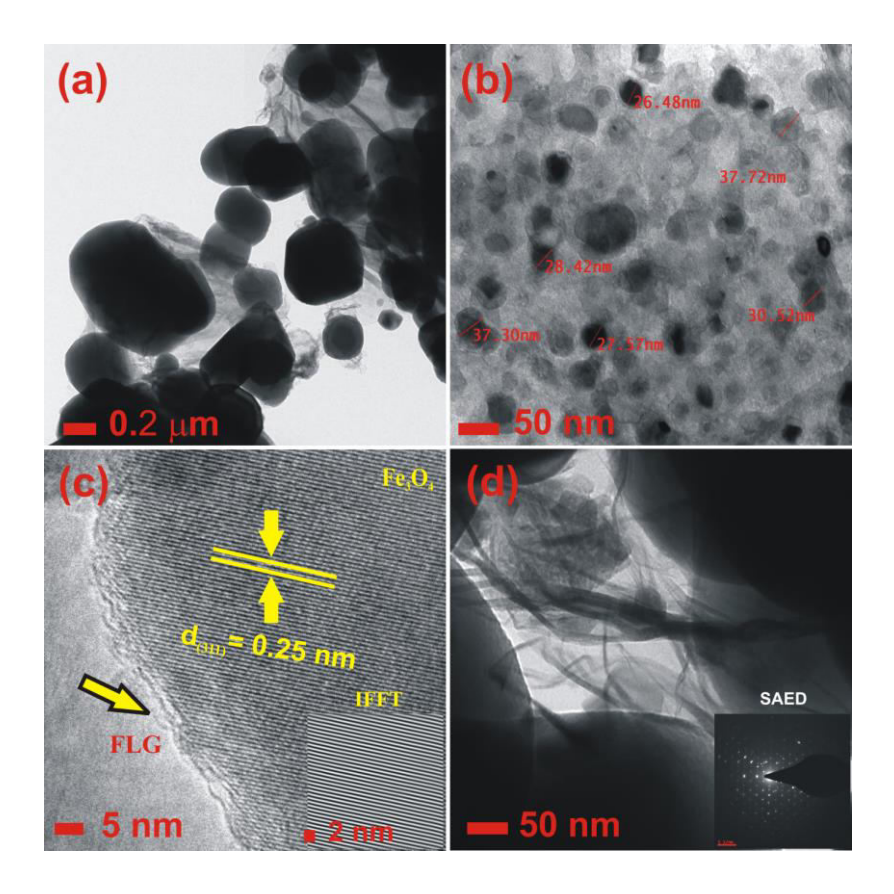


Fig. 4.30. Transmission electron microscope (TEM) micrographs of Fe₃O₄/FLG at different magnifications (a-b) individual Fe₃O₄ network of Micro and Nano (M-N) sized particles (c) HRTEM of the Fe₃O₄ lattice fringes (inset) IFFT pattern (d) FLG wrapped Fe₃O₄ and its selected area electron diffraction (SAED) inset pattern of Fe₃O₄/FLG composite.

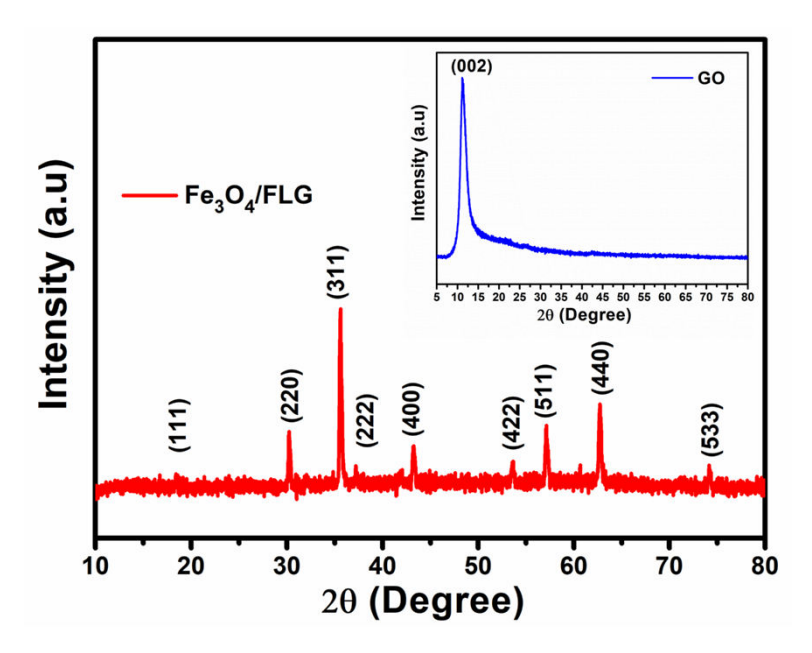


Fig. 4.31. X ray diffraction patterns of Fe₃O₄/FLG composite and GO (inset).

Elemental maps of Fe₃O₄/FLG powder sample are shown in Fig. 4.32. The maps depict that the as-synthesisized Fe₃O₄/FLG powder sample is constituted by iron (Fe), carbon (C), and oxygen (O). EDS analysis further showed there is a very slight presence of Sodium (Na) and Suphur (S) in the sample. The elemental mapping and EDS both were good aggreement with each other.

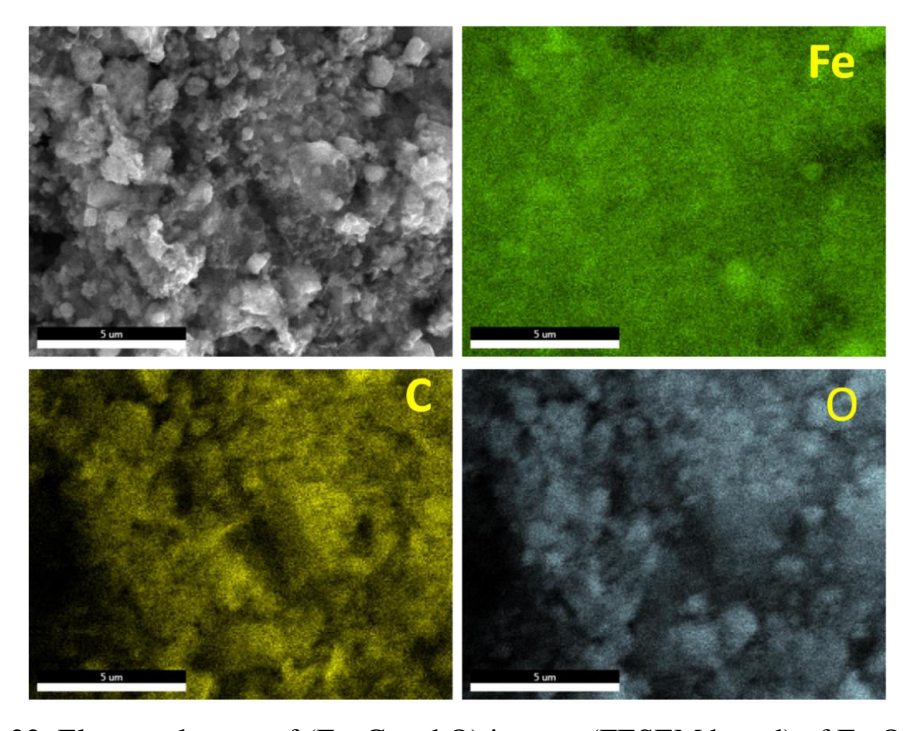


Fig. 4.32. Elemental maps of (Fe, C and O) images (FESEM based) of Fe₃O₄/FLG.

The Raman spectra (in the wavenumber range of 100 to 3500 cm⁻¹) of GO and Fe₃O₄/FLG composite are shown in Fig. 4.33. GO spectrum exhibits D-band (1345 cm⁻¹) and G-band (1598 cm⁻¹). The intensity ratio of D-band to G-band (I_D/I_G) calculated from the Raman spectrum is 0.92 which clearly indicates the graphite is converted into GO. This observation is consistent with XRD observations. Fe₃O₄/FLG spectrum exhibits D-band (1356.06 cm⁻¹) and G-band (1604.95 cm⁻¹). The I_D/I_G ratio in this case was slightly increased from 0.92 to 0.99 along with lower wave number shifting indicating that GO-Fe₂O₃ was reduced and lead to the formation of Fe₃O₄/FLG composite.

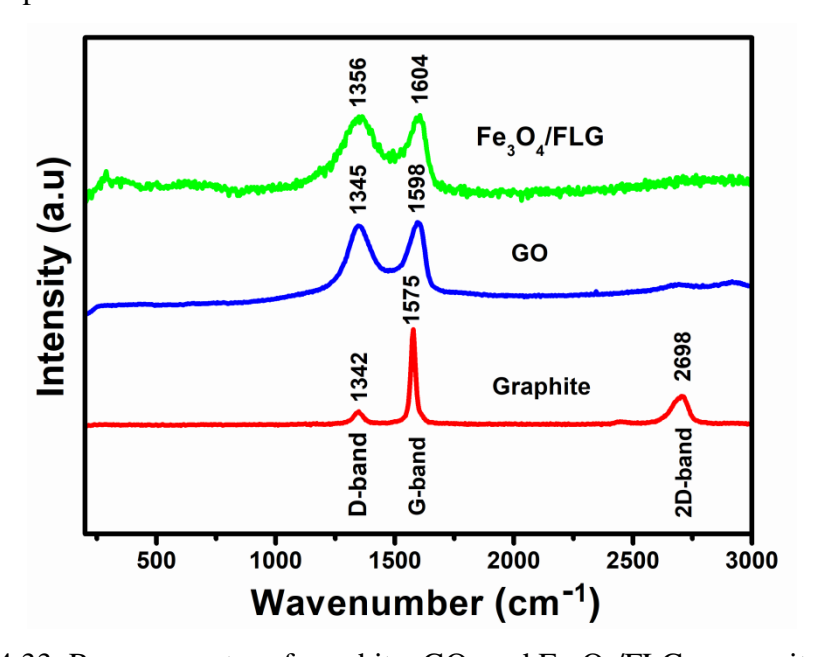


Fig. 4.33. Raman spectra of graphite, GO, and Fe₃O₄/FLG composite.

BET measurements of as obtained from Fe₃O₄/FLG powder sample was performed to find out specific surface area. Fig. 4.34 shows the nitrogen (N₂) adsorption/desorption isotherm information. The BET specific surface area was measured a 94.54 m²/g, which is quite low may be owing to the micron sized Fe₃O₄ particles and/or poor adsorption of N₂. As already discussed above Fe₃O₄/FLG with the high surface area helps to form active sites to detect the dopamine and other interference compounds such as AA and UA. The typical TGA analysis of Fe₃O₄/FLG to check individual weight percentage of composite. Fig. 4.35 shows gradual weight loss is due to the removal of the functional group present in the Fe₃O₄/FLG. The FLG weight percentage found that 22.58 wt % between 200 °C to 800 °C in the as-prepared Fe₃O₄/FLG composite.

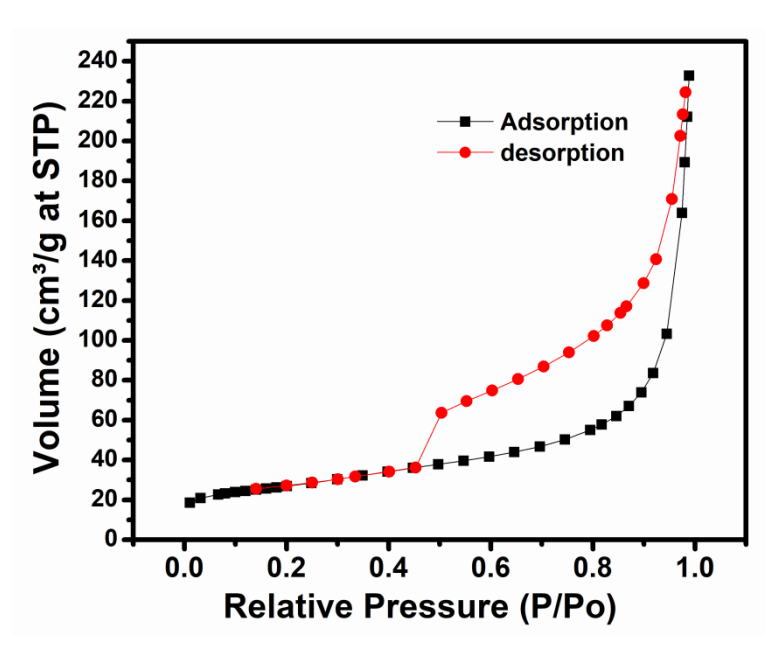


Fig. 4.34. (a) BET (Brunauer-Emmett- Teller) adsorption-desorption isotherm.

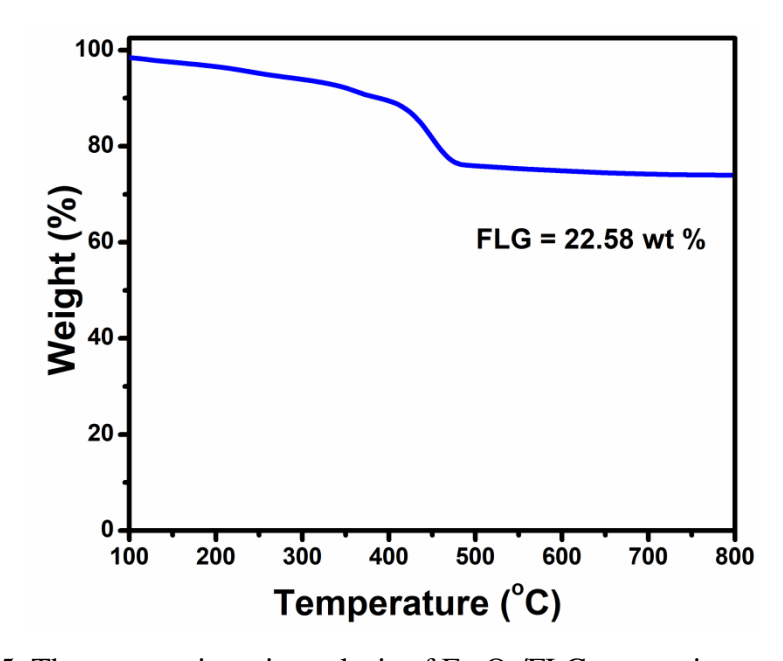


Fig. 4.35. Thermo gravimetric analysis of Fe₃O₄/FLG composite.

Cyclic voltammograms recorded for the considered electrodes are shown in Fig. 4.36. The system represents reduced redox peak current with high overpotential at the surface of bare GCE, and slight enhancement of redox peak current was observed for GO/GCE owing to the nature of GO. The surface of GO has many functional groups which make GO/GCE electrode electrically poor in conductivity. In other words, GO is electrically insulating material nature (due to the existence of disturbed SP^3 carbon atoms and delocalized SP^2 networks). On the other hand, after reduction Fe_3O_4/FLG is free from functional groups and the SP^2 networks is

partially restored. Fe₃O₄/FLG-GCE showed three folds enhancement in both current and anodic peak potential (E_{pa}), cathodic peak (E_{pc}) potentials noted as 244 mV and 132 mV, respectively in comparison to GCE and GO/GCE. This is expected owing to the superparamagnetic nature of Fe₃O₄ and electrical conductivity of exfoliated graphene sheets [42-45]. Furthermore, the reduction potential is owing to reduction of adsorbed DA layer on the Fe₃O₄/FLG-GCE shows the negative shift due to the strong interface between the adsorbed oxygen or hydroxyl groups and Fe₃O₄ surface as compared with bare GCE and GO/GCE. Additionally, modified Fe₃O₄/FLG-GCE performance as electrochemical sensor was showing superior electro catalytic activity for the detection of DA.

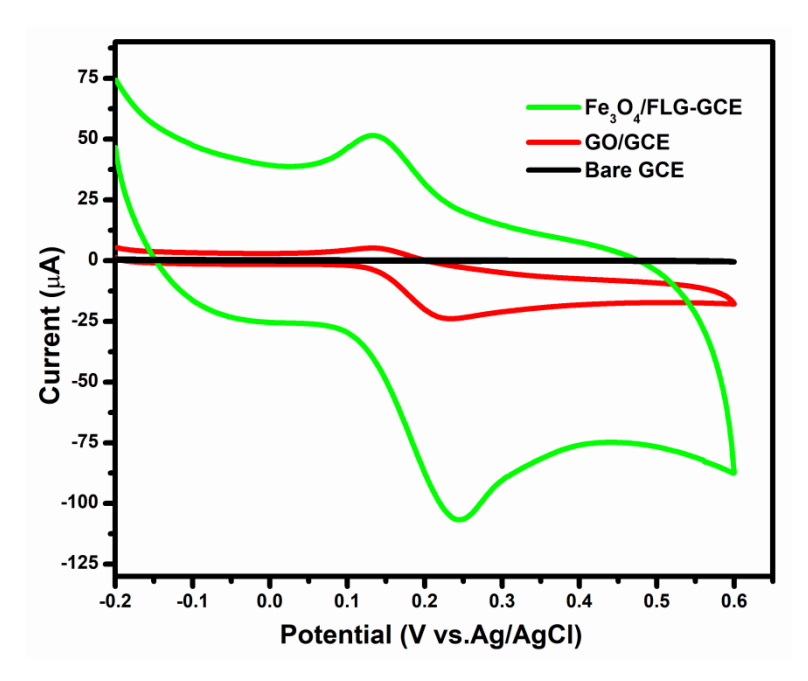


Fig. 4.36. Cyclic voltammogram (CV) of 0.1 mM DA concentration recorded for (a) bare GCE (b) GO/GCE (c) Fe₃O₄/FLG-GCE electrodes in the presence of 0.1 M PBS (pH 7.0) at a scan rate of 50 mVs⁻¹.

To inspect the reaction kinetics of DA, the potential sweep rate's influence on the peak currents and potential were also recorded. Fig. 4.37 shows CV of the modified FLG/Fe₃O₄/GCE electrochemical sensor at the various potential scanning ranges from 100 to 500 mVs⁻¹ of 0.1 mM DA concentration in presence of PBS solution at biological condition of pH 7.0. It is observed that the anodic current (I_{pa}) and cathodic current (I_{pc}) shifted to more positive and negative potentials, respectively, at elevated scan rates. Also, the peak current increased with increasing scan rates. The linear regression equations of I_{pa} and I_{pc} could be expressed as I_{pa} = 0.51486x + 76.95 (R^2 =0.9995) and I_{pc} = 0.451 x - 48.422 (R^2 = 0.9954). The results indicate

that the DA oxidation is an adsorption controlled process. It is observed that for higher scan rates the separation of redox peak positions increased as shown in Fig. 4.37(a). This indicates that charge transfer kinetics partially limit the occurrence of redox reactions leading to an increasing division of redox positions.

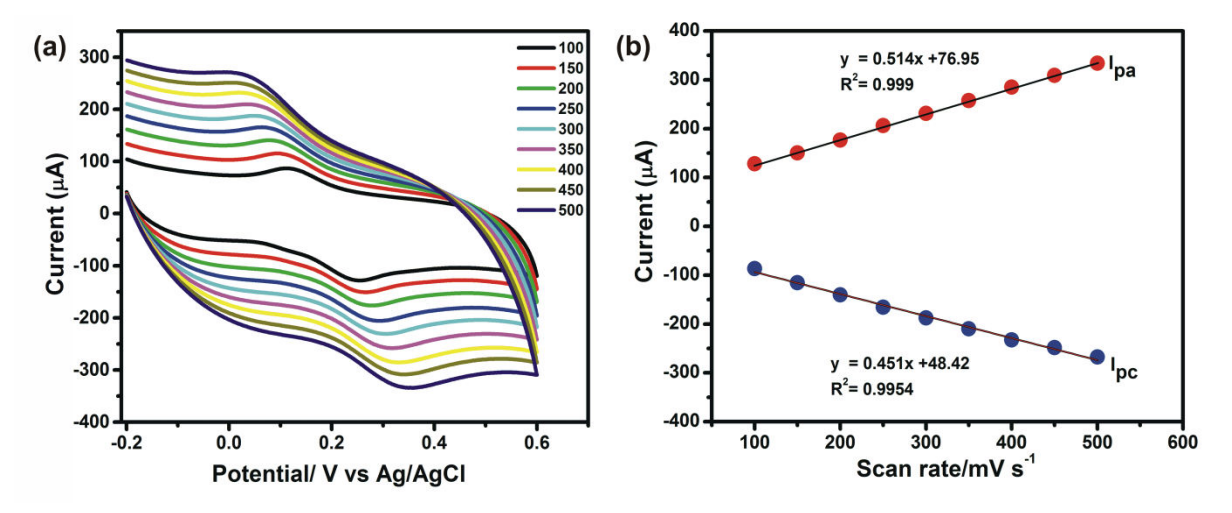


Fig. 4.37. (a) CV curves of modified Fe₃O₄/FLG-GCE electrode at the potential scanning range from 100 to 500 mV s⁻¹ in 0.1M PBS solution at pH 7.0 condition and (b) calibration plots for the redox peak current Vs. square root of scan rate.

To study the effect of pH on the electrochemical behavior of 0.1 mM DA modified $FLG/Fe_3O_4/GCE$ in 0.1 M PBS at different pH values starting from 5.0 to 8.0, DPV was performed and the results are shown in using as shown in Fig. 4.38(a). The potential shifted to the negative side, and it was also clear that the electrochemical behavior varies with pH of the electrolyte solution. Additionally, it is clearly observed that with increase in pH, there is a drop in peak current and simultaneous drop in peak potential. Besides this, the DA scale is downshifted to a negative potential by a slope of -57 mV represented by a linear regression with $R^2 = 0.991$ as shown in Fig. 4.38(b), which suggests that the total number of electrons and protons involved in charge transfer is the same. These observations are in good agreement with the available literature on the oxidation mechanism of DA.

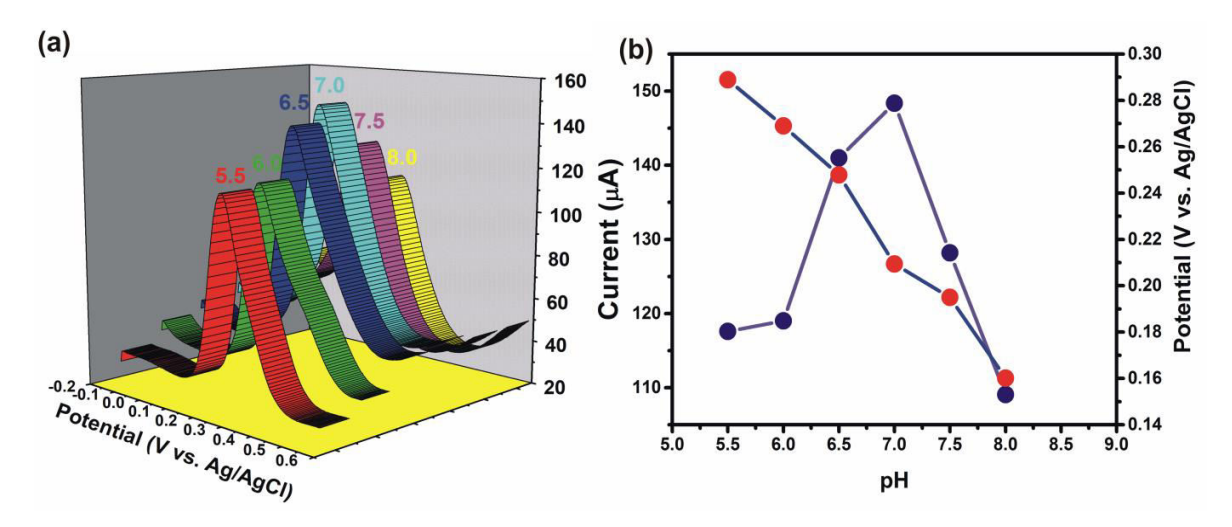


Fig. 4.38. (a) Three dimensional (3D) view of the DPV recorded for 0.1 mM of DA modified Fe₃O₄/FLG-GCE in 0.1 M PBS at various pH values starting from 5.5 to 8.0 and (b) the calibration plots of oxidation peaks of DA (left) current (μ A) (right) Vs. pH; here the scan rate is 50 mV s⁻¹.

To study the effect of DA concentration (26-60 nM) on the electrochemical behavior of DA modified Fe₃O₄/FLG-GCE in 0.1 M PBS at a pH value of 7.0, DPV was performed and the results are shown in using as shown in Fig. 4.39(a). It can be seen that the oxidation peak current has significantly improved with increasing concentration of DA. From Fig. 4.39(b) it can be clearly observed that the anodic peak current varied linearly with the concentration of DA represented by the linear regression relation I_{Pa} (μ A) = 621.93 [DA] + 6.808 (R² = 0.995, n=11). The Limit of detection (LOD) and the Limit of Quantification (LOQ) were calculated by using the formulae:

LOD=3S/M LOQ=10S/M

The calculated LOD and LOQ values are 3.4 nM and 11.43 nM, respectively for signal-to-noise ratio of three (S/N=3). The advantage of the modified Fe₃O₄/FLG-GCE electrode and the analytical performance of the electrochemical DA sensor (LOD and linear range) in this work when compared to the previous research reports summarized in Table 2.3 (Section 2.3 in Chapter 2) it can be inferred that the fabricated Fe₃O₄/FLG-GCE electrode is showing excellent analytical performance for the detection of DA.

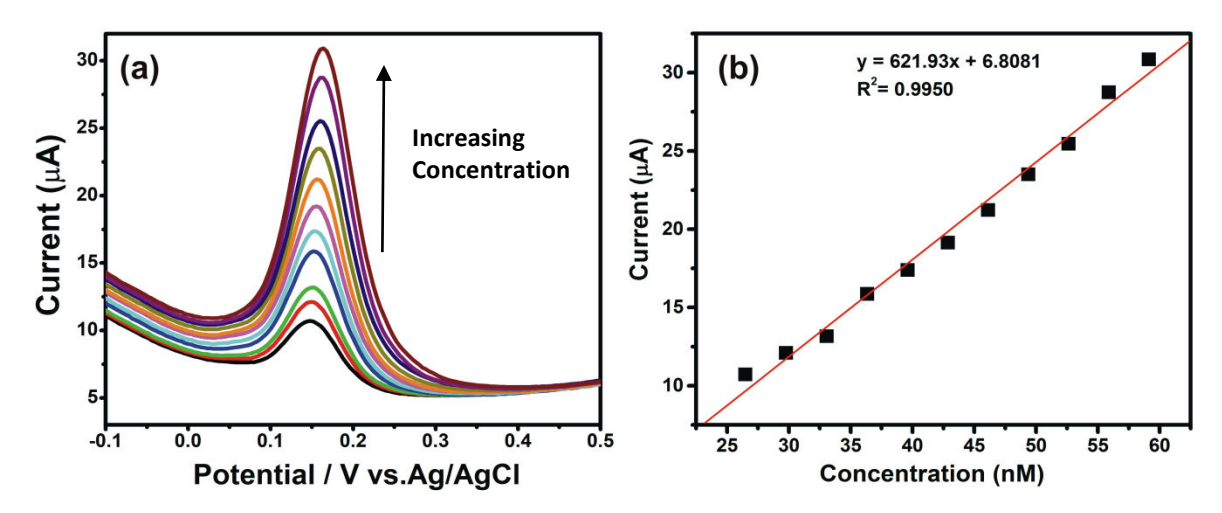


Fig. 4.39. Differential pulse voltammetry recorded for Fe₃O₄/FLG-GCE in 0.1 M PBS at a pH of 7.0 and with different DA concentrations and (b) the calibration plots of I_{pa} Vs. DA concentrations.

In order to check the ability of Fe₃O₄/FLG-GCE electrode in detecting DP in the presence of AA and UA, appropriate experiments (involving DPV) were conducted. DPV for ascorbic acid (AA) (different concentrations) in the presence of 1 µM UA and 0.1 µM DA. From Fig. 4.40(a), it can be observed that when AA is added, the oxidation potential of the biomolecules shifted to the right side. This is attributed to the alteration of the pH of the PBS solution due to the weak acidic nature of AA. The linear regression equation for the AA variation is Ipa = $0.391[AA] + 2.484 \,\mu A \,(R^2 = 0.9977)$ (Fig. 4.40(b)). The calculated LOD for AA is 72 μM with LDR of 15 to 40 µM. In another set of experiments (Fig. 4.40(c)), the concentration of DA was increased in the presence of 15 µM AA and 1 µM UA. In this case the linear regression equation is Ipa (μ A) = 9.496[DA] + 2.870 (R²=0.981) (Fig. 4.40(d)), LOD is 0.12 μ M and LDR is in the range 0.82-1.85 µM in the presence AA and UA. These results show the excellent selectivity of the electrode for DA in the presence of AA and UA. DPV related to the variation of uric acid (UA) concentration in the presence of 15 µM and 0.1µM DA is shown in Fig. 4.40(e). In this case, the linear regression equation is $I_{pa}=18.61 [UA]+2.604 \mu A (R^2=0.997) Fig. 4.40(f)$, LOD is 0.061 µM and LDR is in the range 103-205 µM in the presence of DA and AA. From the above observations it is clear that simultaneous determination of interfering species namely DA, AA and UA implies excellent performance of the Fe₃O₄/FLG-GCE electrode.

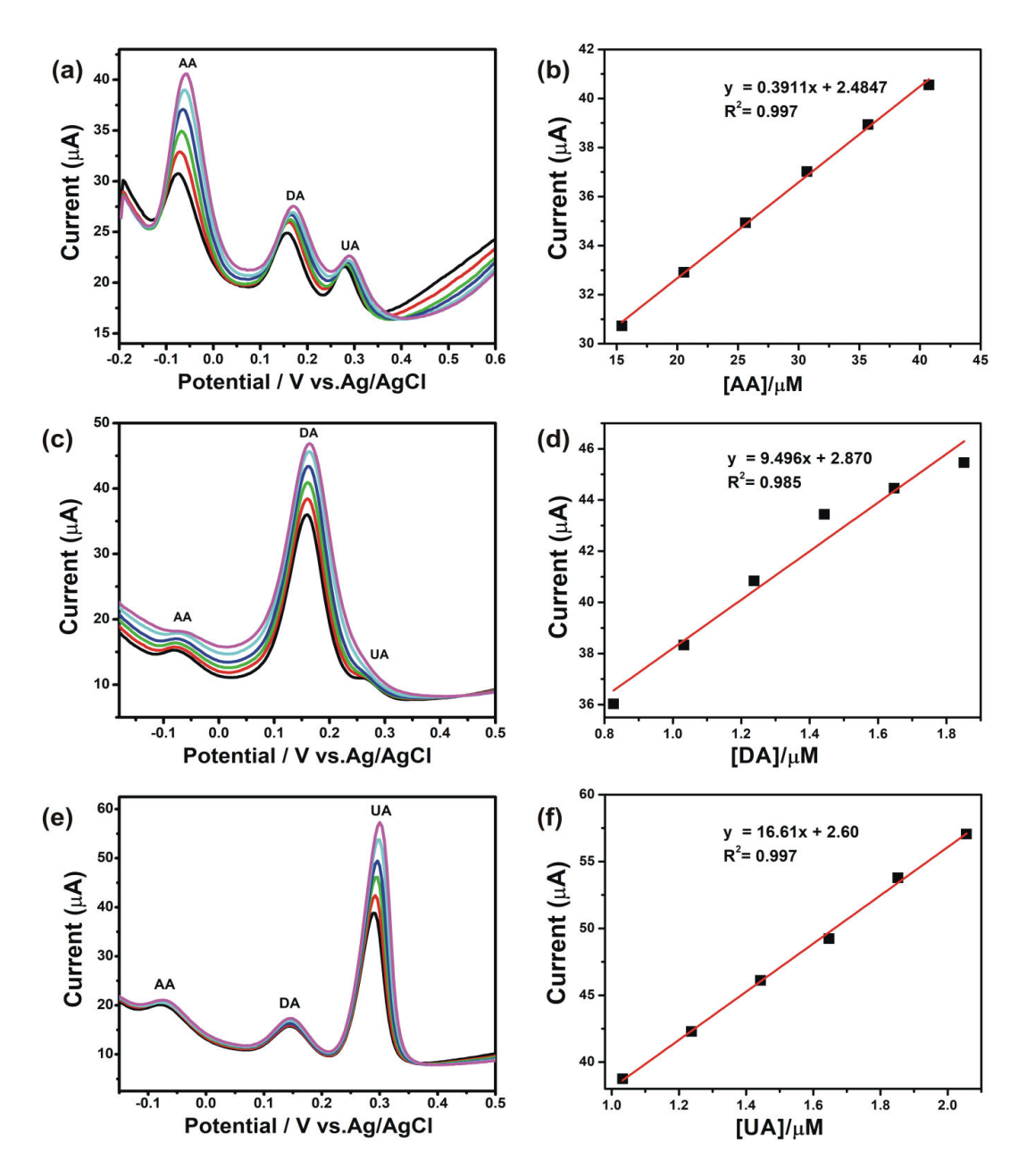


Fig. 4.40. DPV recorded at Fe₃O₄/FLG-GCE electrode in 0.1 M PBS (pH at 7.0) and at a scanning rate of 50 mV S⁻¹ in (a,b) 0.28 mM UA, 0.22 mM DA and different concentrations AA, (c,d) 0.5 mM AA, 0.28 mM UA and different concentrations of DA and (e,f) 5 mM AA , 0.2 mM of DA and different concentrations of UA.

References

- [1] Petnikota S, Rotte N, Srikanth VVSS, Kota BR, Reddy MV, Loh K, et al. Electrochemical studies of few-layered graphene as an anode material for Li ion batteries. J Solid State Electrochem. 2014;18:941-9.
- [2] Petnikota S, Maseed H, Srikanth VVSS, Reddy MV, Adams S, Srinivasan M, et al. Experimental elucidation of a graphenothermal reduction mechanism of Fe₂O₃: An enhanced

- anodic behavior of an exfoliated reduced graphene oxide/Fe₃O₄ composite in Li-ion batteries. The Journal of Physical Chemistry C. 2017;121:3778-89.
- [3] Petnikota S, Rotte NK, Reddy MV, Srikanth VVSS, Chowdari BVR. MgO-decorated few-layered graphene as an anode for Li-ion batteries. ACS Applied Materials & Interfaces. 2015;7:2301-9.
- [4] Levi MD, Levi EA, Aurbach D. The mechanism of lithium intercalation in graphite film electrodes in aprotic media. Part 2. Potentiostatic intermittent titration and in situ XRD studies of the solid-state ionic diffusion. Journal of Electroanalytical Chemistry. 1997;421:89-97.
- [5] Lin P-C, Wu J-Y, Liu W-R. Green and facile synthesis of few-layer graphene via liquid exfoliation process for Lithium-ion batteries. Sci Rep. 2018;8:9766.
- [6] Wang C, Gai G, Yang Y. shape modification and size classification of microcrystalline graphite powder as anode material for lithium-ion batteries. JOM. 2018;70:1392-7.
- [7] Chen K, Yang H, Liang F, Xue D. Microwave-irradiation-assisted combustion toward modified graphite as lithium ion battery anode. ACS Appl Mater Interfaces. 2018;10:909-14.
- [8] Cui X, Tang F, Li C, Zhang Y, Wang P, Li S, et al. Pretreatment of graphite anodes with lithium sulfate to improve the cycle performance of lithium-ion batteries. Energy Technology. 2017;5:549-56.
- [9] Zhang T, de Meatza I, Qi X, Paillard E. Enabling steady graphite anode cycling with high voltage, additive-free, sulfolane-based electrolyte: Role of the binder. J Power Sources. 2017;356:97-102.
- [10] Wu Y, Li Y-F, Wang L-Y, Bai Y-J, Zhao Z-Y, Yin L-W, et al. Enhancing the Li-ion storage performance of graphite anode material modified by LiAlO₂. Electrochim Acta. 2017;235:463-70.
- [11] Wu Y, Wang L-Y, Li Y-F, Zhao Z-Y, Yin L-W, Li H, et al. KCl-modified graphite as high performance anode material for lithium-ion batteries with excellent rate performance. J Phys Chem C. 2017;121:13052-8.
- [12] Kim DS, Chung DJ, Bae J, Jeong G, Kim H. Surface engineering of graphite anode material with black TiO₂-x for fast chargeable lithium ion battery. Electrochim Acta. 2017;258:336-42.
- [13] Ding F, Xu W, Choi D, Wang W, Li X, Engelhard MH, et al. Enhanced performance of graphite anode materials by AlF₃ coating for lithium-ion batteries. Journal of Materials Chemistry. 2012;22:12745-51.

- [14] Jung YS, Cavanagh AS, Riley LA, Kang S-H, Dillon AC, Groner MD, et al. Ultrathin direct atomic layer deposition on composite electrodes for highly durable and safe Li-ion batteries. Advanced Materials. 2010;22:2172-6.
- [15] Lee S-E, Kim E, Cho J. Improvement of electrochemical properties of natural graphite anode materials with an ovoid morphology by AlPO₄ coating. Electrochemical and Solid-State Letters. 2007;10:A1-A4.
- [16] Hameed AS, Reddy MV, Chowdari BVR, Vittal JJ. Preparation of rGO-wrapped magnetite nanocomposites and their energy storage properties. RSC Advances. 2014;4:64142-50.
- [17] Petnikota S, Marka SK, Banerjee A, Reddy MV, Srikanth VVSS, Chowdari BVR. Graphenothermal reduction synthesis of 'exfoliated graphene oxide/iron (II) oxide' composite for anode application in lithium ion batteries. Journal of Power Sources. 2015;293:253-63.
- [18] Zhao B, Zheng Y, Ye F, Deng X, Xu X, Liu M, et al. Multifunctional Iron Oxide Nanoflake/Graphene Composites Derived from Mechanochemical Synthesis for Enhanced Lithium Storage and Electrocatalysis. ACS Applied Materials & Interfaces. 2015;7:14446-55.
- [19] Petnikota S, Rotte NK, Reddy MV, Srikanth VVSS, Chowdari BVR. MgO-decorated few-layered graphene as an anode for li-ion batteries. ACS Applied Materials & Interfaces. 2015;7:2301-9.
- [20] Zhong-Shuai Wu GZ, Li-ChangYin, Wencai Ren, FengLi H-M. Graphene/metaloxidecompositeelectrodematerials for energystorage. Nano Energy. 2012; 1:107–31.
- [21] Chen D, Ji G, Ma Y, Lee JY, Lu J. Graphene-encapsulated hollow Fe₃O₄ Nanoparticle Aggregates As a High-Performance Anode Material for Lithium Ion Batteries. ACS Applied Materials & Interfaces. 2011;3:3078-83.
- [22] Zhao J, Yang B, Zheng Z, Yang J, Yang Z, Zhang P, et al. Facile preparation of one-dimensional wrapping structure: graphene nanoscroll-wrapped of Fe₃O₄ nanoparticles and its application for lithium-ion battery. ACS Applied Materials & Interfaces. 2014;6:9890-6.
- [23] Yang Y, Li J, Chen D, Zhao J. A facile electrophoretic deposition route to the Fe₃O₄/CNTs/rGO composite electrode as a binder-free anode for lithium ion battery. ACS Applied Materials & Interfaces. 2016;8:26730-9.
- [24] Qi L, Xin Y, Zuo Z, Yang C, Wu K, Wu B, et al. Grape-like Fe₃O₄ agglomerates grown on graphene nanosheets for ultrafast and stable lithium storage. ACS Applied Materials & Interfaces. 2016;8:17245-52.

- [25] Zhao L, Gao M, Yue W, Jiang Y, Wang Y, Ren Y, et al. Sandwich-structured graphene-Fe₃O₄@carbon nanocomposites for high-performance lithium-ion batteries. ACS Applied Materials & Interfaces. 2015;7:9709-15.
- [26] Hu X, Ma M, Zeng M, Sun Y, Chen L, Xue Y, et al. Supercritical carbon dioxide anchored Fe₃O₄ nanoparticles on graphene foam and lithium battery performance. ACS Applied Materials & Interfaces. 2014;6:22527-33.
- [27] Petnikota S, Marka SK, Srikanth VVSS, Reddy MV, Chowdari BVR. Elucidation of few layered graphene-complex metal oxide ($A_2Mo_3O_8$, A = Co, Mn and Zn) composites as robust anode materials in Li ion batteries. Electrochimica Acta. 2015;178:699-708.
- [28] Marka SK, Petnikota S, Srikanth VVSS, Reddy MV, Adams S, Chowdari BVR. Co₂Mo₃O₈/reduced graphene oxide composite: synthesis, characterization, and its role as a prospective anode material in lithium ion batteries. RSC Advances. 2016;6:55167-75.
- [29] Koyama K, Harada T. Phase Diagram of Fe-Mo-O System at 1173-1473 K. Journal of the Japan Institute of Metals. 1994;58:1401-7.
- [30] Sun Y, Hu X, Luo W, Huang Y. Hierarchical Self-assembly of Mn2Mo3O8-graphene Nanostructures and their Enhanced Lithium-storage Properties. Journal of Materials Chemistry. 2011;21:17229-35.
- [31] Petnikota S, Srikanth VVSS, Nithyadharseni P, Reddy MV, Adams S, Chowdari BVR. Sustainable Graphenothermal Reduction Chemistry to Obtain MnO Nanonetwork Supported Exfoliated Graphene Oxide Composite and its Electrochemical Characteristics. ACS Sustainable Chemistry & Engineering. 2015;3:3205-13.
- [32] Petnikota S, Teo KW, Chen L, Sim A, Marka SK, Reddy MV, et al. Exfoliated Graphene Oxide/MoO2 Composites as Anode Materials in Lithium-Ion Batteries: An Insight into Intercalation of Li and Conversion Mechanism of MoO₂. ACS Applied Materials & Interfaces. 2016;8:10884-96.
- [33] Petnikota S, Rotte NK, Srikanth VVSS, Kota BSR, Reddy MV, Loh KP, et al. Electrochemical studies of few-layered graphene as an anode material for Li ion batteries. Journal of Solid State Electrochemistry. 2014;18:941-9.
- [34] Sun Y, Hu X, Luo W, Shu J, Huang Y. Self-assembly of Hybrid Fe₂Mo₃O₈-reduced graphene oxide nanosheets with enhanced lithium storage properties. Journal of Materials Chemistry A. 2013;1:4468-74.
- [35] Dong X, Wang K, Zhao C, Qian X, Chen S, Li Z, et al. Direct synthesis of RGO/Cu₂O composite films on Cu foil for supercapacitors. Journal of Alloys and Compounds. 2014;586:745-53.

- [36] Ma Z, Cao H, Zhou X, Deng W, Liu Z. Hierarchical porous MnO/graphene composite aerogel as high-performance anode material for lithium ion batteries. RSC Advances. 2017;7:15857-63.
- [37] Xiao Y, Wang X, Wang W, Zhao D, Cao M. Engineering Hybrid between MnO and N-Doped Carbon to Achieve Exceptionally High Capacity for Lithium-Ion Battery Anode. ACS Applied Materials & Interfaces. 2014;6:2051-8.
- [38] Luo W, Hu X, Sun Y, Huang Y. Controlled Synthesis of Mesoporous MnO/C Networks by Microwave Irradiation and Their Enhanced Lithium-Storage Properties. ACS Applied Materials & Interfaces. 2013;5:1997-2003.
- [39] Zheng JP, Jow TR. A New Charge Storage Mechanism for Electrochemical Capacitors. Journal of The Electrochemical Society. 1995;142:L6-L8.
- [40] De Silva KSB, Gambhir S, Wang XL, Xu X, Li WX, Officer DL, et al. The effect of reduced graphene oxide addition on the superconductivity of MgB2. Journal of Materials Chemistry. 2012;22:13941-6.
- [41] Xing L, Qu M, Huai Y, Zuolong Y. Preparation and electrochemical performance of Li 4Ti 5O 12/carbon/carbon nano-tubes for lithium ion battery2010.
- [42] Yu L, Wu H, Wu B, Wang Z, Cao H, Fu C, et al. Magnetic Fe₃O₄-Reduced Graphene Oxide Nanocomposites-Based Electrochemical Biosensing. Nano-Micro Letters. 2014;6:258-67.
- [43] He H, Gao C. Supraparamagnetic, Conductive, and Processable Multifunctional Graphene Nanosheets Coated with High-Density Fe₃O₄ Nanoparticles. ACS Applied Materials & Interfaces. 2010;2:3201-10.
- [44] Majumder S, Sardar M, Satpati B, Kumar S, Banerjee S. Magnetization Enhancement of Fe3O4 by Attaching onto Graphene Oxide: An Interfacial Effect. The Journal of Physical Chemistry C. 2018;122:21356-65.
- [45] Su J, Cao M, Ren L, Hu C. Fe₃O₄—Graphene Nanocomposites with Improved Lithium Storage and Magnetism Properties. The Journal of Physical Chemistry C. 2011;115:14469-77. [46] Maseed H, Petnikota S, Vadali SVSS, Srinivasan M, B.V.R C, Reddy MVV, et al. Fe₂Mo₃O₈/exfoliated graphene oxide: solid-state synthesis, characterization and anodic application in Li-ion batteries. New Journal of Chemistry. 2018.

Chapter 5 Conclusions and Future Scope

5.1 Conclusions

The novel solid state reduction synthesis technique was employed to prepare Metal oxide - few layer graphene (FLG) nanocomposites of Fe₂Mo₃O₈/FLG, Fe₃O₄/FLG and MnO/FLG in mass quantity. To prepare FLG, microwave reduction method was also used. The as obtained above metal oxide (MO)-FLG composite structural, morphological, chemical, BET surface area measurements were carried out by using different characterization techniques such as FESEM, HRTEM, Raman, XRD, XPS, TGA, BET. In that MW-RGO, Fe₃O₄/ FLG Fe₂Mo₃O₈/FLG, was tested for anode materials in Li-ion battery applications by fabricating coin cell. To study electrochemical performance, it was characterized by cyclic voltammetry, galvanostatic charge-discharge, and electrochemical impedance spectroscopy measurements was performed. Highly crystalline FLG is synthesized from MWI hcFLG as an anode of coin cell Li-ion battery delivered reversible capacities as high as 400 and 330 mAh g⁻¹ at 0.1 C and 1.0 C current rates, respectively. It exhibited excellent rate capability by showing reversible capacity of 215 mAh g⁻¹ even at a very high current rate of 10.0 C. Long-term cycling of hcFLG showed a great increase in reversibly capacity from 330 to 555 mAh g⁻¹ at 1175th cycle of 1.0 C rate and from 200 to 365 mAh g⁻¹ at 1160th cycle of 2.0 C rate. Enhanced surface lithiation above 0.3 V is found responsible for the increased capacity as confirmed from post-cycling CV, structural and EIS analyses. CV features before and after long-term cycling showed clear Li-staging phenomenon below 0.3 V that confirm stable capacity contribution from diffusion controlled lithiation. Overall hcFLG exhibited excellent lithiation electrochemistry and performed far superior to commercial graphite as well as other reported similar materials. The reducing ability of GO w.r.t to Fe₂O₃ can be tailored with its DO. GO with low DO anneals slowly and simultaneously reduces Fe₂O₃ to Fe₃O₄, FeO and Fe depending on heating time and temperature. Thus it leads to a three stage reduction represented by ${}^{1}2G01 + Fe_{2}O_{3} \rightarrow$ FLG/Fe_3O_4 (Stage I) \rightarrow FLG/FeO(Stage II) \rightarrow FLG/Fe(Stage III). In contrast, GO with high DO anneals rapidly and restricts to only first stage reduction $2GO2 + Fe_2O_3 \rightarrow$ FLG/Fe₃O₄ (Stage I)' i.e., it forms only Fe₃O₄ for all times of heating. Even doubling the amount of GO2 was found to be ineffective on the reduction process. Thus it is possible to control the reduction of Fe₂O₃ with GO by varying GO's DO and heat treatment time and temperature. DO of GO is a key factor to decide the nature of FLG-reduced iron oxide composites and their electrochemistry. Fe₃O₄/FLG composite prepared by using GO1 exhibited better cycling performance with reversible capacity as high as 860 mAh/g owing to good contacts between FLG and Fe₃O₄ phases. Fe₃O₄/FLG composite prepared in this work can perform even better if uniform distribution of Fe₃O₄ nanoparticles on FLG surfaces is achieved. A systematic study encompassing GTR synthesis, characterization and anodic application in LIBs of Fe₂Mo₃O₈/FLG composite is reported. Electron microscopy (both SEM and TEM) of the as-prepared composite showed that Fe₂Mo₃O₈ was in the form of hexagonal platelets while EG possessed sheet-like morphology. Diffraction analysis showed that Fe₂Mo₃O₈ phase is well crystallized into the hcp system. The compositional analysis confirmed the presence of highquality Fe₂Mo₃O₈ and FLG phases in the composite. BET surface area measurements suggested that the composite possessed a low specific surface area of 2.8 m² g⁻¹ and low porosity owing to the presence of low amount of FLG and high crystalline quality of Fe₂Mo₃O₈. Assynthesized Fe₂Mo₃O₈/FLG was found to be suitable for anodic application in LIBs with a reversible capacity as high as 945 mAh g⁻¹ at 50 mA g⁻¹ current rate. The as-synthesized MnO-FLG composite with Micro-Nano sized particles; networks are uniformly anchored on few layered Graphene (FLG) sheets which facilitate easy and efficient transfer of electrons and ions in the fabricated electrode in the presence of 1M LiSO₄. The synergic effect between the FLG sheets and MnO composite electrode exhibited high specific capacitance with 778.5 F g⁻¹ at a current density of 0.5 m A g⁻¹ and showing good long term cycling stability. These exhibited resulted works clearly demonstrate that well designed eco-friendly route to prepare novel FLG based metal oxide electrode materials with enhanced electrochemical performance for the application of large scale electrochemical energy storage applications. The Fe₃O₄/FLG composite prepared at 650 °C for 5 h investigated for electrochemical detection of dopamine (DA) sensors in the presence of uric acid (UA) and ascorbic acid (AA) in 1 M phosphate buffer solution (PBS). The modified Fe₃O₄/FLG-GCE has shown extraordinarily high redox peak currents and the results presented herein have oxygen-containing functional groups facilitating AA, DA, and UA adsorption electro-oxidation. The modified Fe₃O₄/FLG-GCE showed a high kinetic sensitivity of electron transfer with selectivity for DA in the presence of AA, and UA. The modified Fe₃O₄/FLG-GCE shows excellent electrocatalytic action and excellent selectivity towards DA detection in the presence of AA, and UA. Therefore, these results were proposed for the advance electrode of binder free modified Fe₃O₄/FLG-GCE for DA detection gave outstanding results with the low Limit of detection (LOD) as 3.429 nM, and the limit of quantification (LOQ) calculated as 11.43 nM. These results from the Fe₃O₄/FLG-GCE composite will get attention for the applicability of electrochemical DA detection in the analysis of real samples with high selectivity for real-time application. Finally, in this work

even it has lower surface area of Fe₃O₄/FLG composite due to its combined M-N sized particles of Fe₃O₄ feature and this work unlock to develop novel modified electrode materials like Fe₃O₄/FLG-GCE for electrochemical sensing of DA application.

5.2 Future Scope

Firstly, the Solid state reduction technique is highly controlling synthesis method to prepare novel Metal oxide-FLG in bulk scale quantity. This method is modification previously reported carbothermal reduction method where instead of carbon GO was employed and its advantages has been explored briefly. Coming to that mechanism it is to be further needs some more investigation what parameters helping or hindering its application. The advantage of GO as reducing agent its very cheap can be made at laboratory due to the morphology of metal oxide nanoparticle change in shape or size may be varied. In this present thesis work, the combination micron – nano metered (M-N) size particle with different morphology was highlighted for Liion battery, super capacitors and electrochemical dopamine (DA) sensor applications. As previously discussed in the thesis, the Fe₃O₄/FLG synthesized from GTR technique like MnO/FLG can be useful super capacitor application with small modification according to previous reports to improve the performance of specific capacitance. Also, Fe₃O₄/FLG can be used for EMI shielding and to remove heavy metals and toxic elements from the polluted water. The above bring up scope is for the urgent prospect study.

Development of Novel Metal Oxide/Graphene Nanocomposites for Electrochemical- Energy Storage and Sensing Applications

by Hussen Maseed

Submission date: 28-Oct-2019 05:06PM (UTC+0530)

Submission ID: 1201924658

File name: Hussen PhD Thesis Plag.pdf (2.29M)

Word count: 19377 Character count: 97305

Development of Novel Metal Oxide/Graphene Nanocomposites for Electrochemical- Energy Storage and Sensing Applications

ORIGINALITY REPORT

25%

7%

22%

11%

SIMILARITY INDEX

INTERNET SOURCES

PUBLICATIONS

STUDENT PAPERS

PRIMARY SOURCES

Hussen Maseed, Shaikshavali Petnikota, Vadali V. S. S. Srikanth, Madhavi Srinivasan et al. "Fe Mo O /exfoliated graphene oxide: solid-state synthesis, characterization and anodic application in Li-ion batteries ", New Journal of Chemistry, 2018

10%

Publication

Publication

Shaikshavali Petnikota, Hussen Maseed, V. V. S. S. Srikanth, M. V. Reddy, S. Adams, Madhavi Srinivasan, B. V. R. Chowdari. "Experimental Elucidation of a Graphenothermal Reduction Mechanism of Fe O: An Enhanced Anodic Behavior of an Exfoliated Reduced Graphene Oxide/Fe O Composite in Li-Ion Batteries ", The Journal of Physical Chemistry C, 2017

5%

Submitted to Yeungnam University
Student Paper

1%

4

Submitted to Heriot-Watt University
Student Paper

1%